Mid-spatial Frequency Control for Automated Functional Surface Processing

XIAO ZHENG

A thesis submitted to the University of Huddersfield

in partial fulfilment of the requirements for

the degree of Doctor of Philosophy

School of Computing and Engineering

The University of Huddersfield

September 2017

This thesis is for my wife and parents.

Copyright Statement

XIAO ZHENG

JULY 2018

Acknowledgements

Firstly, I would like to express my gratitude to my primary supervisor, Professor David Walker, who provided me with the opportunity of this PhD course and continuously supported me in many aspects during these four years. I can still remember the card he sent me in the first Chinese New Year written in strange Mandarin, which cured my homesick. This thesis would not be completed without your help and Many Thanks!

Special thanks to Dr Guoyu Yu, who has provided me with a lot of helpful advice, not limited to scientific issues, but also for my daily life. Thanks to Dr Hongyu Li for his precious advice about the structure of this thesis.

Special thanks go to a friendly group at OpTIC centre for a lot of help I received from them. Specially thanks to Professor Paul Reeds and Garry Davies for their guidance to use a 4D interferometer. Rob Evans for his assistance of operating ADE white light interferometer.

I would also like to acknowledge the financial support from the University of Huddersfield, which enables me to undertake this study.

Finally, but by no means least, thanks go to my parents and my wife for almost unbelievable support. They are the most important people in my world, and I dedicate this thesis to them.

Abstract

Functional surfaces interact with surrounding substances, such as another solid, a liquid, gas, acoustic or electromagnetic waves etc., in order to achieve a required effect. Surfaces are increasingly required with complex forms and ever-increasing precision, can be very challenging to make. In particular, mid-spatial frequency (MSF) ripples are difficult to avoid for various reasons, but especially the changing misfit between a polishing tool as it moves across a complex workpiece surface.

Current surface processing techniques are limited in their ability effectively to control or remove MSF errors for the reasons: i) lack of the ability to conform to the complex working surfaces, including grinding and lapping; ii) low material removal rate, such as Magneto-rheological finishing and fluid jet polishing; iii) high cost (typically for ion beam figuring); iv) constrains for the size of the workpiece, such as stressed lap polishing and stressed mirror polishing.

This thesis reports on the development of enhanced techniques, both to understand the formation of MSF errors on aspherical surfaces, and to mitigate them, increasing overall production efficiency. This has been achieved by:

1) Development of a novel stressed mirror technique providing a universal platform for aspheric experiments.
2) Results and analysis of kinetic simulations to understand the working mechanism of the non-Newtonian material under different stress conditions.
3) Developing a non-Newtonian tool, used in a novel way, to manage misfit between an aspherical workpiece and the tool surface. Peak-to-valley MSF error on an off-axis aspheric part better than 10 nm has been achieved.
4) Using bonded diamond pads, with various diamond sizes in a ‘grolishing’ (hybrid between grinding and polishing) procedure to achieve extremely high material removal rates (up to 267 mm^3/min), and control MSF errors 10 nm peak-to-valley, on flat and spherical surfaces.

5) Providing an aspherical surface after grolishing by a 3-microns diamond pad, with texture of sufficiently quality to be measured *directly* by an interferometer, which usually be achieved only after polishing.

Contents

List of Figures

List of Tables

List of Abbreviations

CNC	Computer Numerical Control
E-ELT	European Extremely Large Telescope
FEA	Finite Element Analysis
FJP	Fluid Jet Polishing
IBF	Ion Beam Figuring
MRF	Magneto-Rheological Finishing
MSF	Mid-Spatial Frequency
PSF	Point Spread Function
PV	Peak to Valley
RAPT	Reactive Atomic Plasma Technology
RMS	Root Mean Square
SA	Surface Average

SLP	Stressed Lap Polishing
SMP	Stressed Mirror Polishing
SNR	Signal to Noise Ratio
SSD	Sub Surface Damage
STP	Shear Thickening Polishing
TIF	Tool Influence Function

This page is left blank intentionally

Chapter 1. Introduction

‘冯翼惟象，何以识之’

‘How could we observe the vast universe?’

--《天问》 屈原

--Poem from antiquity “Heavenly Questions”

By Qu Yuan

1.1 Functional Surfaces

More than 150 questions about the universe were raised in this poetry attributed to Qu Yuan (c. 340–278 BC)[1], a Chinese poet who lived during the Warring States period and remembered as the origin of Dragon Boat Festival. This question was raised followed by ‘*How could the universe be created from nothing*’ and ‘*How could we understand the natural law of the universe*’. In order to give answers to these basic philosophy questions, the first telescope was invented by Galileo in 1609[2, 3] to observe the outer space. Since then, more telescopes with larger aperture were fabricated to observe this vast universe trying to answer these ultimate questions.[4, 5] Microscopy was also invented trying to explore the mysteries of nature from the macro level to the

quantum level. In these observations, precision optics play an important role to enable us to achieve clear images with good contrast and resolution.

When a surface can interact with the surrounding substances, such as fluid, gas, electromagnetic waves etc., and achieve a certain effect, this surface is defined as a functional surface. Reflection or transmission of the visible light is one of the important functions that discussed in this thesis. Apart from it, the surface of a turbine, which reacts with liquids or air providing driving force, or a solar cell surface, which transfers energy form from electromagnetic waves to electricity, can also be classified as functional surfaces.

Functional surfaces are used widely, and they have impact on our lives in many aspects, including manufacturing, medical, transportation, national defence, etc. Some examples are listed in **Table 1.1**. Functional surfaces include, but are not limited to these examples.

Table 1.1: List of examples for functional surfaces.

Surfaces	Functions
Optical surface	Reflecting or transmitting light
Surface of turbine	React with air or water to provide a driving force
Surface of solar cell	Photoelectric conversion
Artificial joint surface	Reduce friction during the limb movement
Mould surface	Limit the shape of the filler

1.2 Mid-Spatial Frequency (MSF)

1.2.1 Introduction of MSF

Surface errors can be introduced by many manufacturing processes during the fabrication of functional surfaces.[6] They are divided into low, middle and high spatial frequencies. Low-spatial frequency errors refer to the surface form errors, and high-spatial frequency errors point to the surface texture.

However, the definition of Mid-spatial frequency (MSF) errors is ambiguous in the literature. Their range varies with the size of part and tool used in the practical production. Generally, it is agreed that MSF errors are higher in frequency than Zernike polynomial specs and lower than surface roughness, which bridges the gap between traditional form errors and final surface finishing.[7] For the most of surface processing technologies, the mid-spatial frequency ranges from 0.02/mm to 1/mm.[8, 9] Spatial frequency below 0.02/mm refers to the low-spatial frequency, which is also known as surface form. Spatial frequency above 1/mm refers to the high-spatial frequency, which represents the roughness and surface texture.

1.2.2 Initiation of MSF

1.2.2.1 Overlap of tool influence functions

MSF errors usually appear to be periodic straight or circular ripples on surfaces due to the discontinuous overlap of the tool influence function in the direction perpendicular to the movement of the tool.

Tool influence function (TIF) usually comes about when putting a working tool on a fixed position of the workpiece surface. It represents the material removal by a

polishing tool in a unit time. The overall material removal during the process can be regarded as the integration of tool influence functions.

Take an example of a process using a raster tool path, which is shown in **Figure 1.1**. The material removal along the X direction is continuous in one track apart from the edge zone, but that in the Y direction depends on the overlap of the tracks. The material removal along the Y axis is more even if the track spacing is decreased, but in practice, it can never be uniform, as shown in **Figure 1.2**.

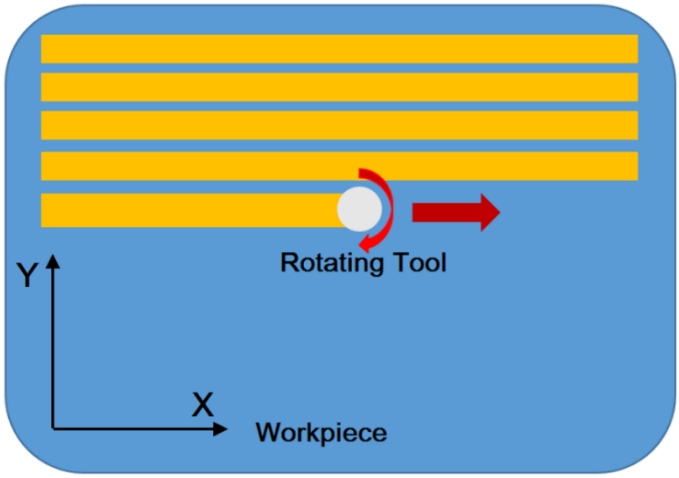

Figure 1.1: A rotating tool that working on a surface with raster tool path.

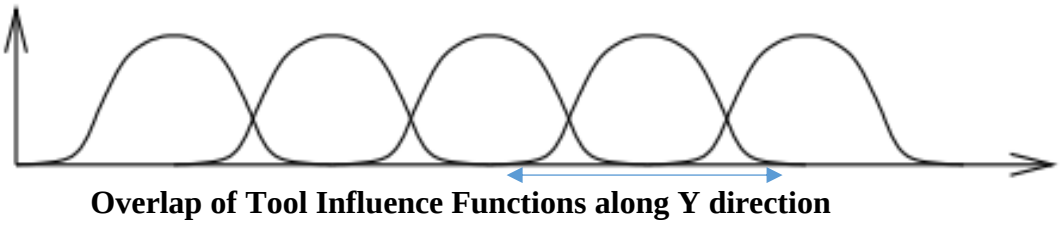

Figure 1.2: The overall material removal can be regarded as the integration of tool influence functions and it can never be uniform no matter how close they overlap with each other.

It also means that MSF error cannot be avoided using a regular tool path in surface processing based on the relative movement between the workpiece surfaces and tools to remove material. Dunn and Walker have presented a random tool path for subaperture polishing and compare polishing with the random and raster tool paths. The results shows that the random tool path could not only removing the MSF errors but also be helpful to avoid MSF in surface processing. However, the material removal is not uniform in practical experiments, which limits its application for form correction.[10]

1.2.2.2 Aspherical misfit

The asphere is a more complex surface profile, which can reduce or eliminate the spherical aberration and also reduce some optical aberrations (astigmatism for example). The utility of an aspherical part has obvious advantages since a single aspheric surface can often replace a number of spherical surfaces in an optical system.[3, 11]

Most of the spherical surfaces can be regarded as conic sections of revolution, even though some of them are fabricated as off-axis in practice. In the practical fabrication, it is more concerned about the deviation of an aspherical surface from the spherical surface. The aspherical sag is given in Eq. 1.

$$S(r) = \frac{r^2}{R\left(1+\sqrt{1-(1+K)\frac{r^2}{R^2}}\right)} + \alpha_4 r^4 + \alpha_6 r^6 + \cdots \text{[12]} \qquad \text{(Eq. 1)}$$

where S(r) is the sag—the displacement of the surface from the vertex, at distance r from the axis. The coefficients α describe the deviation of the surface from the axially symmetric quadric surface specified by R and K.

If the α_i are zero, then R is the radius of the curvature and K represents the conic constant, in which case, the surface is one of the general asphere decided by K.

Table 1.2: General asphere decided by conic constant K.

K<-1	K=-1	-1<K<0	K=0	K>0
Hyperbola	Parabola	Ellipse	Sphere	Ellipse

However, it is difficult to process workpiece with aspherical surfaces, especially for the large parts since small ones can be directed moulded in metal, glass or plastic. When using a rigid tool, there will always be misfit between the tool and workpiece surfaces. Changing the radius of the working tool could make the curvature of the tool closer to the workpiece surface, but never eliminate the misfit.

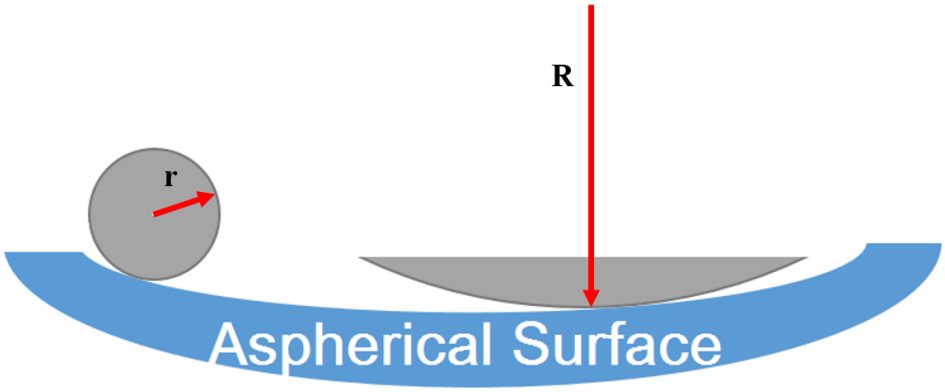

Figure 1.2: Schematic diagram of aspherical misfit, changing the radius of the tool could reduce but never eliminate the misfit.

In order to reduce the misfit, conformal tools are used, which can adapt to the aspherical or free-form workpiece surface. However, the deformation of the conformal layer is easy to cause the non-uniform pressure distribution during the processing. This leads to the uneven material removal and generation of MSF errors according to Preston's Equation.[13] This equation raised by Preston in 1927 gives the theoretical basis for estimation of removal rates in the manufacturing of surfaces.

$$\Delta h(x,y) = k \cdot v(x,y) \cdot p(x,y) \quad \text{(Eq. 2)}$$

where p(x, y) represents the pressure or force per unit area, v(x, y) is the velocity of the tool relative to the workpiece surface, k is a constant depends on the material of the tool and workpiece surface, and Δ h(x, y) is the rate of material removed.

1.2.3 Influence of MSF on functional surfaces

Spatial frequency has influence on the performance of functional surfaces. Low-spatial frequency refers to the surface form, which can be easily controlled or corrected by many surface processing techniques.[14-16] High-spatial frequency refers to the roughness or surface texture. Regardless of the complexity of the surface, high-spatial frequency could be improved by many surface finishing techniques, such as shear thickening polishing.[17, 18] However, current technique could not eliminate the mid-spatial frequency errors, even for the excellent smoothed optics, such as the Hubble Space Telescope primary mirror.[19] Therefore, in this section, the discussion is focused on influence of the mid-spatial frequency errors.

For an optical system with lower frequency errors (or form errors), the peaks and nodes of point spread function (PSF) are retained, while high frequency errors would scatter the light out of the system, decreasing the overall light intensity. These errors can be easily compensated later in image processing. However, the MSF errors erode the peaks and nodes of the point spread function[20], which reduces the signal to noise ratio and influences the contrast of the image (shown in **Figure 1.3** and **Figure 1.4**).

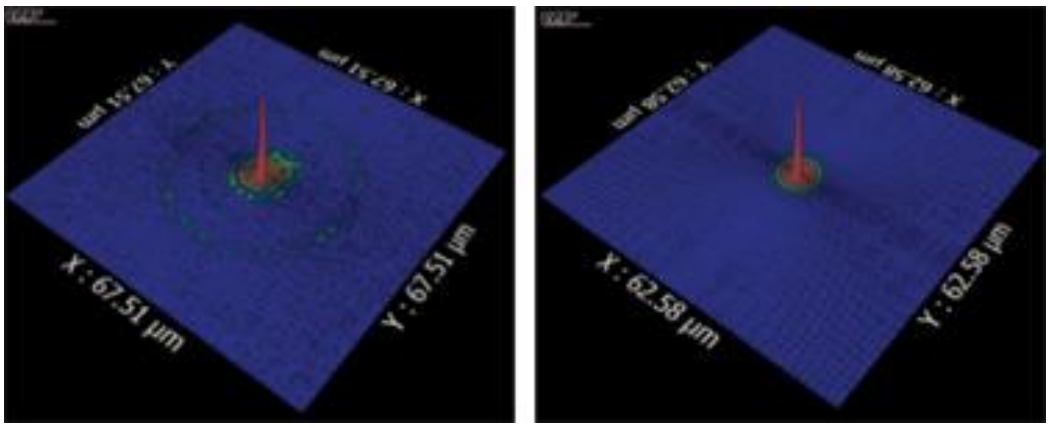

Figure 1.3: Point-spread function with uncontrolled and controlled MSF errors.[21]

By comparing the PSF result of a mirror with MSF error of 9 nm RMS and a perfect mirror in a simulation experiment, Krist and Hook have demonstrated MSF errors could significantly affect the image. The encircled energy of the PSF reflected by the perfect mirror is 30% more than the one reflected by the mirror with MSF errors.[22] It can be seen from **Figure 1.4**, how much the MSF errors could affect the contrast of the image.

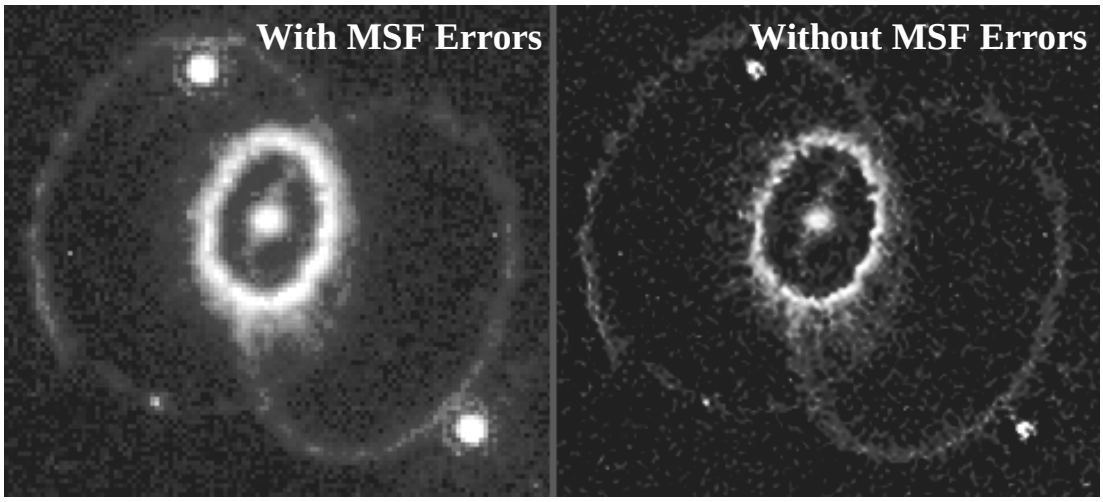

Figure 1.4: Images observed with and without MSF errors on the telescope mirror.[23]

According to the research of Jin Luo and co-workers, the MSF errors will also affect the quality of coating. In their report, a polished surface with MSF errors of 0.05 nm leads to the coating with PV of 25 nm and uniformity of 99.5%, while the polished

surface with MSF of 0.2 nm could only generate a coated layer with PV of 99 nm and uniformity of 98%.[24]

The performance of other functional surfaces is also affect by different ranges of spatial frequencies. Since the high-spatial frequency (roughness) and low-spatial frequency errors (surface form) can be reduced, the control of the MSF error becomes the key.

For example, the MSF errors have different effects for an aircraft turbine blade. According to Bai and Liu, the total pressure loss coefficient of cascade can reach up to 129% for blades with spatial frequencies comparing with smooth blades on an aircraft turbine, which leads to the increase of fuel consumption .[25]

Spatial frequency on the surface of as aircraft wing would leads to extra momentum losses and increase of the parasite drag. The overall lift force on an aircraft wing with spatial frequency could be reduced to only 50% of that on a well smoothed wing surface.[26] More influence of MSF errors on functional surfaces are listed in **Table 1.3**.

Table 1.3: Influence of MSF on functional surfaces.

Surfaces	Influence of MSF to functional surfaces
Optical surface	Affect the contrast of the image due to the light diffraction; reduce the uniformity of film coating for large optics.[24]
Surface of turbine	Loss of pressure coefficient and increase the fuel consumption.[25]
Aircraft wing surface	Leads to extra momentum losses in the boundary layer and reduce the lift force.[26]
Artificial joint surface	Increase friction during the limb movement.[27]
Mould surface	Reduce the surface texture and induce the same spatial frequency errors to the product surface.[28]
Silicon Carbide catalyst	Reduce catalyst efficiency.[29]

It is worth emphasising that human eyes are very sensitive to MSF errors. Apart from the influence of MSF errors introduced above, mid-spatial frequencies also reduce the customer appreciation and the potential value of the product.

1.3 Motivation

It has been introduced that mid-spatial frequency could significantly affect the performance of a functional surface, but the generation of the MSF errors can hardly be avoided during the manufacturing procedures, especially for the workpiece with large surfaces. Thus, it is critical to control the MSF in the manufacturing procedures. However, it is demonstrated in Chapter 2 that current technologies could not effectively reduce the MSF on functional surfaces with an economical method.

Grinding procedure usually introduce MSF errors to the functional surfaces. Some techniques lack the smooth ability to control mid-spatial frequencies, such as Bonnet polishing, Magneto-rheological finishing and Fluid jet polishing. Stressed lap or part polishing are not suitable for processing small functional surfaces and cannot process surfaces with steep curvature. Other methods are either time consuming or very expensive (Ion beam figuring, Reactive atomic plasma technology).

This research aims to develop an economical technique to effectively control the MSF errors on functional surfaces in as little time as possible.

1.4 Outline of this thesis

Chapter 1 articulates the problem for MSF control in manufacturing functional surfaces and briefly explains the importance to control the MSF to promote the performance of the functional surfaces.

Chapter 2 summarises various processing techniques for manufacturing functional surfaces and introduces the MSF errors control respectively. The metrology equipment used in this thesis are introduced, including their uncertainty and applications. The overview demonstrates that it is widely recognized that MSF errors can hardly be controlled during the processing of functional surfaces.

Chapter 3 describe the *grolishing* technique and implements this technique using rigid tools with loose abrasive to control mid-spatial frequency on flat surfaces.

Chapter 4 presents the grolishing technique using a rigid tool with bound-diamond pads to control the mid-spatial frequency with faster volumetric material removal rate and better surface texture.

Chapter 5 characterises the visco-elastic property a non-Newtonian material and introduces the simulation conducted in ANSYS atmosphere as guidance for research on aspherical surfaces.

Chapter 6 demonstrates that grolishing technique using non-Newtonian conformal tool could successfully control the mid-spatial errors on asphere and free-form surfaces.

Chapter 7 summarises the work, provides conclusions and suggests the future work.

This page is left blank intentionally

Chapter 2. Overview of Mid-Spatial Frequency Control in Manufacturing

2.1 Introduction

It has been discussed in chapter 1 that it is a critical issue to control mid-spatial frequencies in the manufacturing of functional surfaces because these MSF errors could significantly affect the performance of functional surfaces used in various fields.

This chapter reviews eight different manufacturing technologies for processing functional surfaces. The working principle of these technologies are firstly introduced and then compared based on their performance on different aspects in practical applications, especially for the ability for controlling MSF errors.

The advantages and disadvantages of these manufacturing methods are compared in this chapter. It concludes that current technologies could not effectively reduce the MSF on functional surfaces with a fast and economical approach and a new technique needs to be developed to fill this blank.

2.2 MSF Control for Manufacturing Techniques

In this section, different manufacturing methods for processing functional surfaces are introduced. Based on their working principles, the ability for controlling MSF errors during the fabrication are discussed and compared.

2.2.1 Grinding

The grinding procedure is commonly introduced to machining the part rapidly to the near-final shape, thickness, and curvature.[30] Compared to the fine-grinding or polishing process, this grinding procedure normally uses diamond impregnated tools. The exposed diamond particles on the grinding tool could remove material rapidly from the workpiece surface on the scale of tens of microns.[31, 32]

These grinding tools are classified into two configurations: cup wheels and peripheral wheels (shown in **Figure 2.1**). Cup wheels are used to process the surface of the part, while peripheral wheels are normally used for trimming the edge, sawing, and bevelling. The conventional grinding procedures are conducted by hand or on a single axis machine. This processing technique is suitable for generating spherical and flat surfaces. However, it is extremely time-consuming to fabricate a part with aspherical or free-form surface, because the surface needs to be occasionally measured during the fabrication procedure to guide further processing. The traditional surface grinding technique is done by hand and heavily depends on the experienced operators, which increases the processing risk and limits the part size.

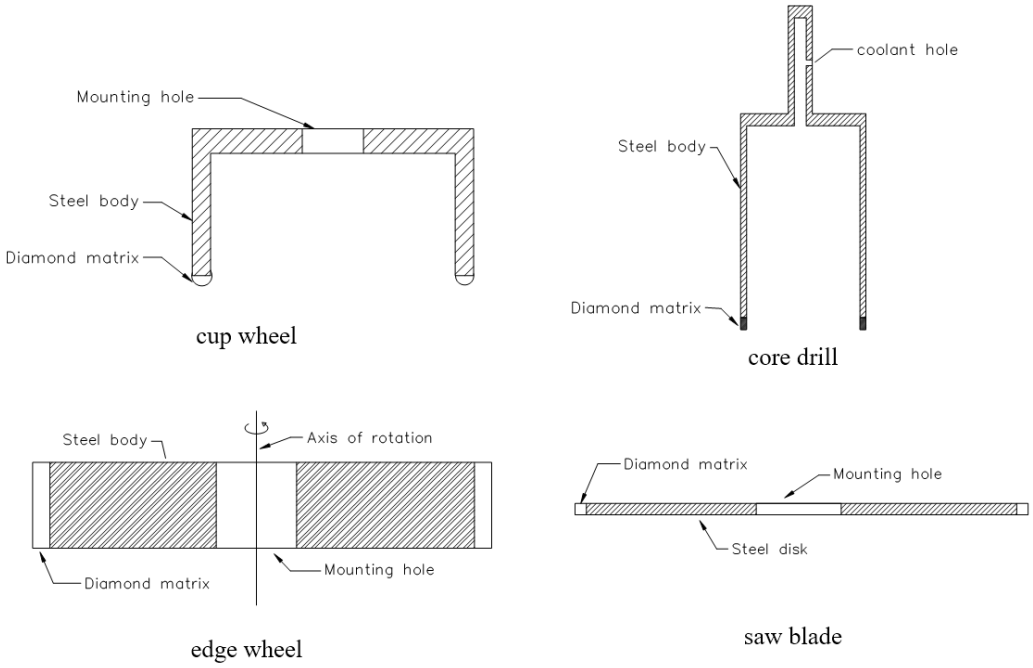

Figure 2.1: Diamond grinding wheels. There are two types of grinding tool used for processing functional surfaces: cup wheels and core drills are commonly used to generate curvatures and drill holes on the surface of the workpiece, while the peripheral wheels, with diamonds on their edges, are used for edging and sawing.[30]

In order to generate aspherical and free-form surfaces, these grinding tools are mounted on computer numerical controlled (CNC) machines with multiple axes, which makes the processing independent from the manual operation and improves the fabrication efficiency and extends size of the product.

For example, BoX grinding machines, research and development by Cranfield University[33-35], have been used for processing 1.4 m off-axis aspherical segments for the European Extremely Large Telescope (EEL-T).

The grinding machine was designed with high static and dynamic loop stiffness to obtain low subsurface damage depth. The repeatable error is control within micron level to ensure the accuracy of surface form. Unfortunately, due to its material removal

mechanism, regardless of the positioning accuracy, it is inevitable to introduce MSF errors to the workpiece surface.

Figure 2.2: Cranfield University BoX grinding machine.[33]

Diamond turning used a single point diamond as a cutting tool to process the part surface. The part is turned around the diamond-tipped lathe tool during the fabrication. This technique has a few advantages, including sub-nanometre level surface finishes, which could be directly measured by an interferometer, and sub-micrometre form accuracies. The term ‘single point diamond turning (SPDT)’ is also used sometime to express the processing.[36-38]

Unfortunately, this technique also has a problem for the mid-spatial frequency control on part surfaces. Especially for processing a large part, when the heavy part is rotating around the diamond tool, the vibration would affect the uniformity of local material removal and lead to MSF errors.

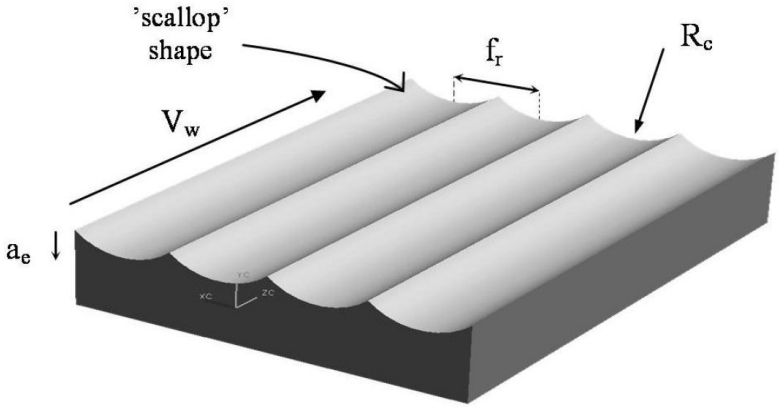

Figure 2.3: MSF errors generated by the grinding procedure.[39]

Cheung and Lee[39] generated a grinding model to estimate the surface profile after diamond turning in 2000. This model was based on a surface simulation generated by grinding using a conventional cutting tool. The radius of the conventional grinding cutting tool was replaced by the cutting radius of diamond tuning. The "scallop" shape generated by this grinding model is shown in **Figure 2.3**.

2.2.2 Lapping

Lapping is a controlled mechanical sanding or polishing process in which two surfaces are rubbed together with an abrasive between them, by hand movement or using a machine.[40, 41]

Two kinds of lapping using different tools are introduced in this section. One uses pitch tool combined with a slurry abrasive of cerium oxide and the other uses metal tools working with aluminium oxide. In the lapping process, the pressure and dwell time are controlled by hand, which makes the accuracy and efficiency of the process dependent upon the experience of the operator.

2.2.2.1 Lapping with pitch tools

A pitch layer is one of the most historic surfaces for a polishing tool, and it has been suggested that Isaac Newton (1642-1727) might be the first person to use a pitch lap to fabricate an optical lens in 1668.[42-44] Pitch is a combination of different viscoelastic polymers, which could be natural or extracted from plants, petroleum, or coal tar. Pitch has a low softening point of 55-70℃ and a much lower hardness compared with silicon carbide, glass or metal. Therefore, during processing, a pitch tool could closely contact the surface without changing the shape of the part.

The pitch tools are usually applied together with cerium oxide working on spherical and plane surfaces. The material is removed using a combination of mechanical motion and chemistry to produce surfaces with surface texture to nanometres.[45]

The pitch tool is widely used to remove mid-spatial frequency in the polishing process due to its good smoothing ability. The surface form may be changed in the lapping procedure, but it can be easily corrected again in corresponding polishing techniques.

However, the material removal rate for lapping with pitch tool is low. It commonly takes hours to remove about 1 micron depths of material from a glass part depending on the size of the tool and part surface. In addition, due to the lack of flexibility, a pitch tool can hardly be conformal to an aspherical or free-form surface. Although its visco-elasticity allows the pitch to deform slowly to adapt to the surface, but in practical application for generating aspherical or free-form surfaces, the misfit can hardly be completely eliminated, which easily introduce MSF errors to the workpiece surface.

Figure 2.4: Lapping process using pitch tool and cerium oxide.

For processing metal surfaces, different slurries, including oxidiser agents and different acids[46, 47], need to be applied to the lapping procedures. The material removal is also based on the chemical mechanical mechanism.

2.2.2.2 Lapping with metal tools

Using metal tools with aluminium oxide can substantially increase the material removal rate for lapping process. The size of the abrasive usually ranges from 3 microns to 50 microns, and the volumetric removal rate could be improved up to a few hundred times faster than the pitch tool.

However, the rough abrasive would reduce the quality of surface finishing. Based on the author's experiment results (shown in Chapter 3) and publications by Bennett, the surface texture (Surface Average) after lapping by aluminium oxide ranges from a few hundred nanometres to one micron.[48]

Based on the features described above, this technique is used following the grinding procedure to control the MSF errors generated and rapidly remove material from the layer including subsurface damage.

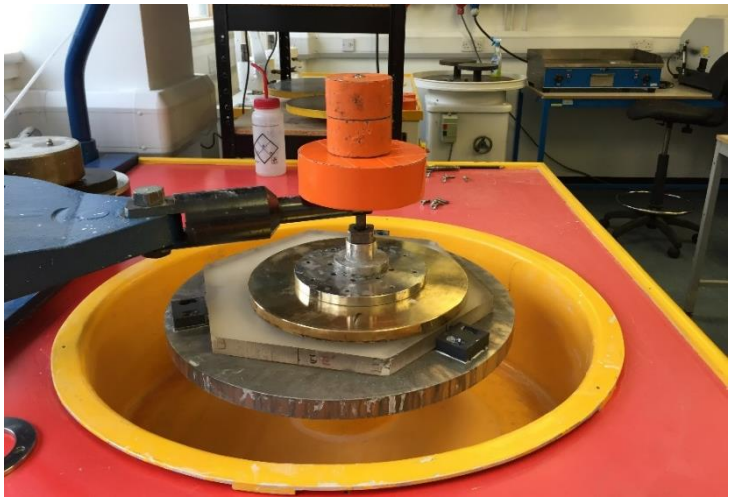

Figure 2.5: Lapping procedure using a flat brass tool working on a piece of borosilicate glass.

Similar to the pitch tool, the lapping tool made of metal also lacks the ability to adapt to an asphere or free-form surface. The material is rigid and could only be applied to control MSF errors on spherical or flat surfaces.

2.2.3 Bonnet polishing

An inflated bonnet tool was first applied in the 'Precessions' polishing technology developed in the early 1990s and commercialised by Zeeko Company in the late 20th century.[49-51] This technology is a deterministic, ultra-precision surfaces processing technique based on computer controlled polishing technique for prepolishing and correcting 2D and 2½D form.[16, 52-62] This technique was applied to processing telescope mirrors[63, 64] and other functional surfaces.

Zeeko IRP series polishing machines are shown in **Figure 2.6**. The size of the workpieces ranges from 50 mm to 1600 mm in diameter. IRP 2400 and IRP 3000 are still in research and development stage.

Figure 2.6: Zeeko IRP polishing machines, ranges from 50-1600 mm (IRP 2400 and IRP3000 are still in research and development).

In the 21st century, this technology had breakthroughs in the field of edge control and super-smooth surface finishing for large optical and mechanical surfaces.[64, 65] But this technology does not show advantages for the MSF control for its flexibility of the tool.

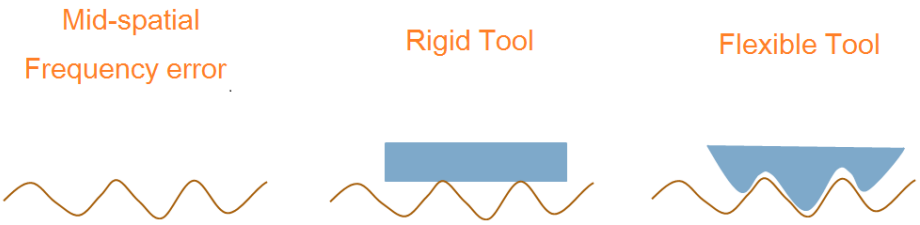

Figure 2.7: Schematic diagram of the problem for MSF error control.

It is shown in **Figure 2.7** that a flexible tool could easily conform to the workpiece surface and removal material uniformly during the processing. But this process keeps the original topography of the surface and cannot remove existing MSF errors. A rigid tool, on the other side, could bridge over the peaks of surface errors and remove the mid-spatial frequency.

To solve this problem, ‘grolishing’ was introduced as the intermedium procedure to control MSF errors. It was reported by Hongyu Li and Guoyu Yu[8, 9] that a brass button glued on the inflated bonnet was used to control mid-spatial frequency on large optical parts, which is shown in **Figure 2.8**.

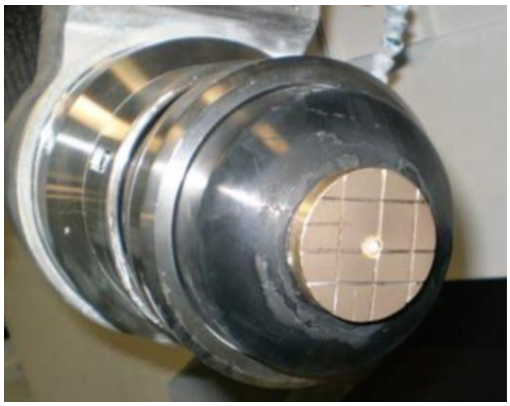

Figure 2.8: Grolishing tool mounted on a polishing machine.[8, 9]

It was discussed in the article that the tool clearly exhibits aspherical misfit, which is mainly caused by two reasons: i) the misfit as the tool moves along the tool path; ii) the misfit caused by the rotation of the tool. The first can be effectively reduced by the natural tool wear and the second may be managed by using the optimised size of abrasives, which is sufficiently larger than the misfit.

This method is not suitable for processing free-form surfaces and aspherical surfaces with steep curvature. Because on these working surfaces, the tool does not have enough time to wear and adapt to the surface. If reducing the transverse time, it is likely to leave water mark on the part surface and seriously change the surface profile.

2.2.4 Stressed lap polishing

Stressed lap polishing was a computer numerical controlled surface processing technology firstly developed by the Steward Observatory Mirror Laboratory at

University of Arizona[66, 67]. This method enables to process an aspherical surface using a rigid tool by bending and twisting the edge of the tool to deform to a converse form to the local area of the working surface. The stressed lap comprises of a metal disk with actuators attached to top and coated to the lower face with the traditional squares of pitch.[14] During processing, the tool is pressed against the working surface, and the actuators induce the correct change in form according to the pre-computed programme so that the polishing tool can conform to the local surface of the workpiece surface.

The stressed lap polishing enables to process a large aspherical surface using a rigid polishing tool, which could effectively removal material and a large range of spatial frequency errors. This technology has been applied as a core technique in the fabrication of segments for 25 m Giant Magellan Telescope (GMT).[68-70] The final surface texture could be achieved better than 1 nm using this technology.[71]

The stress lap is very complex and needs to be carefully maintained. The tool is designed especially for each part and needs to be re-built for a new process. This technology is especially developed for processing large optical surfaces. It could produce segments for GMT with 15 mm peak to valley aspheric departure[71], but have difficult to processing the off-axis aspherical surfaces with deeper curvature or complex free-form surfaces.

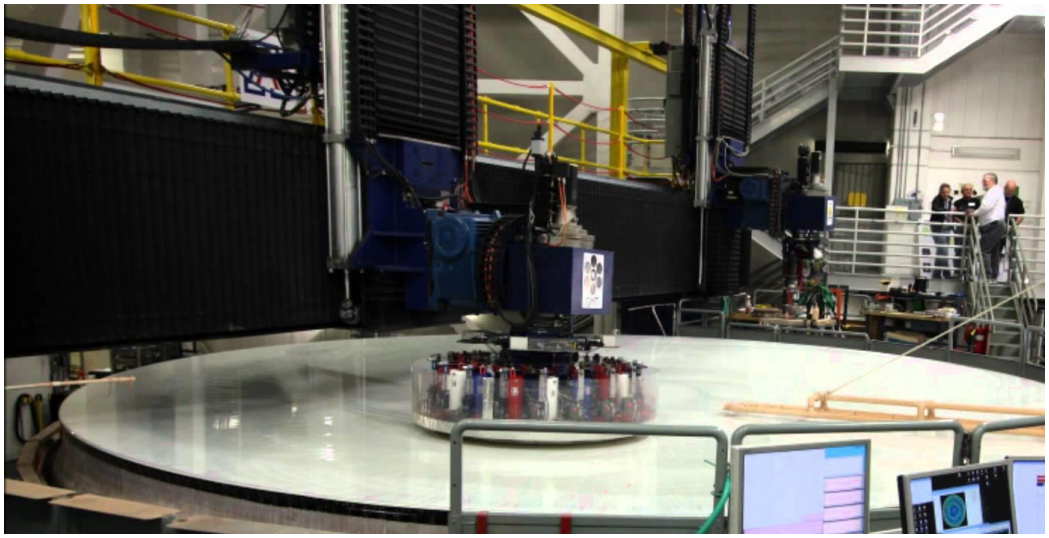

Figure 2.9: A stressed lap tool used for polishing an 8.4 m diameter segment for the Giant Magellan Telescope.[69]

MSF errors could be effectively be removed using the stressed lap for it natural smoothing ability. But due to the complexity of the polishing tool, the possible range of the tool size is limited and not suitable for processing small parts.

2.2.5 Stressed mirror polishing

Unlike stressed lap polishing, the stressed mirror polishing is exactly the opposite approach- the mirror is deformed during the process rather than the tool.

This technology was first invented by Lubliner and Nelson to fabricate nonaxisymmetric mirrors in 1980.[72, 73] Stress is applied to a mirror blank and deforms elastically to generate a spherical surface, which could be polished directly by a pitch tool with the same radius curvature of the part. As the misfit has been eliminated, this procedure could effectively control the MSF errors left by previous processing. According to the computing results, when the force is released, the part surface could relax back to the desired asphere or free-form surface.

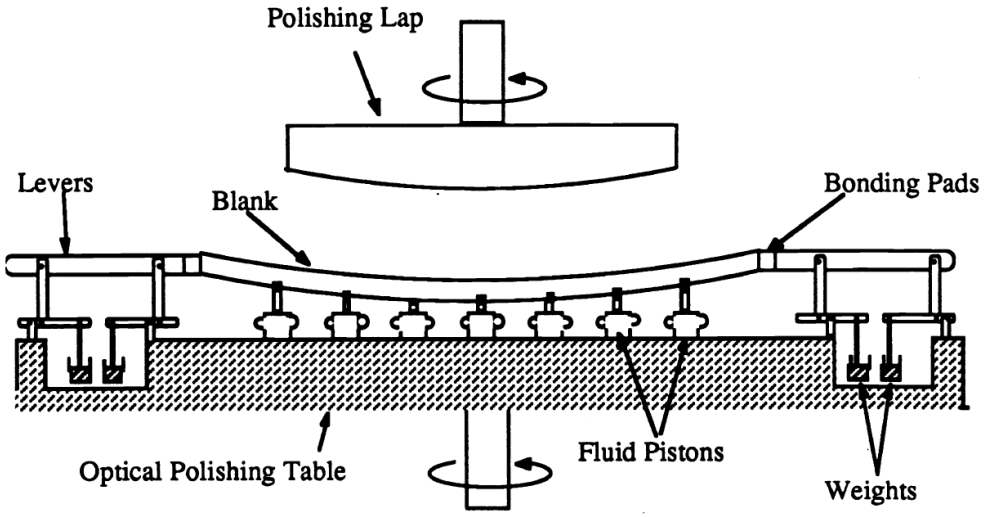

Figure 2.10: Stressed mirror polishing setup used for processing Keck's Segment.[74]

A fixture used in stressed mirror polishing is shown in **Figure 2.10**. During the fabrication procedure, a number of fixtures are applied under the part to bend the mirror to a spherical form. This technology has been successfully applied for producing segments for the primary mirrors of Keck and European Extremely Large Telescope (E-ELT).[15, 75] However, the high frequency error is very difficult to bend, thus reducing the overall surface form accuracy. It was reported that the surface form error of more than 200 nm RMS was achieved after the stressed mirror polishing. The residual error was corrected using ion beam figuring technology.[76]

Similar to the stressed lap polishing, the stressed mirror polishing procedure does not introduce new mid-spatial errors and could effectively remove these errors. But this technology has limitation to manufacturing part made of metal, plastic or other material with plasticity. Because these materials could not relax to the original form and will generate internal press during the manufacturing procedure. Even for workpieces made of optical glass, this technology also has requirements for the shape of the part. Usually,

the thickness of the workpiece needs to be considerably smaller than its length and width. Otherwise, the glass may break during the stressed procedure.

2.2.6 Magneto-rheological finishing (MRF)

Magnetorheological finishing (MRF) is firstly invented by a research team led by William Kordonski[77, 78] at Luikove Institution of Heat and Mass Transfer in the late 1980s. It was then developed by Jacob[79-81] and co-worker at the Centre for Optical Manufacturing since 1993 and commercialised by QED Technologies Inc.[80]

The MRF is a deterministic method for processing functional surfaces with a variety of materials, including glass, ceramics and typical semiconductor materials. The MRF technology could control the accuracy of the surface form to less than 50 nm and surface roughness less than 1 nm.[82]

MRF is a small tool surface finishing process, which combines with metrology with interferometry, precision equipment and numerical computer control. This technology bases on a magneto-rheological fluid with Nano size abrasive particles (typically carbonyl iron). The polishing fluid could be stiffened by a controlled magnetic field. Material is removed in the area where the optic is immersed into the stiffened fluid ribbon (or removal function). Usually, a raster tool path is used for the surface processing, and it could also be completed by rotating the working surface through the polishing fluid.[83-85]

This technology has great advantage for improving the surface texture and can be characterised to high precision. The stiffened fluid could easily conform to complex surfaces, providing the flexibility for processing workpiece with spherical, aspherical and free-form surfaces.

However, this technology is not suitable for form correction for its low material removal (typical of 0.033 mm^3/min)[86]. The workpiece needs to be nonmagnetic to avoid the negative affection to the magnetic field that control the fluid. The safety issue and high cost of Magneto-rheological fluid are also the disadvantages of MRF.[87]

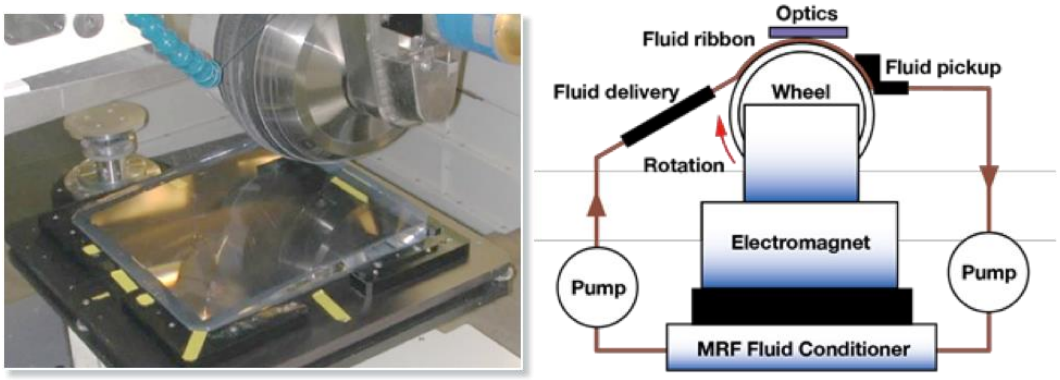

Figure 2.11: The procedure of MRF processing.[83]

This technology is not commonly used for controlling MSF errors. This process technique may introduce new mid-spatial frequency because of the overlap of the influence functions.[88] If it is very demanding for controlling MSF errors, pitch tool is commonly used after this processing. A simulation has proved that the MSF may be further restrained by reducing the track spacing of the raster tool path[89], but it will significantly increase the overall processing time.

Research has been conducted by Hu and co-workers [90], using a novel random tool path to restrain the MSF errors on a flat work piece with 98 mm in diameter. No obvious MSF errors is found after one MRF polishing. This result only demonstrates that using a random tool-path may not introduce new MSF onto the surface, but not remove existing mid-spatial frequencies.

2.2.7 Fluid jet polishing

Fluid jet polishing (FJP) technology was first developed at Delft University at 1998.[91] It is a surface processing technique, which is capable of making form corrections and improve the surface texture of workpieces made of glass or other materials. During the process procedure, liquid and fine abrasive are pre-mixed by a vibrator and guided a stream of slurry to the hand holder, and then sprayed from a nozzle to the workpiece surface at a low pressure.[92] The material is removed by collision and shearing effect between the abrasive and the part surface. The process is shown in **Figure 2.12**.

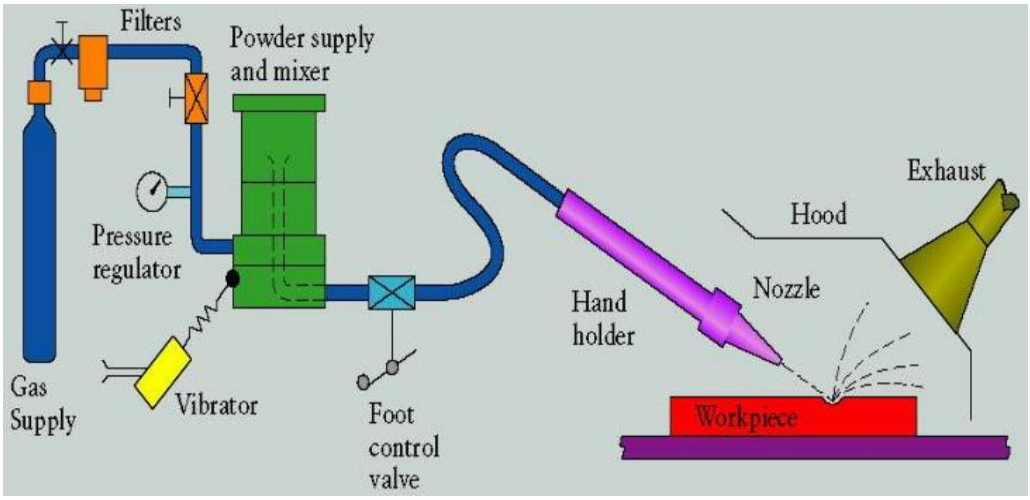

Figure 2.12: Overview of the Fluid-jet processing setup.[93]

It was reported that using the fluid jet polishing technology the surface roughness of the pre-grinded glass surface could be reduced from 475 nm to 5 nm. For the pre-polished workpiece, the surface texture could be further reduce to 1.6 nm.[94] It was also demonstrated that this technology is suitable for polishing complex surfaces for it is not affected by misfit problems.

The material removal rate of this technology is low so that it is commonly used at the final surface finishing to improve the surface roughness. The fluid jet polishing cannot

also precisely control the influence function during the processing, which reduce the stability of material removal rate. Thus, this technology is not suitable for form correction or edge control.[95]

This technology has been applied to Magneto-rheological finishing, which provides a long standoff distance between the workpiece surface and the nozzle. It enables to process surfaces with a steep curvature, which is hardly reaching using a MRF wheel based tool.[86] The technology is most attractive for the finishing of complex surfaces, such as freeform optics, steep concaves or cavities. This technique also increases the material removal rate as such fluid flow may generate sufficient surface shear stress in the regime of chemical mechanical polishing.[96]

Similar to the MRF process, the fluid jet polishing lacks the smooth ability and was considered that it is not suitable for MSF control. But it was claimed by A. Beaucamp[97] and co-workers that marks left by diamond turning could be removed by fluid jet polishing technique applied on a Zeeko polishing machine. The analysis results of power spectrum density (PSD) is shown in **Figure 2.13**.

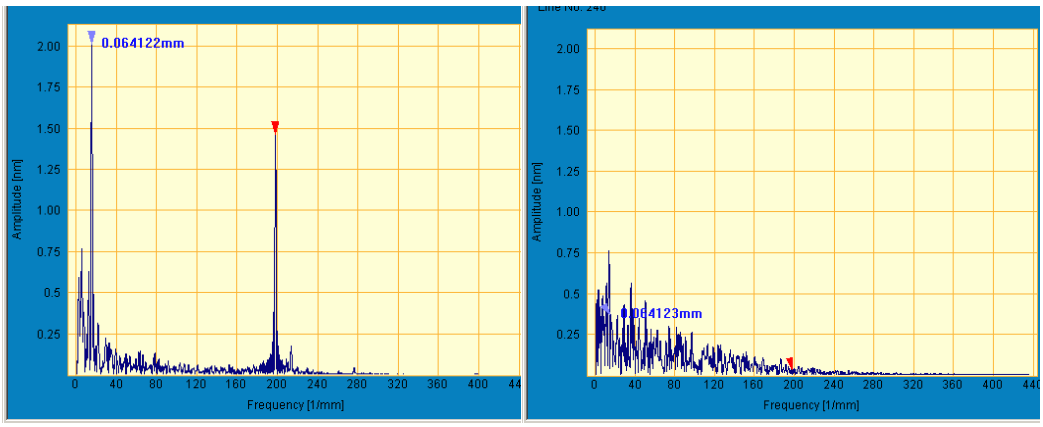

Figure 2.13: PSD analysis of part surface before (left) and after (right) fluid jet polishing.[97]

As can be seen from **Figure 2.13** that surface frequency at 200/mm has been significantly reduced by the fluid jet polishing procedure. As introduced before, the

definition of the mid-spatial frequency is a vague concept, and the frequency range depends on the parameters of the practical application, such as surface size, tool size, track spacing and so on. For a surface topography processed by diamond turning is already very smooth, so that an error with frequency of 200/mm could be regarded as mid-spatial frequency. However, as explained before in Chapter 1, for most of the surface processing technologies, the mid-spatial frequency ranges from 0.02/mm to 1/mm[8, 9]. 200/mm is usually regarded as high frequency and can be removed by other conventional polishing methods.

2.2.8 Ion beam figuring

Ion beam figuring is a surface processing technology for variety of applications using a type of charged particle beam consisting of ions. It could be divided into ion beam sputtering, ion beam removal, ion beam adding and reactive ion beam figuring.[98, 99]

2.2.8.1 Ion beam sputtering

Ion beam sputtering is typically used for silicon-based semiconductor manufacturing. In order to create certain patterns on a substrate in nanometre scale. A layer of photoresist is deposited averagely on the target surface. Then an ion beam is used to bombard the target surface through a mask with certain pattern. For a positive photoresist, the processed area could be easily removed in the following chemical process. Thus, the pattern is formed on the substrate. It is similar to spraying paint to a substrate but using individual atoms to ablate a target.

2.2.8.2 Ion beam removal and adding

A focus ion beam is used for ion beam removal and ion beam adding procedures. Both of these techniques have be used for processing optical surfaces.

As shown in **Figure 2.14**, in ion beam removal technique, the surface errors could be removed by a raster scan of a focus ion beam across the part surface, according to the dwell time map. The material could be removed from the bombardment between accelerated ions and the atoms on the part surface. This method has been used for more than 50 years.[100-102] Early experiment has been conducted by Meinel and co-workers to figuring optical surfaces in 1965.[102] The surface roughness of the surface processed by this technology could be reduced to 5 nm RMS. The ion beam removal technique has been successfully applied on the final surface finishing on the primary mirror of Keck Telescope.[103]

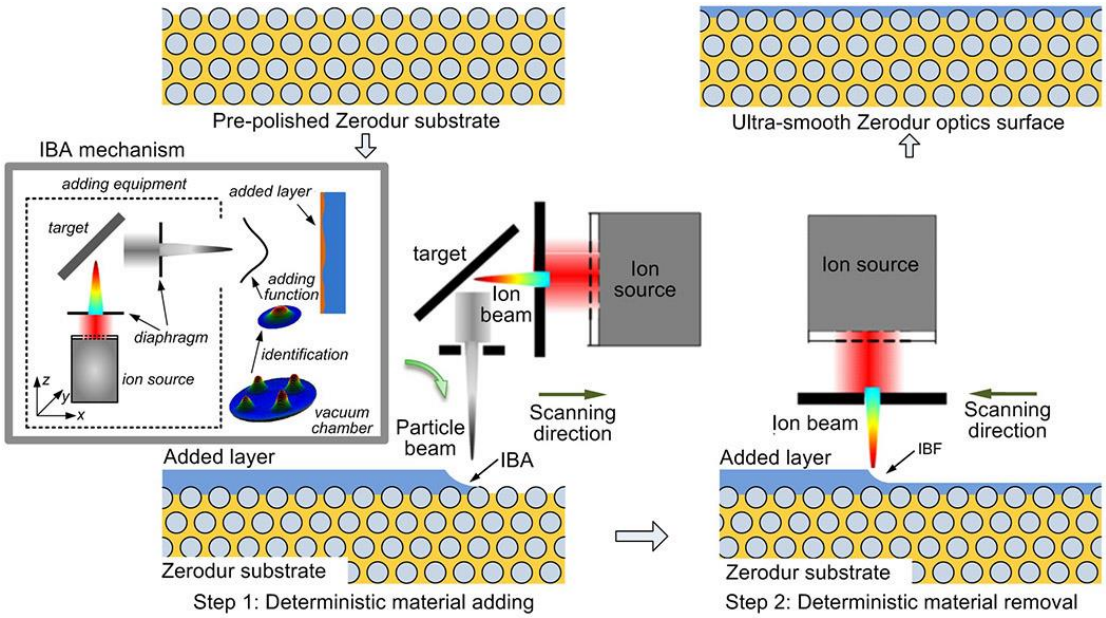

Figure 2.14: The schematic illustration of ion beam adding and removal process.[104]

On the other side, instead of removal material from the working surface, the focused ion beam could also be used to add material to deterministically to the local low position on the functional surfaces to get rid of surface errors, which is shown in the **Figure 2.14**. It has been reported that the ion beam adding technology applied on optical surfaces could maintain and even improve the original surface form.[104]

The material removal or adding rate is extremely slow, which makes this technology not able to change the form of the surface on a large scale. For example, it took more than ten days to correct the residue error for one of the segment for Keck Telescope after polishing procedures.[74] In practise, ion beam removal and adding is usually used for final surface finishing. The cost of this technology is also very expensive.

2.2.8.3 Reactive ion beam figuring

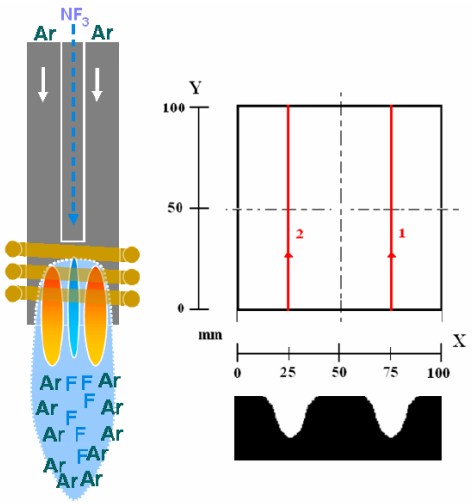

Figure 2.15: Principle of reactive ion beam figuring.[105]

Reaction ion beam figuring use a stream of reactive atoms, which is directed to the working surface and produce volatile gas, to assist the material removal procedure. It is also called Reactive Atomic Plasma Technology (RAPT) in some publications. It is an important extension that uses chemical reactivity to enhance the physical sputtering effect. It has been claimed by Arnold that using reactive atomic plasma technology, removal depths of some 10 μm can easily be achieved.[106]

Plasma etching is also a typical method used to process semiconducting materials that used for the fabrication of electronics. Small features can be etched into the surface of the semiconducting material to increase the surface area or providing a more efficient

electrons pathway. This could promote the efficiency or enhance certain properties when used in electronic devices.[107]

2.2.8.4 MSF control

Ion beam figuring technique does not introduce new mid-spatial frequency to the working surface for its ability to remove or add materials at the molecular level. Until now, the ion beam figuring is not regarded as one of the optimal methods for controlling MSF errors on the surface. This is probably because that it is too expensive and time-consuming. Ion beam sputtering has the potential ability to smooth a functional surface, but also degrade the surface form and reduce surface roughness.[108] Furthermore, the alignment seems to be another problem for the practical application. It is extremely difficult to ensure the alignment accuracy within a few nanometres. Otherwise, the MSF errors can never be completely removed.

2.2.9 Comparison of the manufacturing techniques

In this section, the advantages and disadvantages of these manufacturing technologies for processing functional surfaces are compared below in **Table 2.1**. The ability for mid-spatial frequencies control is listed separately in the table.

Overall, it is difficult to eliminate the mid-spatial frequencies in the manufacturing of asphere and free-form surfaces in a fast and economical way using current techniques.

Table 2.1: Comparison of different manufacturing techniques.

Manufacturing Techniques	Advantages and Disadvantages	MSF Control
Grinding	Fast material removal rate; Variety of materials. Subsurface damage; Introduce MSF.	Cannot avoid or remove MSF errors; it also introduces subsurface damage.[33, 35]
Lapping	Good surface texture for pitch tool; High material removal rate for metal tools. Serious misfit for processing aspherical surfaces	Could effectively control MSF in spherical or flat surfaces, can't be applied to aspherical or free-form surfaces.[48]
Bonnet Polishing	Good surface texture; High surface form accuracy; Large rang of part size. Too flexible to remove MSF errors.	Does not introduce MSF, but can remove existed MSF errors.[9, 64]
Magneto-rheological Finishing	Good surface texture and surface form accuracy. Low material removal rate; Non-magnetic part; safety issue;	Time consuming to control MSF errors.[89]
Fluid Jet Polishing	Good surface texture and surface form accuracy. Low material removal rate, unstable tool influence function.	Effectively control spatial errors at high frequency; time consuming to control MSF errors.[82]
Stressed Lap Polishing	High material removal rate and surface texture. Does not applies to small part, specially designed tool for each part.	Effectively remove MSF errors, but suitable for small parts.[14]
Stressed Mirror Polishing	Good material removal rate, good stability. Requirement for workpiece shape and limited material selection.	Effectively remove MSF errors, but limited to the size and shape of the parts.[15]
Ion Beam Figuring	Very good surface texture and form accuracy. Expensive and time consuming.	It has the ability to control MSF errors, but extremely time-consuming and costly.[104]

2.3 Measurement Equipment Used in This Thesis

2.3.1 Talysurf Profilometer

Profilometer is an instrument to measure a surface's profile, in order to quantify the form and roughness of the surface. In order to measure the surface of large optics, a Form Talysurf Profilometer[109], as can be seen in **Figure 2.16**, is used for its long transverse range of 300 mm. Stitching software has been developed in-house, which has been used to measure the form of parts up to 500mm diameter. The measurement accuracy of this equipment reaches 125 nm, which delivers form as well as surface finish measurement capability for precision forming and other application.[110]

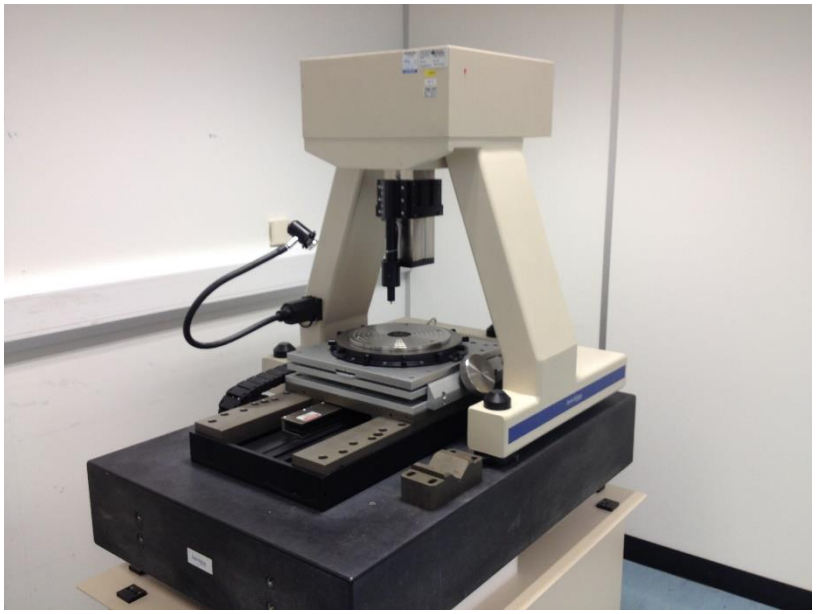

Figure 2.16: Long Range Form Talysurf Profilometer.

This equipment is typically used to measure the surface profile and roughness of workpieces before polishing. The system noise is less than 2 nm and the overall noise of the measurement results depends on the roughness of the surface.[109] In order to observe MSF errors from the results, the noise needs to be controlled below the PV of

the MSF errors. In this case, the MSF errors with PV larger than 125 nm could be measured by this equipment.

2.3.2 4D interferometer

Interferometer is a metrology equipment using the technique, in which electromagnetic waves are superimposed causing the phenomenon of interference in order to extract information.[111] Conventional interferometry is very sensitive to vibration, moving parts and turbulent airflow, because the data are taken at different times and vibration causes the phase shifts between the data frames to be different from what is desired.[112] In order to reduce the vibration effects, in 4D interferometer, all the 4 phase shifted frames are taken simultaneously, which is shown in **Figure 2.17**.[113]

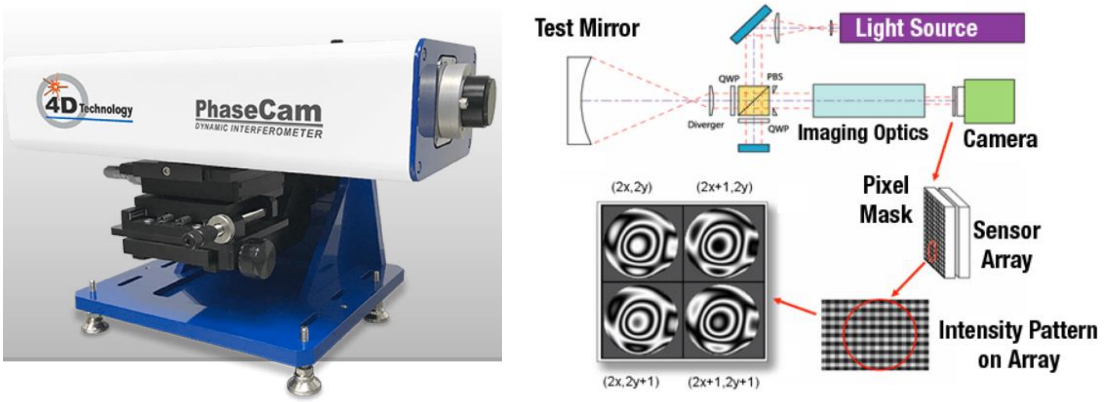

Figure 2.17: 4D interferometer and its working principle to reduce vibration effects.[113]

The accuracy of the measurement for RMS of this equipment could achieve 10 nm.[112] It requires good surface finishing (Sa less than 100 nm) of the part to be measured. Therefore, the surfaces are usually polished to achieve good surface texture before they are measured by this equipment.

2.3.3 White light interferometer

White light interferometer is a metrology equipment based on a non-contact optical method for surface height measurement. It is named by the fact that it relies on spectrally-broadband, visible-wavelength light (white light). The measurement accuracy of this equipment is 20 nm in RMS.[114] Due to the small detection range (less than 1 mm^3), it is commonly used for the metrology of roughness.

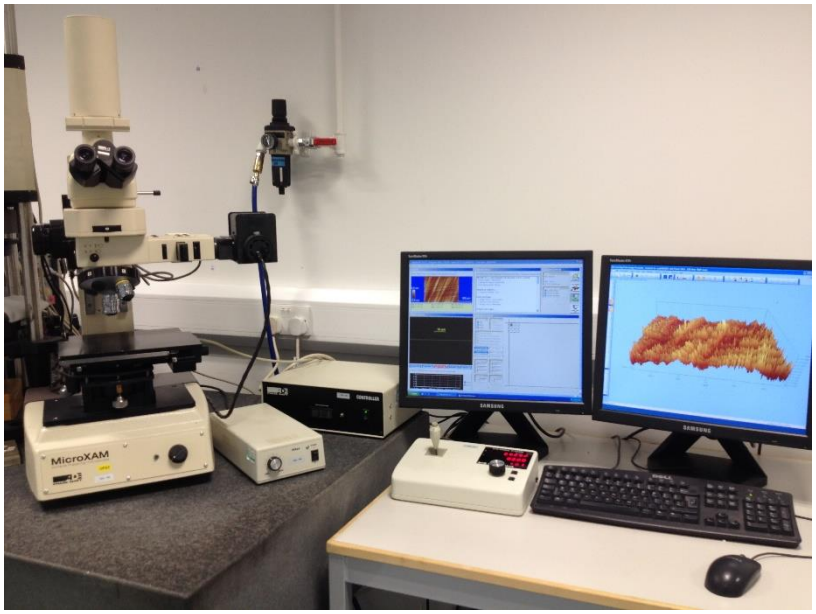

Figure 2.18: White light interferometer (left) and analysis system (right).

2.3.4 ROMER Absolute Arm

ROMER Absolute Arm is a product from *Hexagon Manufacturing Intelligence*.[115] It is a portable measuring arm, which does not require referencing before measuring. It is shown in **Figure 2.19**.

Figure 2.19: ROMER Absolute Arm.[116]

This equipment has a point repeatability of 16 microns and volumetric accuracy of 23 microns[117], which gives it the ability to measure the surface profile of a complex surface and providing directions for the alignment of workpieces and tools.

2.4 Summary

The metrology equipment to be used in this thesis are introduced in this chapter. The accuracy specification and relative application of these equipment are descripted.

Eight different manufacturing technologies for processing functional surfaces have been introduced. Due to their different processing principles, the performance also varies in different key indicators, including material removal rate, surface roughness, surface form accuracy and cost. However, all of these techniques do not have the ability to control MSF errors for aspherical and free-form surfaces with different size in a fast and economical way.

The grinding process could shape the workpiece surfaces close to the required form quickly, but also introduced MSF errors, which could significantly affect the performance of functional surfaces and needs to be reduced by other techniques.

Conventional lapping could effectively reduce MSF errors, but are limited to flat or spherical surfaces. For asphere or free-form surfaces, this technique would introduce new MSF errors due to the misfit between workpiece and tool surfaces. Stressed tool and stressed mirror polishing could be applied to aspherical surfaces to control MSF errors, but they cannot be used for all the parts. The application is limited by the requirements of the workpiece size and shape.

MRF and fluid jet polishing could remove residual MSF errors, but the material removal rate is very slow, which increase the overall processing time. Ion beam figuring techniques could produce surfaces with good surface texture and form accuracy, but its application for MSF control is restricted by its high cost and problem of alignment before processing.

The bonnet polishing using a flexible tool lacks the smoothing ability and cannot remove MSF errors left by previous processing procedures. The grolishing technique developed from it could reduce the mid-spatial frequency, but it is also very easy to introduce new MSF errors to the surface because of the misfit problem. Thus, a new technique need to be developed to keep the tool's smoothing ability and reduce the misfit between workpiece and tool surfaces, which is introduced in the following chapters.

This page is left blank intentionally

Chapter 3. Mid-Spatial Frequency Control with Loose Abrasive on Flat Surfaces

It has been introduced in Chapter 2 that mid-spatial frequency (MSF) is a critical issue for surface processing, as it is difficult to be removed by polishing methods. Most of the CNC polishing techniques have a soft tool interface to improve the surface finishing. However, it is difficult to control the MSF using such tools.

In this chapter, a polishing experiment is introduced firstly to demonstrate the problem of using a flexible tool to control MSF errors. Then, grolishing experiments using rigid tools are presented to successfully removed MSF errors on a flat surface. The PV of the mid-spatial is controlled within 10 nm.

During the manufacturing of functional surfaces. A layer of material needs to be removed before form-correction polishing to eliminate the sub-surface damage (SSD) introduced by the grinding procedure. This procedure is usually called pre-polishing and could be time-consuming limited by the material removal rate of the polishing procedure. Grolishing experiments introduced in this chapter also aims to increase the volumetric material removal rate to reduce the overall processing time.

Rigid tools attached with different metal buttons are compared in the grolishing experiments regarding the material removal rate and surface texture. Two material removal mechanisms are introduced in this chapter to explain the results.

3.1 Mid-spatial Frequency Control with Flexible Tools

3.1.1 Aim

It is widely recognized that it is difficult to remove mid-spatial frequency using a flexible tool. A few experiments have been conducted to support this opinion. [8, 9] As this is one of the most important bases of this thesis, in this section, experiments were repeated to validate this conclusion.

3.1.2 Experiment procedure

In this experiment, a flat hexagonal borosilicate glass (with corner to corner dimension of 400 mm) was used. Mid-spatial frequencies were generated on the surface on purpose. It was then polished using Zeeko IRP 600 by an inflated flexible bonnet tool. The surface profile of the part was measured before and after the polishing.

3.1.2.1 Generating mid-spatial frequency

Firstly, mid-spatial frequencies were generated using a rigid cast iron tool, with the diameter of 100 mm, mismatching to the part surface. Raster tool path was used with 10 mm track spacing.

3.1.2.2 Metrology before polishing

The surface profile of the part was then measured before polishing. A Form Talysurf profilometer, introduced before in Chapter 2, was used, which is shown in **Figure 3.1**. This equipment has measurement accuracy of 16 nm and a traverse range of 300 mm.

Figure 3.1: Metrology using long Range Form Talysurf Profilometer.

3.1.2.3 Polishing

A Zeeko IRP 600 was used for polishing the part, trying to remove or reduce mid-spatial frequencies. A raster tool path was used with track spacing of 1 mm and perpendicular to the tool path for generating mid-spatial frequencies. A polyurethane polishing cloth was attached to a bonnet, and used in this experiment. The experiment was conducted with the following parameters shown in **Table 3.1**.

Table 3.1: Parameters for the polishing experiment.

Surface feed	Slurry	Spindle speed	Bonnet size	Time	Process angle
1000 mm/min	Cerium oxide	800 rpm	80 mm	2 hours	15˚

Figure 3.2: Polishing procedure trying to remove mid-spatial frequencies.

3.1.2.4 Metrology after polishing

The part surface was measured again after the polishing experiment by the long-range Form Talysurf Profilometer. The results were compared to find out whether the mid-spatial frequencies could be attenuated or removed by a bonnet flexible tool.

3.1.3 Results analysis

The surface profile of the part before and after the polishing is shown in **Figure 3.3**. The polishing spot did not contact the edge of the measured area so that the edge was considered as reference position. It was clearly shown that during the polishing procedure, more than 2 micron depth of material had been removed from the centre area of the part. However, the mid-spatial frequency content was not obviously reduced. Peaks and valleys had remained on the surface, which validate the conclusion that flexible bonnet tool can hardly remove mid-spatial frequencies from a workpiece surface. It is due to the compliance of the tool to the local surface that gives bonnet tool the ability to conform to the spatial frequencies.

The PSD analysis in **Figure 3.4** shows that the peak appears at 10^{-1}/mm before and after the polishing processing, which also demonstrates that flexible tool could be reduce the MSF errors. The MatLab code of PSD analysis is listed in Appendix A.

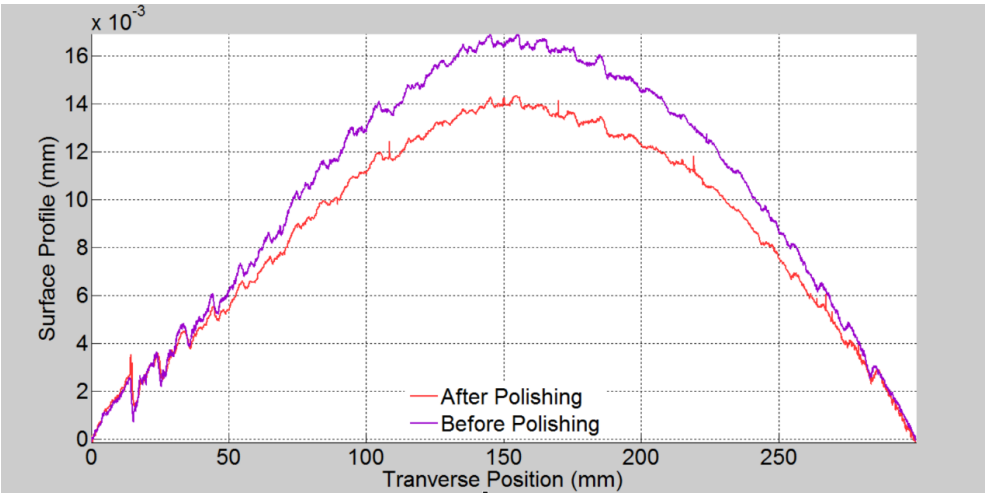

Figure 3.3: Surface profiles of the part before and after polishing.

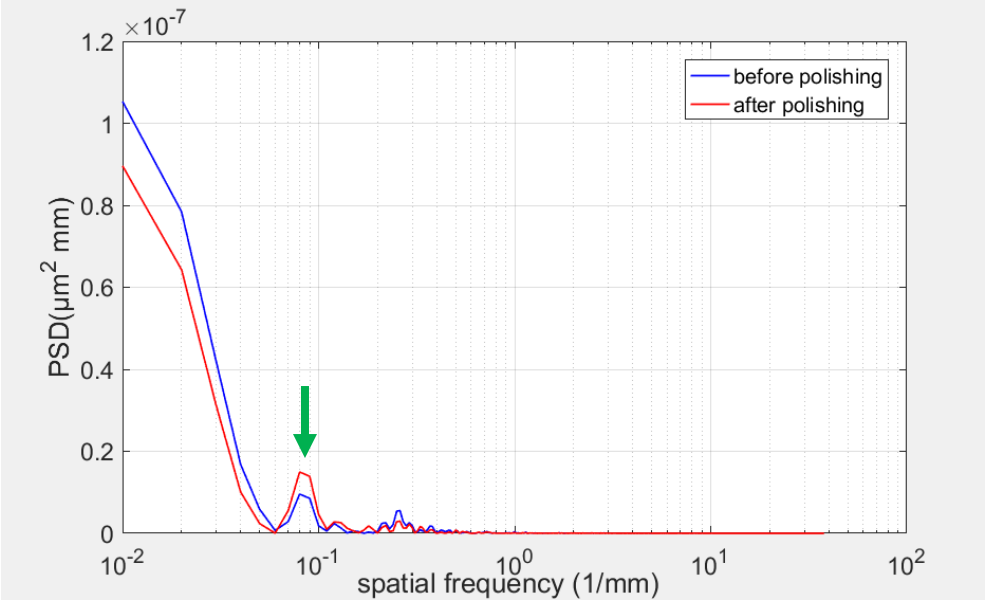

Figure 3.4: PSD analysis of the surface before (blue) and after (red) polishing.

3.2 Mid-spatial Frequency Control with Rigid Tools

It has been demonstrate that a flexible bonnet tool can hardly remove mid-spatial frequencies. In this section, a rigid tool was used trying to remove mid-spatial frequencies. This procedure was named ‘grolishing’ by Walker, because it is an intermediate procedure between ‘grinding’ and ‘polishing’.[118]

3.2.1 Introduction

Unlike the grolishing experiment conducted previously by Yu and Li[8, 9], a new tool interface has been designed and used in this experiment, which is shown in **Figure 3.5**. This design allowed the tool to float freely on the workpiece surface, which is less likely to introduce new mid-spatial errors to the surface.

A Fanuc robot arm was used in this experiment instead of using a brass-button tool in a polishing machine. This choice had a few advantages listed as below.

(i) It gives a potential possibility to control the mid-spatial frequency fully automatically in the future, which mitigates risk and reduces dependency on highly-skilled staff.[119-121]

(ii) It is easier to control the contamination using a separate equipment for polishing procedure and coarse grinding.

(iii) A robot arm has lower purchase and maintenance price compared with a CNC polishing machine.

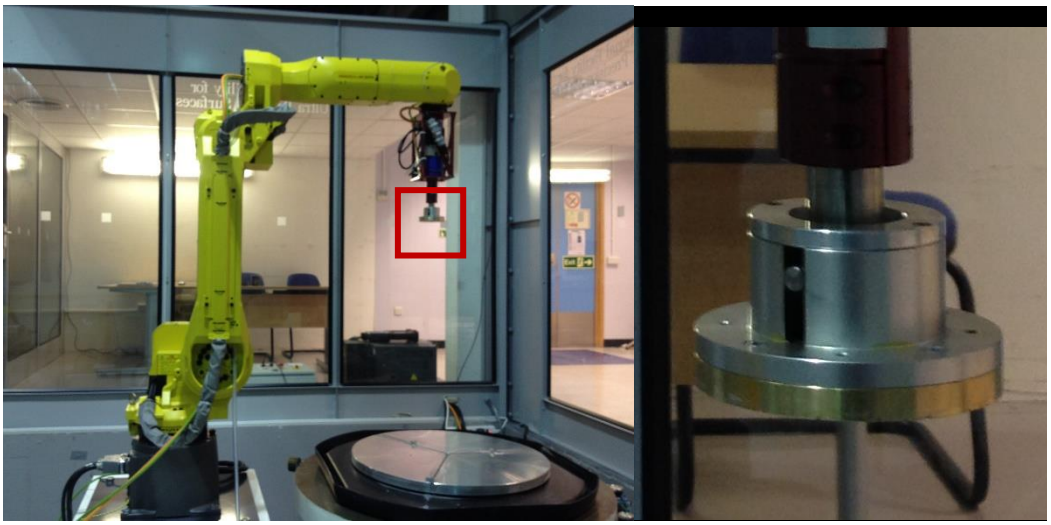

Figure 3.5: Fanuc robot (left) and the tool (right) used for grolishing experiment.

3.2.2 Grolishing Experiment procedures and result analysis

3.2.2.1 Experiment procedures

This experiment procedure was similar to the previous polishing experiment procedures. It was divided into four parts: 1. Firstly, mid-spatial frequencies were generated on the workpiece surface; 2. Then the workpiece surface was measured by Form Talysurf Profilometer; 3. 'Grolishing' experiment was conducted to remove the mid-spatial frequencies generated on the workpiece surface using a rigid floating tool with Fanuc robot; 4. At last, the surface profile of the part was measured again and compared with the result measured before grolishing.

In this experiment, the grolishing tool path was perpendicular to the MSF errors in order to separate the marks left on the workpiece surface in each procedures. The misfit between the rigid tool and workpiece could be reduced because of the working wear of the tool. The parameters of this grolishing experiment are shown in **Table 3.2**.

Table 3.2: Parameters for grolishing experiment.

Surface feed	Slurry	Spindle speed	Track space	Time
1500 mm/min	9 µm Al_2O_3	800 rpm	10 mm	15 min
Tool material	**Tool size**	**Tool weight**	**Part material**	**Part size**
Brass	100 mm	2 kg	Borosilicate	400 mm

3.2.2.2 Result analysis

This experiment is similar to the grolishing experiment conducted by Yu and Li[8, 9], using a bonnet tool attached with a brass button. Rather than using a Zeeko IRP machine, this experiment is conducted by using a Fanuc robot arm, which contributes to the application of automated processing.

The surface profile result shows that the mid-spatial frequencies pre-generated on the workpiece surface have been reduced after the grolishing experiment with a rigid floating brass tool. The surface profiles before and after grolishing indicate that this tool could effectively remove material and made the surface more symmetrical.

The surface form is changed to be more symmetric after the grolishing process, which may be caused by the run-in between the tool and workpiece surface.

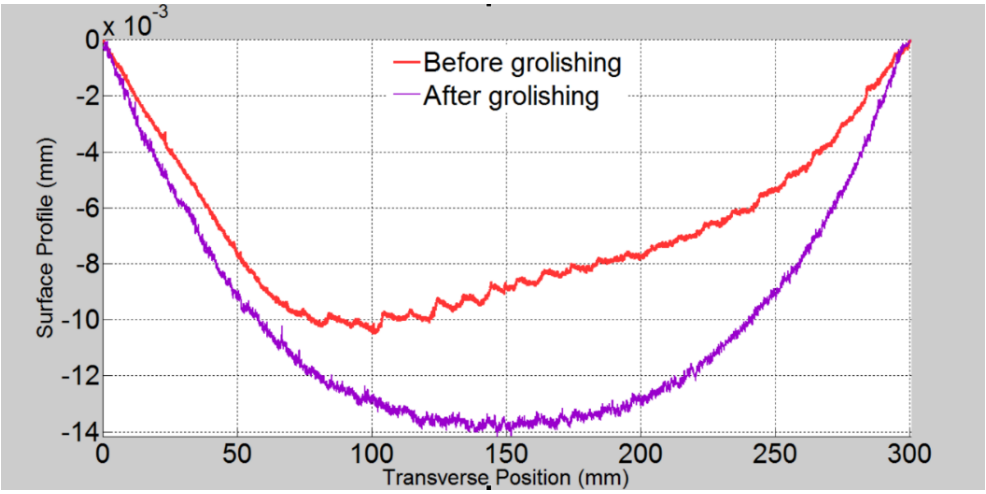

Figure 3.6: Surface profile measured before and after grolishing experiment.

The PSD analysis (shown in **Figure 3.7**) presents that the peak disappears at 10^{-1}/mm (reciprocal of the track spacing to generate MSF) after the grolishing experiment, which validates the conclusion that the rigid floating brass tool could reduce MSF errors.

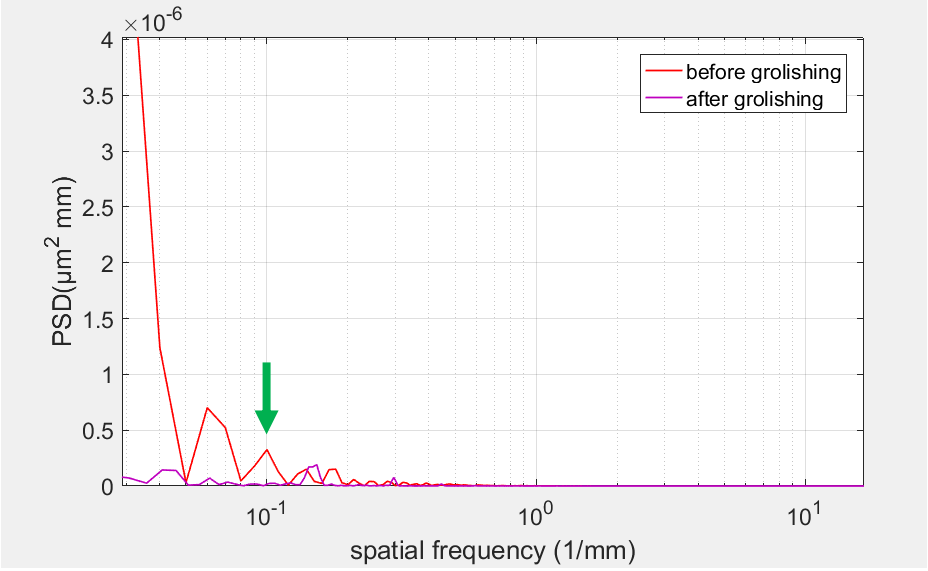

Figure 3.7: PSD analysis of the surface profile before and after grolishing.

However, considering the accuracy of this profilometer (125 nm in PV), mid-spatial frequencies with PV less than 125 nm can hardly be observed. It can be observed that

the surface profile after grolishing was rough. It could either be induced by the noise of measurement, a true reflection of the surface texture or MSF errors. Further metrology needs to be conducted using an interferometer with better metrology accuracy.

3.2.2 Validation metrology

In order to confirm whether the grolishing procedure could control the MSF errors down to PV less than 125 nm, a 4D interferometer was used to measure the workpiece surface before and after grolishing experiment.

The workpiece was pre-polished to a specular surface before each metrology test. The polishing raster tool path was orientated at a 45° angle to the grolishing tool path, so that the source of the mid-spatial frequency could be identified. A 4D interferometer with a 180 mm diameter beam expander was used in order to measure the flat surface. As introduced in Chapter 2, the accuracy of this interferometer is better than 10 nm, so that MSF error with PV above 10 nm could be detected by this equipment.

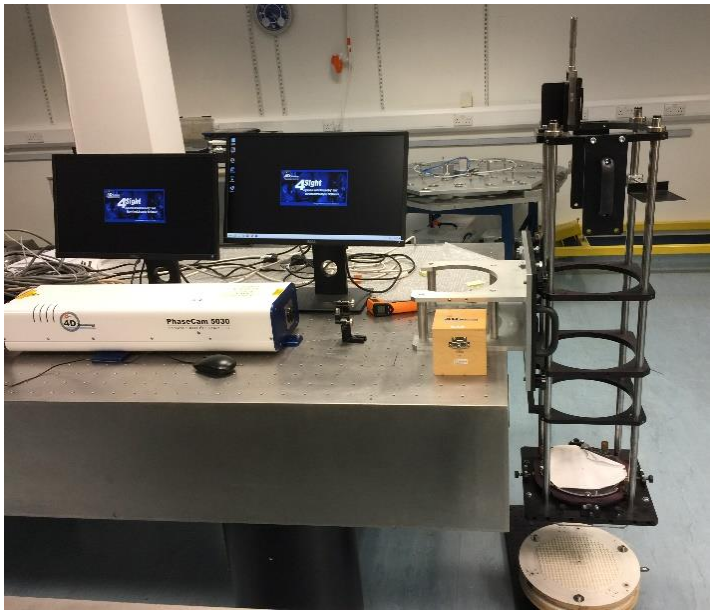

Figure 3.8: 4D interferometer with beam expander.

To remove the system error of the metrology, a reference flat sample was measured before measuring the workpiece to obtain a reference interferogram. The reference interferogram was subtracted from the workpiece interferogram to eliminate the system error. More details are recorded in **Appendix B**.

It is clearly shown in 错误!未找到引用源。 that, MSF errors have been removed by the grolishing procedure using a rigid tool, and this procedure do not introduce new MSF errors to the workpiece surface. This is because that the rigid tool could bridge over the peaks of MSF errors. The working wear of the tool also reduce the misfit between the tool and workpiece surfaces. Considering the metrology accuracy of the 4D interferometer, the PV of the MSF errors are controlled within 10 nm.

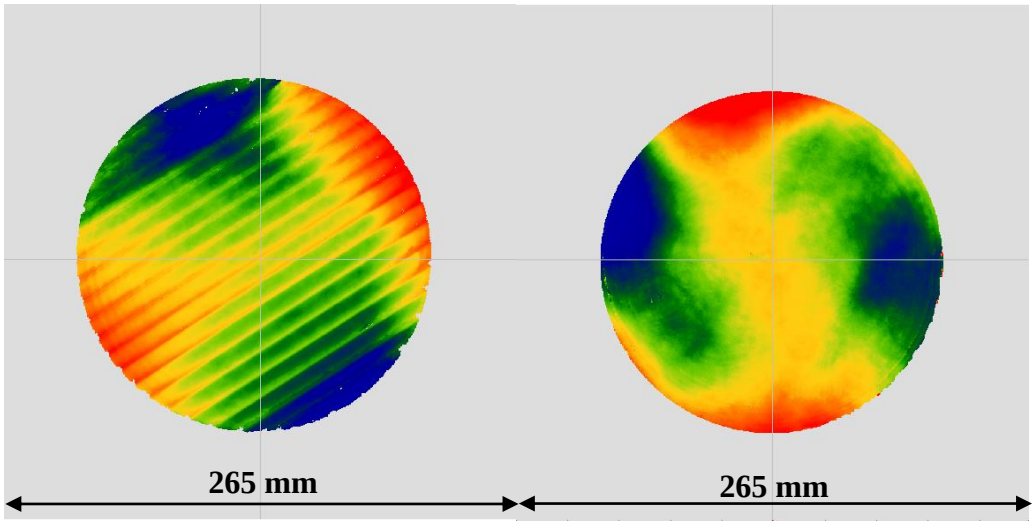

Figure 3.9: Interferogram measured by 4D interferometer before (left) and after (right) the grolishing experiment.

The PSD analysis of the surface profile before and after the grolishing processing are is shown in **Figure 3.10**. The peak value is significantly reduce at 10^{-1}/mm, which is the reciprocal of the track spacing to generate MSF errors. It demonstrates that this grolishing processing could effectively remove MSF errors on a flat surface.

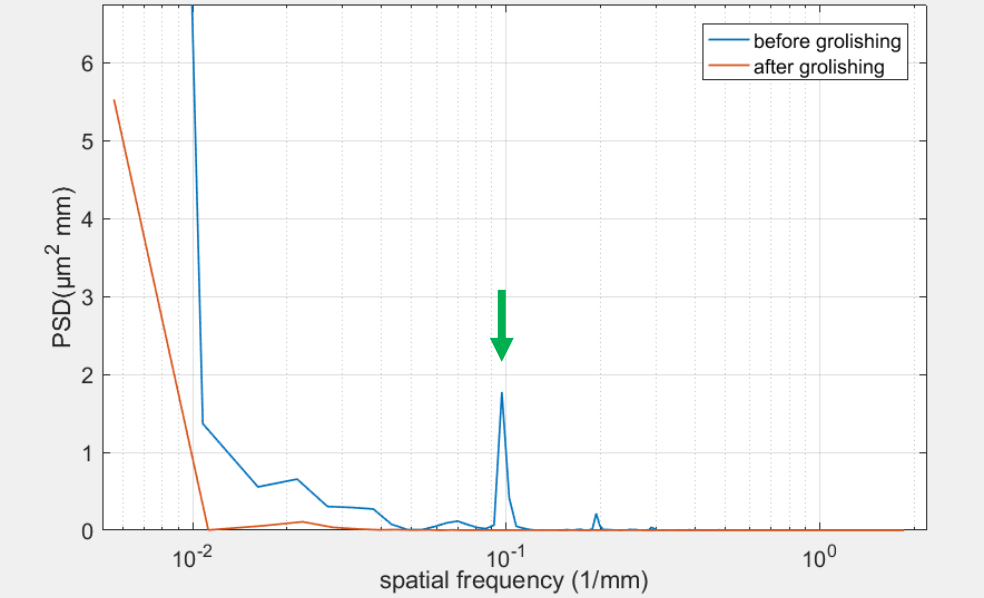

Figure 3.10: PSD analysis of the interferogram cross section before and after grolishing.

Similar methods can be used to control the MSF on spherical surfaces using a rigid tool with the same diameter of radius. However, the misfit cannot be avoided when working on an aspherical or free-form surface.

3.3 Comparison between Brass and Aluminium Tools

3.3.1 Aim

It has been demonstrate that a rigid floating tool can effectively remove MSF from a glass sample surface. This section aims to compare the performance of these two grolishing tools regarding material removal rate and surface texture.

3.3.2 Experiment Procedures

In this experiment, brass and aluminium alloy tools were used to grolish a hexagonal borosilicate glass, 400mm in diameter, with different aluminium oxide abrasives of C9,

C15 and C20 (with the size of 9µm, 15µm and 20µm respectively). Both of the tools were grooved so that it is easier for the slurry to flow into the centre of the tool surface during the processing. Both tools had the same size of 100 mm in diameter. Material removal rate and surface texture of these grolishing experiments were compared and analysed.

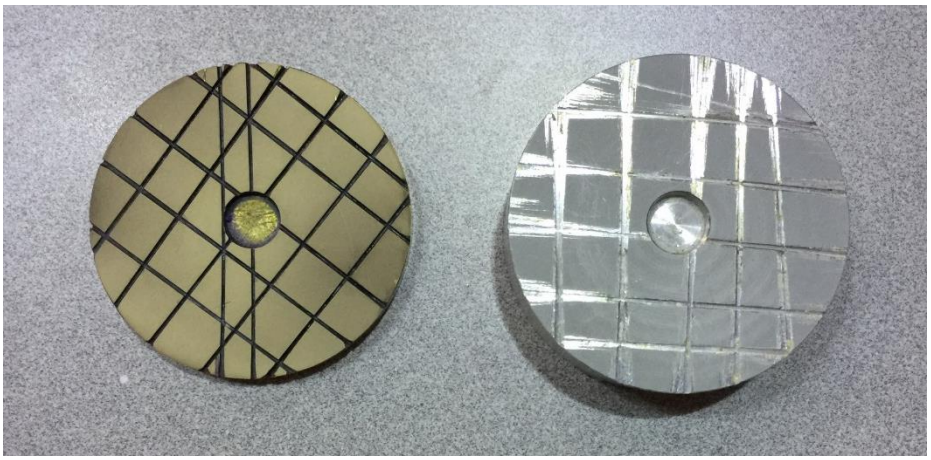

Figure 3.11: The Brass and Aluminium button (both 100 mm in diameter) used in the experiment.

The procedures of the experiment are briefly introduced as below:

(i) The part surface was pre-smooth using C9 for 30 min to ensure the same starting condition. The surface profile of the part was the measured by the Form Talysurf Profilometer.

(ii) These grolishing experiments were conducted using the Fanuc M-i20A robot. The edge of the part was not grolished, in order to leave an absolute reference datum for the metrology. The blue zone shown in **Figure 3.12** was left as unprocessed.

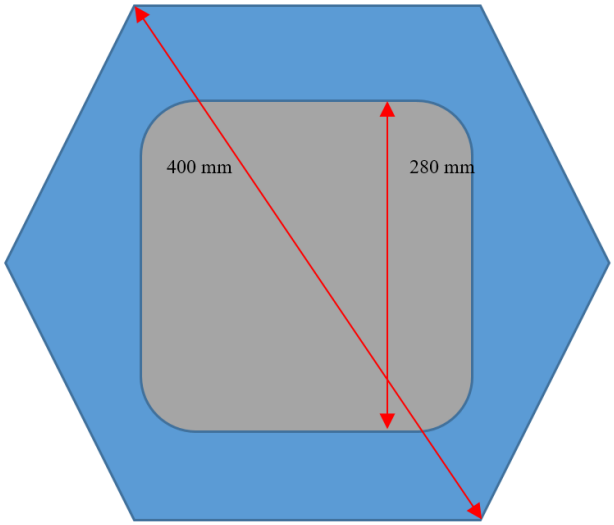

Figure 3.12: Schematic diagram of the grolished area on the part.

The parameters used in these grolishing experiments are listed in **Table 3.3**.

Table 3.3: Parameters for grolishing experiments.

Surface feed	Spindle speed	Track space	Time	Tool weight	Tool size
800 mm/min	1500 rpm	10 mm	1 hour	2 kg	100 mm

(iii) The surface profile of the part was measured again by the profilometer. The material removed in the grolishing experiment was calculated by subtracting the two profiles before and after these experiments.

(iv) The surface texture of the part after each grolishing experiment was tested by a white light interferometer, introduced in Chapter 2. The procedure is shown in 错误!未找到引用源。.

3.3.3 Result and analysis

The results of the material removal rate are listed in **Table 3.4**, from which we can see that larger abrasive size gives higher material removal rate, as expected. Although the same parameter were used in these experiments, using a brass tool could improve the removal rate compared with the aluminium tool. The reason was believed to be the different material removal mechanism during the grolishing procedure.

Table 3.4: Material removal rate.

	C9	C15	C20
AL	4.8 mm^3/min	14.2 mm^3/min	36 mm^3/min
BRASS	45.6 mm^3/min	46.8 mm^3/min	57 mm^3/min

Grolishing is similar to the conventional lapping process. There are two material removal mechanisms for the lapping process with loose abrasive and carrier fluid. In this experiment, the abrasive is aluminium oxide and the carrier fluid is water. The rolling abrasive could removal material from the workpiece more effectively than the sliding abrasive, while sliding could create better surface texture than rolling.[122]

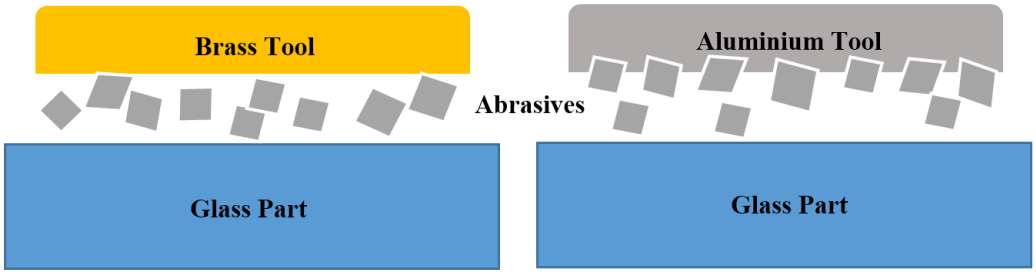

Figure 3.13： Schematic diagram of rolling (left) and sliding (right) mechanism in grolishing.

The hardness of the aluminium (2-2.9 in Mohs scale) is less than brass (3-4 in Mohs scale), and aluminium oxide abrasive has a hardness of 9 in Mohs scale.[123] Thus, it is easier for the abrasive to embed into the soft aluminium tool and slides on the workpiece

surface. On the other hand, the abrasive prefers to roll between the brass tool and the workpiece during the grolishing experiment.

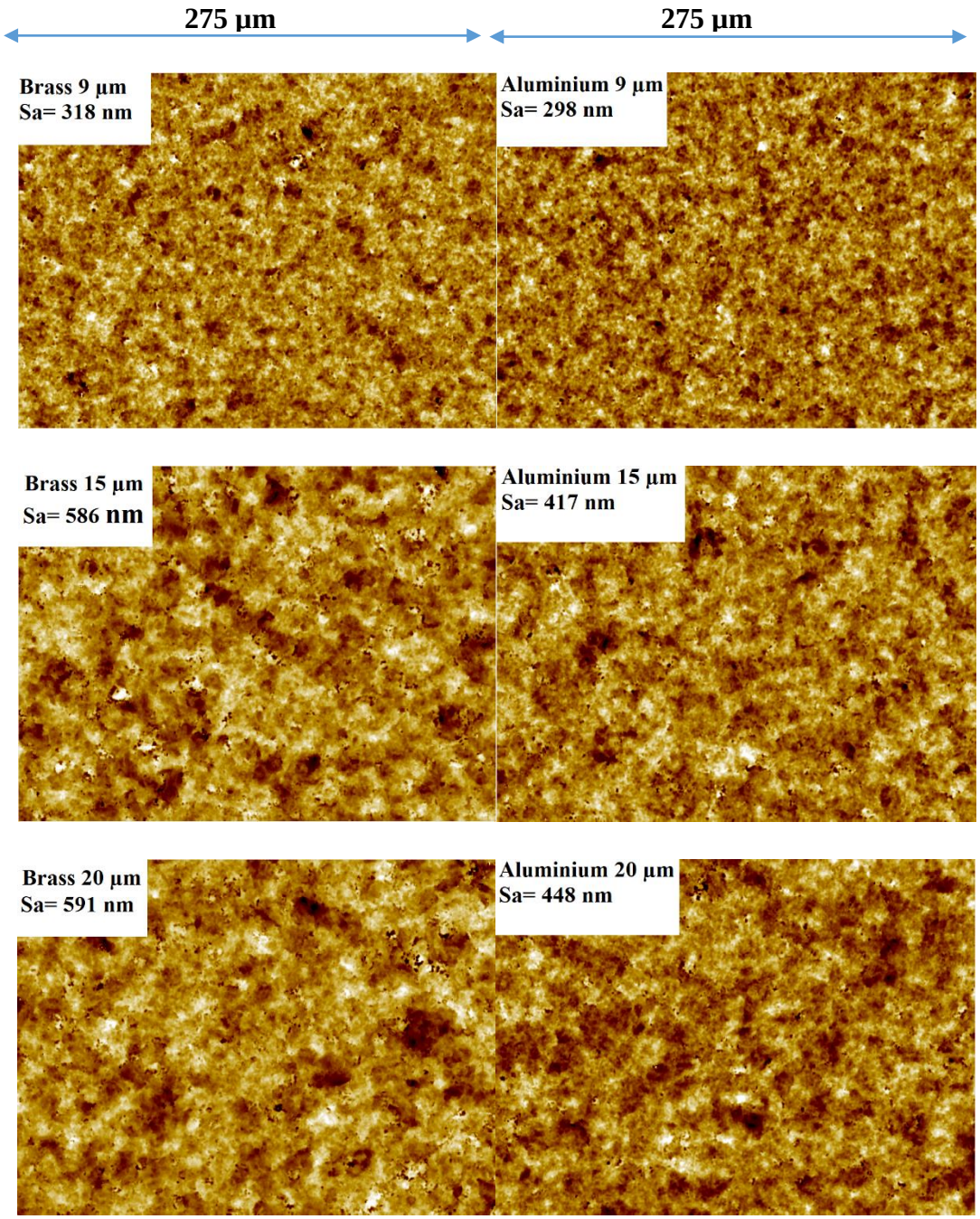

Figure 3.14: Surface texture of the workpiece surface after grolishing by brass and aluminium tools with different abrasive of 9µm, 15µm and 20µm (shown with the same scale).

Table 3.5: Surface average of the workpiece surfaces after grolishing.

	C9	C15	C20
Aluminium	298 nm	417 nm	448 nm
Brass	318 nm	586 nm	591 nm

The surface average was measured for it could represent the overall roughness on the surface. The results are shown in **Figure 3.14** and

Table 3.5. The surface quality deteriorates with the increase of the abrasive size. For the same abrasive, the aluminium tool leaves a better surface texture than the brass tool. The reason has been discussed that rolling mechanism dominates processing when using the brass tool. It removes material more effectively but makes more damage to the surface. Brass and aluminium tools are complementary, and both have its own advantage for grolishing and should be selected according to the process step considered.

3.4 Conclusion

In this chapter, polishing experiments are reported to demonstrate the common perception that it is difficult to remove MSF errors using a compliant tool. This leads to the utility of a rigid tool to control MSF errors, as also reported in this chapter.

MSF errors are successfully removed by a rigid floating tool. Metrology has been conducted to prove that the PV of mid-spatial frequency can be controlled down to 10nm according to the measuring accuracy of the interferometer. To find out the optimised material for the grolishing tool, brass and aluminium tools are compared regarding to the material removal rate and surface texture. The results indicate that

using the brass tool can improve the material removal rate, while the aluminium tool can give a better surface finish. Two material removal mechanisms have been introduced to explain the experiment results.

Although it has been shown that a rigid floating tool can effectively reduce the mid-spatial frequency from a flat (or possibly a spherical) surface, it is always a critical issue to control MSF errors on an aspherical or free-form surface. More research needs to be conducted to resolve this problem.

Chapter 4. Mid-Spatial Frequency Control Using Bound-Diamond Pads

4.1 Introduction

The previous chapter has demonstrated that the grolishing procedure using rigid metal tools and loose abrasive could successfully remove MSF errors on flat surfaces. However, due to the limitation of tool flexibility, it is impossible to eliminate the misfit during manufacturing for the workpiece with aspheric surfaces.

In this chapter, bound-diamond pads with variable flexibility are introduced to control the MSF errors. In the bound diamond pads, the abrasive (diamond particles) are embedded into the resin layer attached to the surface of the pad. Unlike loose abrasives, these diamond particles are not free to move. During the processing, sliding mechanism dominates the procedure, so that the results showed better surface texture than using the same size aluminium oxide abrasives.

Material removal rates were measured using bound-diamond pads with different diamond size. The flexible diamond pad showed better performance for removing material, especially for the aggressive 250 micron diamond pad, of which the volumetric material removal rate was more than 200 times faster than a polishing procedure using bonnet tools.

MSF errors were successfully controlled using a 3 micron diamond pad with track spacing of tool path less than 2 mm. However, this tool had problem to process

aspherical surfaces due to the non-uniform pressure distribution caused by the misfit between tool and workpieces surfaces.

A glazing effect was discovered in the grolishing experiment with diamond pad finer than 9 microns. This phenomenon is introduced, and its potential impact is discussed in this chapter.

4.2 Grolishing Experiments Using Rigid Diamond Pads

KGS Speedline® diamond pads[124] were used in the grolishing experiments trying to control mid-spatial frequency on a pre-smoothed borosilicate glass. It was suggested by the KGS sales department that this pad series with rigid resin could effectively remove material from a ceramic part.

The grolishing experiment procedure is briefly introduced, and the surface profile of the part was measured before and after the experiment.

4.2.1 The first trial of grolishing using rigid KGS pads

The aim of the first trial using this rigid KGS pad is to test the removal ability of the tool and whether this tool will introduce new MSF errors on the workpiece surface.

4.2.1.1 Preparation

The borosilicate part used in this experiment was pre-smoothed by hand using C9 Aluminium oxide abrasive for 1 hour to remove potential MSF errors left on the part surface. The surface profile was then measured by a profilometer.

The diamond pad was glued on a brass metal pad using Loctite Adhesive, which is shown in **Figure 4.1**. During the bonding process, the pad was pressed against a flat

surface until the glue solidified. Diamond particles are bound with resin in this pad. The size of the diamond particle for this KGS Speedline® series ranges from 50-3000 (3 to 250 μm). In the first grolishing experiment, a pad containing 20μm diamond particles was used. This pad was conditioned by hand on a flat glass workpiece before the experiment. (Another conditioning method is also introduced in **Section 4.2.2**.)

Figure 4.1: A KGS diamond pad attached to a metal pad used for grolishing experiment.

4.2.1.2 Grolishing

This experiment followed the previous grolishing procedures. Only the central zone of the part was grolished, which left a reference area for metrology, which is shown in **Figure 4.2**. A Fanuc robot was used to conduct this experiment, using the parameters shown in **Table 4.1.**

Loose abrasives (such as aluminium oxide or cerium oxide) were not used in this experiment, as the diamonds are bound within the resin of the pads. Water was used as coolant.

Table 4.1: Parameters for Grolishing experiment with a rigid KGS pad.

Tool Diameter	Head Speed	Surface Feed	Time	Tool Weight	Track Spacing	Diamond size
100 mm	500 rpm	1500mm/min	30 min	3 kg	10 mm	20 μm

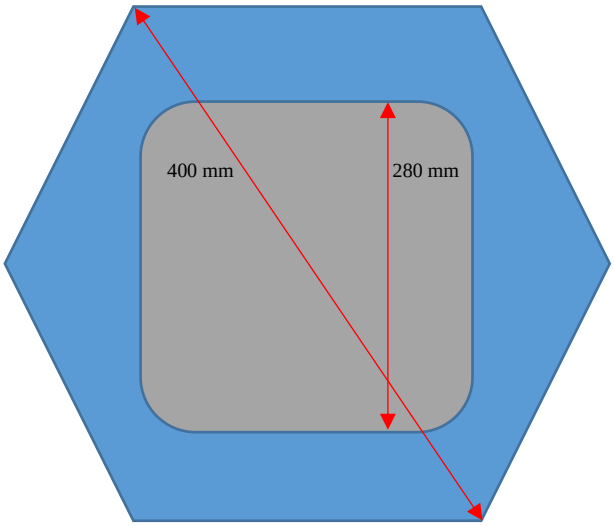

Figure 4.2: Schematic diagram of the grolished area on the part.

4.2.1.3 Metrology result and analysis

The surface profile was measured before and after the grolishing experiments at the same position on the part. A total of 3 experiments were conducted. It can be indicated from one of the experimental results shown in **Figure 4.3** (the other 2 repeated experimental results are recorded in **Appendix C**) that the material removal for this grolishing experiment was not uniformly distributed and MSF content can be found in some positions. This may have been induced by the misfit between the tool and workpiece surface. Unlike the grolishing tool with a metal button, this rigid pad made of hard resin does not wear easily during the conditioning and working procedure. Therefore, it is more difficult to adapt to the workpiece surface profile. Micro scale misfit can lead to non-uniform pressure distribution and affect the uniformity of the

overall material removal. It may need more time or a new method for conditioning the tool before the grolishing experiment, to reduce the misfit and achieve intimate contact between tool and part.

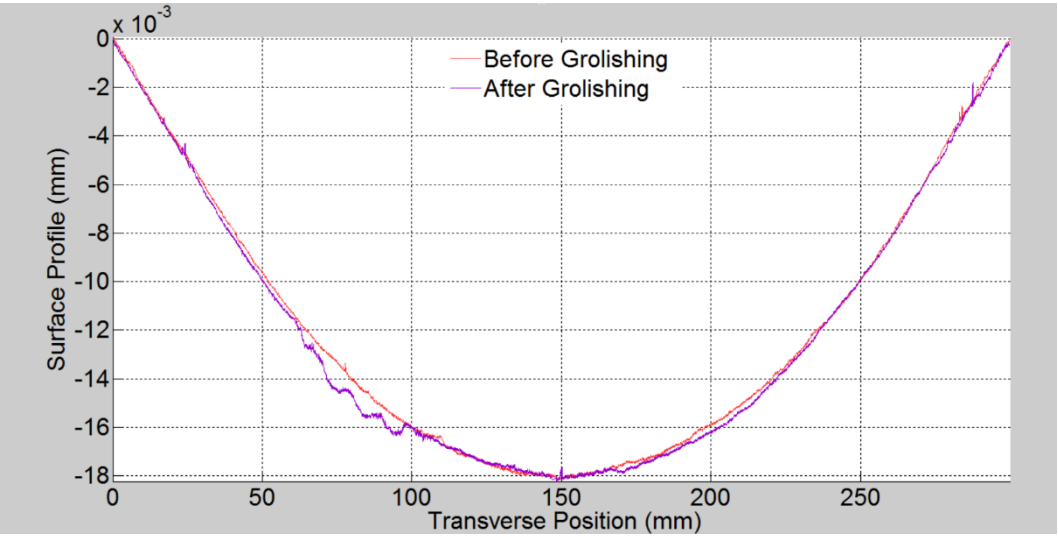

Figure 4.3: Surface profile of the part before (red) and after (purple) the grolishing experiment.

4.2.2 Conditioning KGS pads by a grinding wheel

To reduce the mismatch between the pad and working surface, these pads need to be properly conditioned before use. According to previous experience in the research team, a rigid tool needs to be ground to fit the workpiece surface. In this experiment, a KGS pad was conditioned by a grinding wheel using the IRP 600 before the grolishing experiment.

4.2.2.1 Experiment procedures

Although a nominal flat part was used in the grolishing experiment, it still had a small spherical error. The part surface profile was measured by a Form Talysurf Profilometer, and its best-fit spherical radius was calculated. The result indicated that the workpiece surface had a convex surface of 200 m radius.

Figure 4.4: The process for conditioning KGS pad in IRP 600.

This conditioning procedure was similar to polishing a workpiece with spherical surface. The difference was that in this procedure the KGS diamond tool was not polished but ground.

A concave surface of 200 m was designed, and the corresponding tool path was generated in the Zeeko Tool Path Generator (TPG) software. During the conditioning process, the grinding wheel remained stationary on the C axis, and the pad is rotated at 100rpm on the H axis. As the tool moved along the X axis of the polishing machine repeatedly, the surface of the pad will gradually approach the designed surface. At the end of this conditioning procedure, the IRP 600 machine was thoroughly cleaned to avoid the cross contamination.

The pad surface was conditioned by hand and the grinding wheel is shown in **Figure 4.5**, from which it was indicated that more material is removed according to the colour change. As the designed tool path followed the same profile based on the workpiece surface, the misfit between tool the workpiece was reduced.

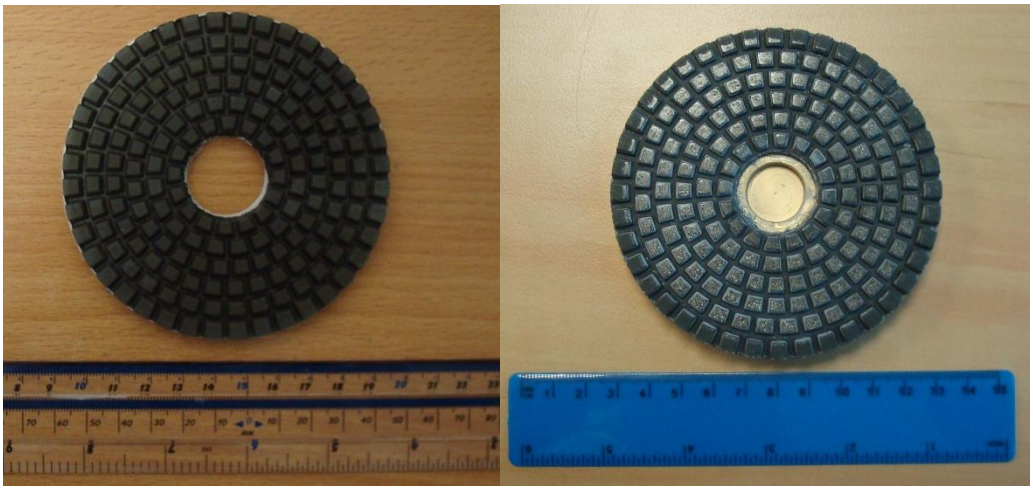

Figure 4.5: The surface of the KGS pad after conditioning by hand (left) and a grinding wheel (right).

The diamonds were in the bulk of the pad, the new diamonds were exposed after removing the resin near the surface in the conditioning process.

The same grolishing experiment was repeated for 3 times using the KGS pad conditioned by this procedure. The surface profiles of the part before and after the grolishing process were measured. Then the part surface was polished at 45° to the grolishing orientation and measured by an interferometer with beam expander to look for MSF errors.

4.2.2.2 Results and analysis

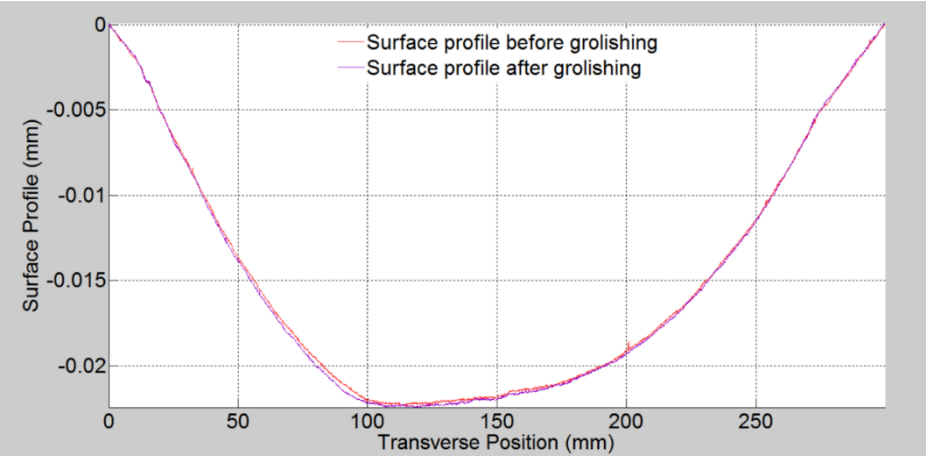

Figure 4.6: Surface profiles before and after the grolishing experiment.

One of the results are shown in **Figure 4.6**, the other two measuring results are recorded in **Appendix C**. Unlike the surface profiles shown previously after a grolishing experiment using the pad conditioned by hand, the removal appeared to be more uniform, and no mid-spatial frequencies could be observed after the conditioning process using a grinding wheel. This indicated that the mismatch between KGS pad and glass surface had been reduced.

Unfortunately, MSF content was found in the interferogram clearly. The distance between the adjacent peaks of these mid-spatial frequency foot waves was 10 mm, which was the same as the track spacing of the raster tool path.

PSD analysis was also conducted using MatLab, the peak could be observed clearly at the frequency of 10^{-1}/mm, which is the reciprocal of the raster tool path. The analysis results validated the conclusion that this KGS Speedline pad would introduce MSF errors to the part surface.

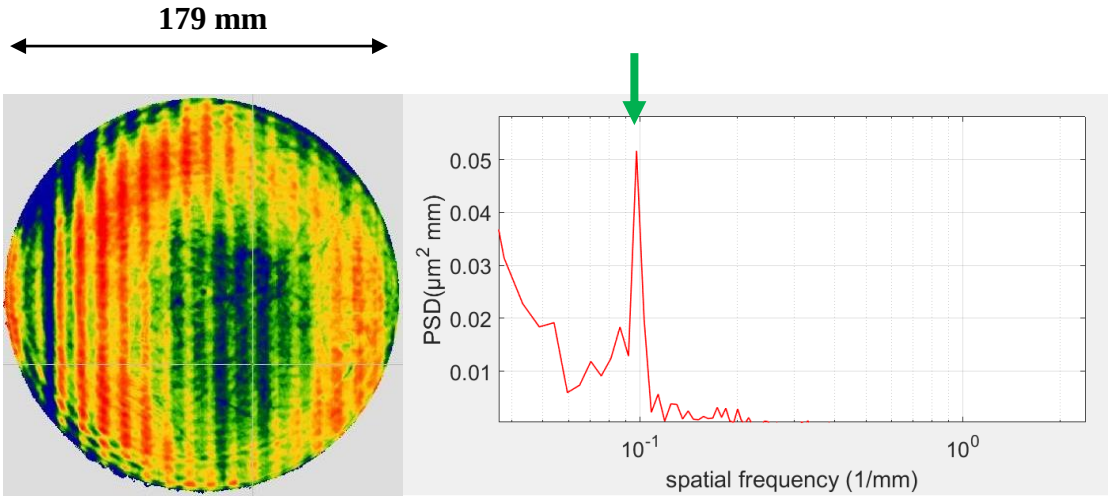

Figure 4.7: Interferogram of the workpiece surface after grolishing and polishing (left) and PSD analysis of the interferogram (right).

Another issue was that the removal rate (0.2 mm^3/min) was much lower than the grolishing using loose abrasive (4.8-57 mm^3/min), which increases the overall processing time.

This problem has been discussed with Anthony Beaucamp, a co-researcher, who had experience using KGS diamond pads. He suggested that a more flexible diamond pad with smaller pellet size should be used for the grolishing experiment.

4.3 Grolishing Experiments Using Flexible Diamond Pads

This work draws on the development of the Shape Adaptive Grinding (SAG) process by Beaucamp et.al.[124-126], but deployed on a robot rather than a polishing machine. These pads were mounted via a compliant layer on rigid metal buttons to give ability to adapt to an aspheric profile.[120] The aim of this experiment was more effectively to control MSF errors with higher material removal rate and better surface finishing.

4.3.1 Material removal rate

Firstly, grolishing experiment using flexible diamond pads were conducted to measure the material removal rate. 250 micron and 20 micron diamond pads were used with a more massive tool, in order to achieve the working condition of the diamond pads and also increase the removal rate.

4.3.1.1 Experiment procedures

The removal experiments were conducted by a robot working on a borosilicate glass workpiece. The workpiece was pre-smooth on a conventional single axis machine by C9 aluminium oxide to remove potential MSF errors left by previous processing.

Surface profile of the part was measured before and after the experiments by a Talysurf profilometer. A white light interferometer was used to measure the surface texture of the part after each grolishing run.

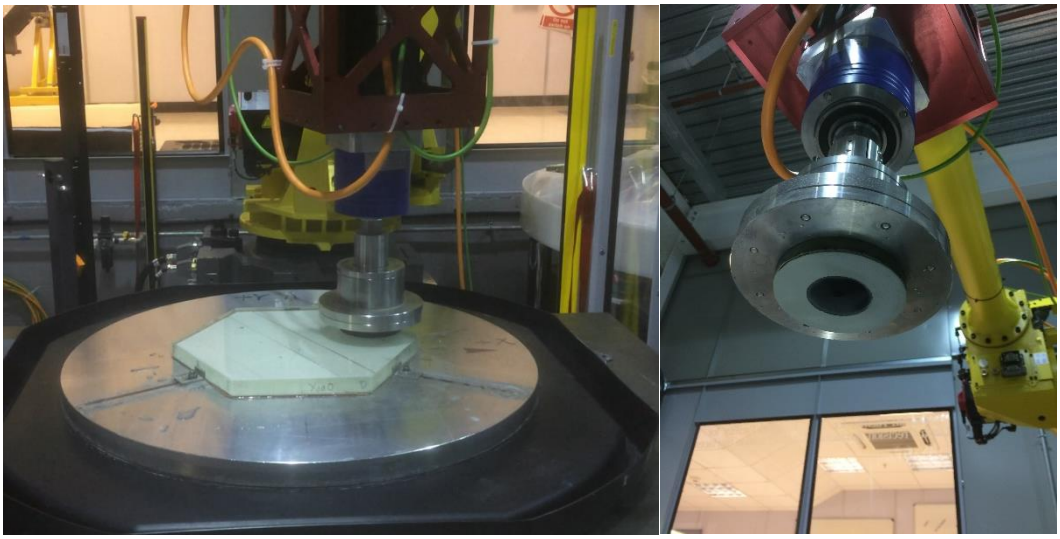

Figure 4.8: Removal experiment using flexible KGS diamond pads.

4.3.1.1 Results and analysis

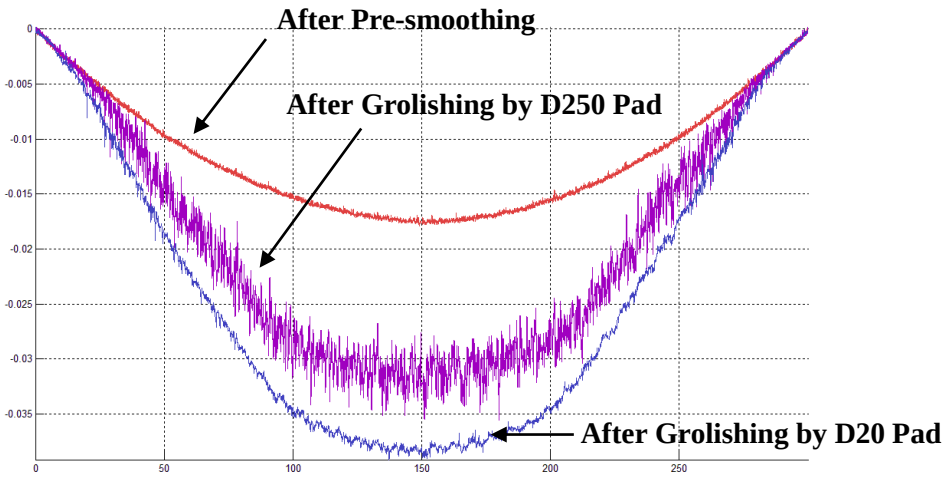

Figure 4.9: Surface profiles before (red) and after grolishing with 250 micron (purple) and 20 micron (blue) diamond pads.

The surface profiles are shown in **Figure 4.9**, from which the overall material removal was calculated. The metrology noise was significantly higher after grolishing with extremely aggressive 250 micron diamond pad (D3) compared with the benign 20 micron pad (D20). The flexible pads were easier to adapt to the workpiece surface, and the material removal was much more uniform compared with the rigid diamond pads.

It is shown in **Table 4.2** and **Figure 4.10** that the volumetric material removal rate was increased using this bound-diamond pads compared with the rigid diamond pads. Especially for the aggressive 250 micron diamond pad, the removal rate was more than 200 times higher than the conventional polishing procedure (about 1 mm^3/min[127]). The part grolished by 20 micron diamond pad had a better surface texture (392 nm) than the part grolished by 20 micron Al_2O_3 loose abrasive using a brass tool (591 nm).

Table 4.2: Results using flexible KGS bound-diamond pads.

Abrasive	250 µm diamond pad	20 µm diamond pad
Vol. Removal Rate	267 mm^3/min	45 mm^3/min
Texture (nm)	1150 mm^3/min	392 mm^3/min

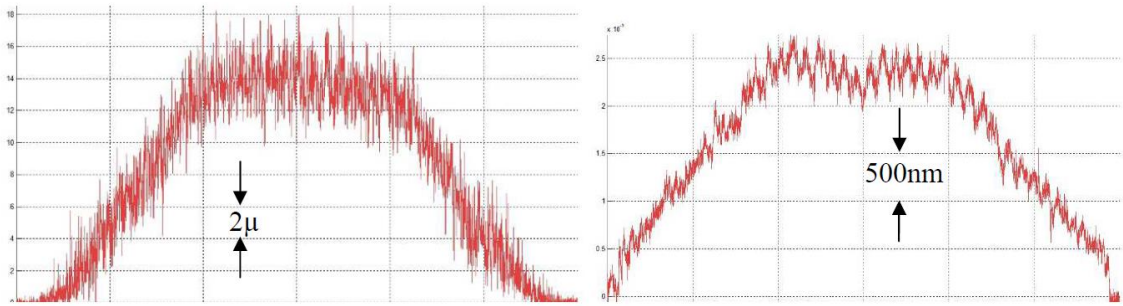

Figure 4.10: Removal profiles with 250 micron diamond pad (left) and 20 micron (right) 200rpm spindle speed, applied force 8.2KgF, time 2m 30s.

4.3.2 Observation for MSF using flexible diamond pads

A 3 micron diamond pad (D3) was used to grolish a part smooth by C9 aluminium oxide using an epicyclic tool path. The part was measured by an interferometer after every 20 min of processing. The **Figure 4.11** shows the interferogram of the workpiece surface as it evolved.

It is generally believed that conventional lapping or smooth procedures cannot make a surface directly measureable by a visible interferometer. In order to achieve an interferogram, the surface needs to be pre-polished before the metrology. However, the results demonstrate that the surface can be measured by an interferometer directly after the grolishing process, which potentially improves the overall production efficiency. This may be related to the glazing effect, which is discussed later in **Section 4.4**.

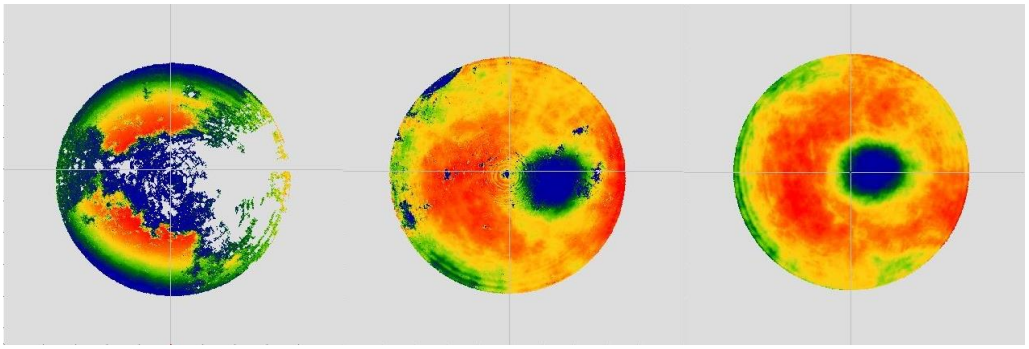

Figure 4.11: Interferogram measured after grolishing with 3 micron diamond pad for 20 min, 40-min and 60 min using a raster tool path with 10 mm track spacing.

MSF error is very sensitive to the track spacing of the raster tool path. Two grolishing experiments were conducted on a flat part using different track spacing (10 mm and 2-mm) of the tool path. Then the part was measured by the interferometer with a beam expander. Results in **Figure 4.12** shows that MSF errors was not introduced to the part surface process by the 2 mm track spacing grolishing process, while on the contrary, MSF errors could be observed on the part surface grolished with tool track spacing of 10 mm.

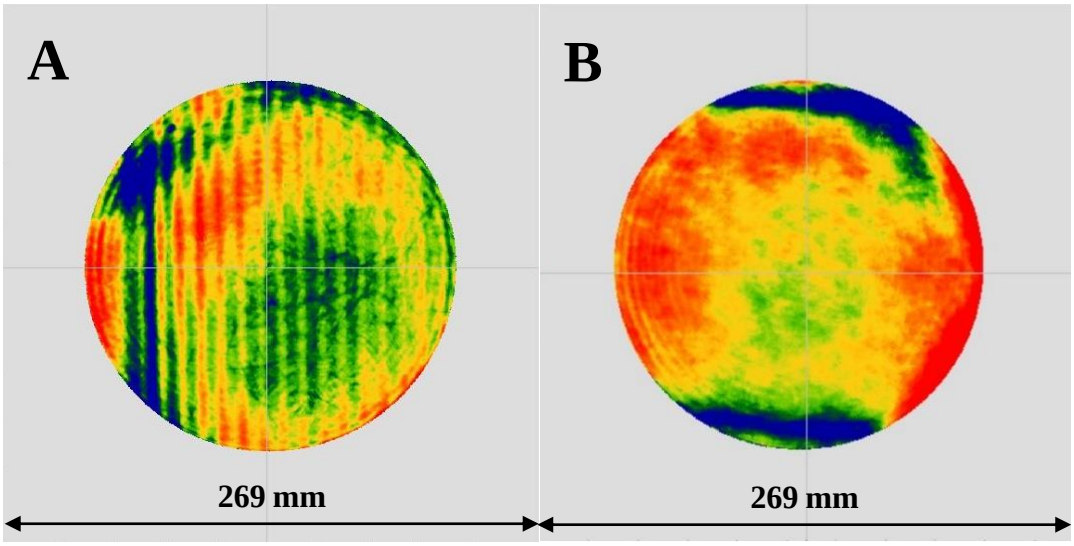

Figure 4.12: Comparison of the MSF errors introduced by grolishing using raster tool path with different track spacing of 10 mm (A) and 2 mm (B).

The conclusion above is also validated by the PSD analysis, from which it indicates that the peak is reduced at 10^{-1}/mm using 2 mm track spacing in grolishing experiment.

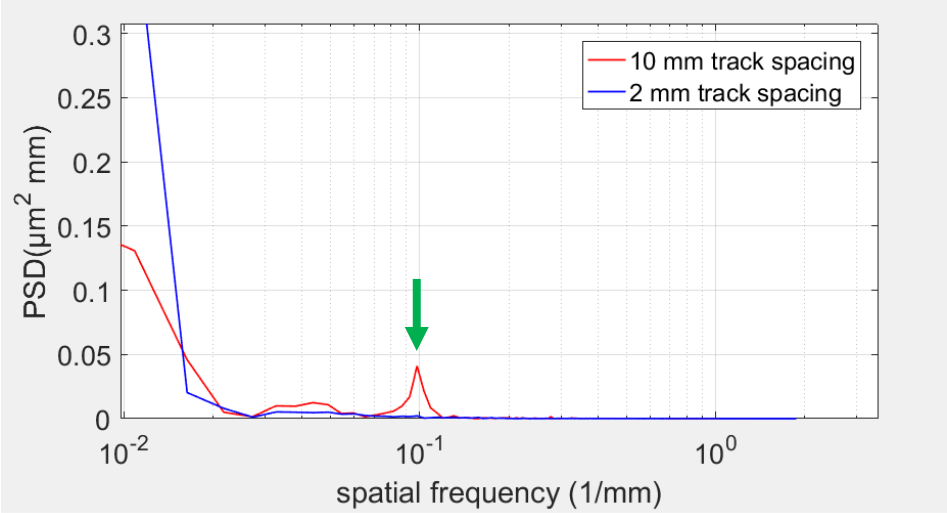

Figure 4.13: PSD analysis of the workpiece surface after grolishing with different tool track spacing of 10 mm and 2 mm.

4.3.3 Grolishing on an aspherical surface using a diamond pad with flexible foam layer

An experiment was conducted using the tool with flexible diamond pad on an aspherical borosilicate part. The flexible layer surface was changed to a best-fit spherical surface to the part in order to reduce the misfit. The tool path was generated by Zeeko TPG for this aspherical surface.

During the experiment, the tool surface could deform to adapt to the workpiece surface to reduce the misfit gap. But the pressure between the tool and workpiece surface could not be distributed uniformly, and this almost caused serious damage to the workpiece surface, especially the edge surface, during the grolishing procedure.

To solve this problem, the thickness of the flexible layer was increased to reduce the pressure distribution difference over the tool's surface. Then, the same experiment was conducted again on the same aspherical surface. Results are shown in **Figure 4.14**.

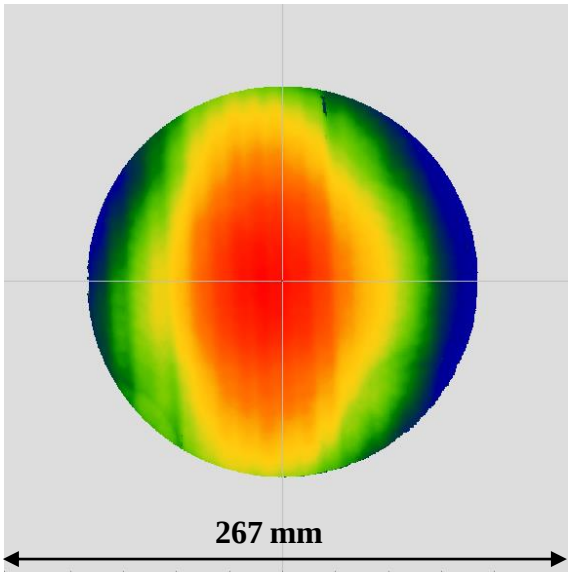

Figure 4.14: Interferogram of the surface after grolishing by diamond pad with flexible layer.

The MSF errors are also shown in the PSD at the frequency of 10^{-1}/mm, which indicates that the using this KGS tool with a flexible layer does not solve the misfit problem.

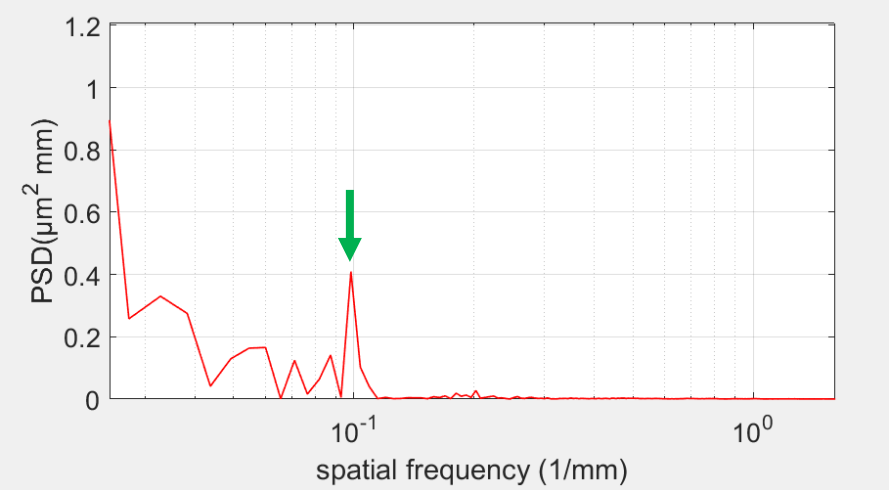

Figure 4.15: PSD analysis of the surface after grolishing by diamond pad with flexible layer.

4.4 Glazing Effect

The glazing effect was discovered through the material removal rate reducing for some KGS diamond pads over processing time. This occurred for grolishing using a diamond pad with grit size smaller than 9 microns. **Figure 4.16** shows the surface profiles of the part measured after successive grolishing runs on the same part suing the same diamond pad.

This phenomenon was also discovered by Johnson and introduced in his PhD thesis.[128] It was explained in this thesis that this effect occurs when the material on the pad surface could not be worn away sufficiently fast. In other words, the abrasive pad surface could not refresh rapidly enough to expose new effective diamond crystals.

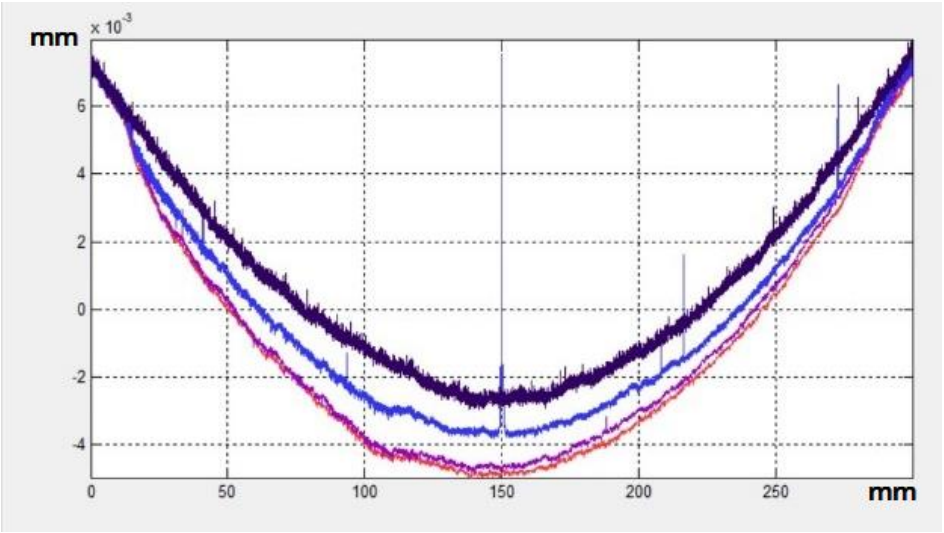

Figure 4.16: Surface profiles of the part surface measured before and after three grolishing experiments using a D9 diamond pad.

It has been concluded by Johnson that glazing is not desirable in the optical processing because it ultimately stops material removal.[128] However, glazing could also improve the surface texture. Previous experiments introduced this thesis have proved that a D3 diamond pad could produce a surface measurable for the interferometer, which reduce the overall fabrication time. According to Johnson's experiment results, a glazed process does not introduce any sub-surface damage and surface errors, it may be used at the end of a process to improve the surface finishing.

4.5 Conclusion

Overall, the MSF errors could be effectively controlled by using flexible diamond pads. The volumetric material removal rate could be raised up to 267 mm^3/min using a 250 micron diamond pad of diameter 100 mm. The surface texture is improved to be measurable by an interferometer directly after the grolishing process using a 3 micron diamond pad.

Experiments were conducted trying to apply this technique to aspherical surfaces for MSF control. However, this tool failed to work on the aspherical surface due to inadequate compliance.

Glazing effect was discovered in the grolishing experiment, and its initiation was introduced. The author also introduces the opinion of Johnson and discusses his conclusion. Rather than completely denying the usefulness of this phenomenon, a potential application of the glazing effect in surface processing is introduced in this chapter.

This page is left blank intentionally

Chapter 5. Characterization of a non-Newtonian Materials and Simulation for Influence Functions

5.1 Introduction

The previous chapters of this thesis have introduced the grolishing method with rigid tool interfaces to remove mid-spatial frequencies errors on flat surfaces. However, as has been discussed in Chapter 2, there are compelling market demands to make asphere and free-form surfaces optics to reduce the lens or mirrors numbers in an optical system. However, unlike processing spherical surfaces, it is never possible for a rigid tool to conform to an aspherical or free-form surface. The misfit between the tool and workpiece surface can lead to serious periodic surface errors and affect the performance for functional surfaces.

It has been introduced in Chapter 3 and Chapter 4 that the tool needs to be conditioned even before using on flat surfaces. Otherwise, the misfit down to microscale can affect the quality of a functional surface. The misfit between a rigid tool and an aspherical or free-form surface can be millimetres. Thus, in practice, compliant tools are select for processing these surfaces, including inflated bonnets, stressed lap, magnetorheological fluid and so on. But these tools are limited to their smoothing ability to remove the MSF errors.

Although a grolishing tool with conformal layer and flexible diamond pads had been introduced to work on an aspherical surface, the result was not satisfactory due to the non-uniform pressure distribution.

In this chapter, a non-Newtonian material, Silly Putty TM[129], is introduced for the surface processing aspherical and free-form parts. This material can maintain a solid form at room temperature. The Young's Modulus of this material varies depending on the frequency of external forces, which gives a semi-flexible layer for the tool interface.

In order to guide the application of this non-Newtonian tool for the practical surface processing, simulation experiments were conducted looking for the relationship between the tool influence functions and tool spindle speed on flat surfaces. Practical tool influence function experiments were conducted to validate (or otherwise) the modelling results. A characterization experiment was also conducted to measure the Young's Modulus of this non-Newtonian Material, which provided essential data for the numerical simulation.

5.2 Material Characterization of non-Newtonian materials

5.2.1 Stress-Strain Curve

In order to determine the Young's Modulus of a material, the stress-strain curve of this material needs to be measured. It is usually conducted by stretching or compressing the materials with a constant speed. With the progress of the deformation, more force needs to be applied to the material to keep it extending or compressing with the same speed. For a typical structural material or Newtonian material, the Young's Modulus is the slope of stress divided by strain, which presents the stiffness of this material.

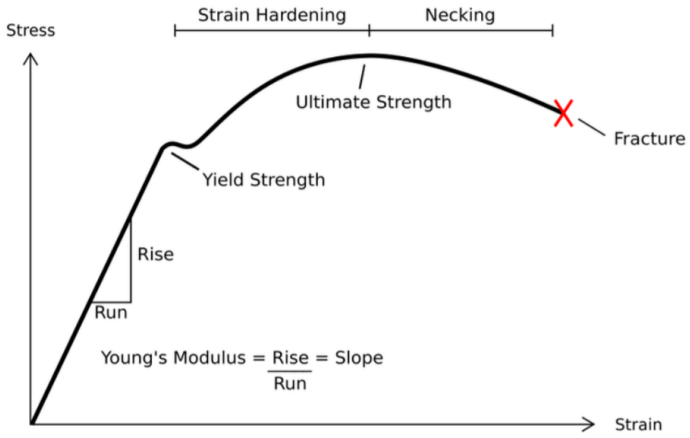

Figure 5.1: A stress-strain curve for a typical structural steel.[130]

However, for a non-Newtonian material, the Young's Modulus changes depending on the external force frequencies. On the stress-strain curve, the slope of the curves change along with the deformation. The Young's Modulus at this certain deformation speed is defined as the average slope of the curve.

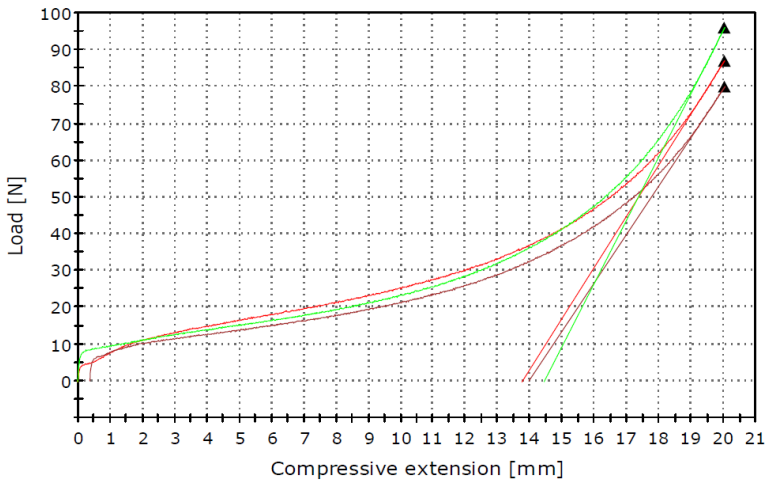

Figure 5.2: One group of the stress-strain curves measured for Silly Putty ™ (by author).

5.2.2 Experiment Preparation and Procedures

This experiment was conducted with the INSTRON 5900 at Advanced Composite Training and Development Centre based in Broughton. Silly Putty samples were prepared as cubes of material before the test. These cuboid samples had the same

bottom surface of 40mm × 40mm, but with different height of 20mm, 40mm and 80mm. These samples were then immediately mounted on the sample holder of the INSTRON 5900 because this non-Newtonian material could deform significantly even only under gravity. It was for the same reason that, in this experiment, the samples were compressed rather than stretched.

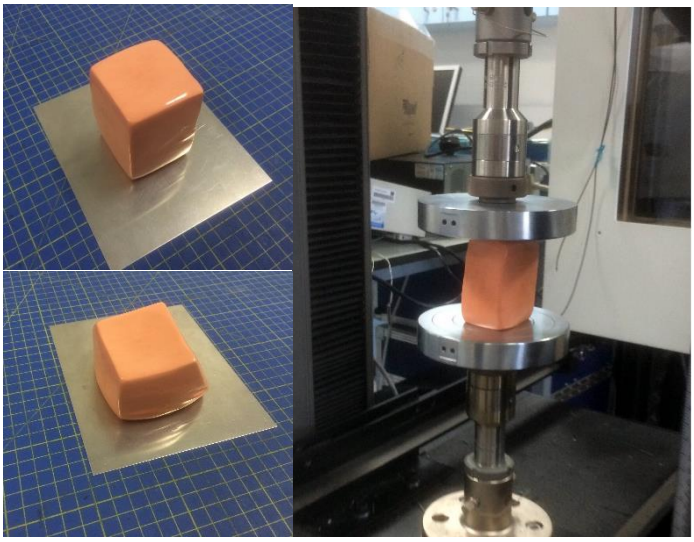

Figure 5.3: One of the Silly Putty samples deforms under the gravity within 10 min (left) and the test procedure to achieve stress-strain curves (right).

In order to determine the Young's modulus of Silly Putty with different external forces, the compression tests were tested with different strain speeds, which include $0.5\% \cdot s^{-1}$, $1\% \cdot s^{-1}$, $5\% \cdot s^{-1}$ and $10\% \cdot s^{-1}$. As 3 samples were tested in this experiment, 12 stress-strain curves in total were achieved for further analysis.

5.2.3 Characterization Results and Analysis

The stress-strain curves were tested for the three silly putty samples with different strain rates. The Young's Modulus was achieved by calculating the average slope of the curves. It turned out that the Young's Modulus of this non-Newtonian material increased with the addition of the strain rate and this trend applied to all the samples.

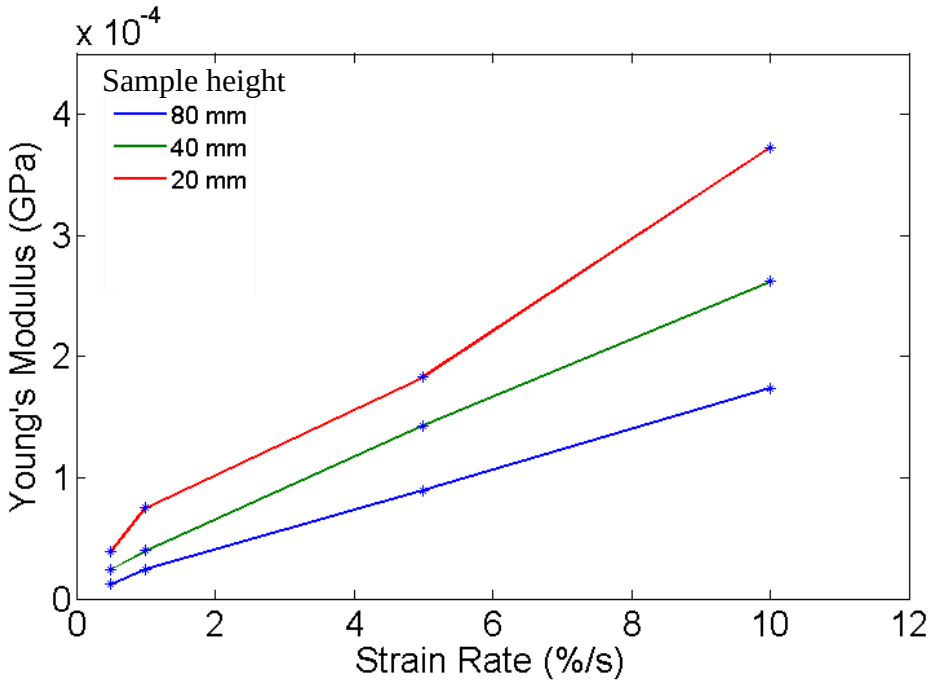

Figure 5.4: The Young's Modulus for non-Newtonian Materials with different strain rate.

5.3 Simulation for Generating Influence Function using non-Newtonian tool

5.3.1 Aim

The aim of this simulation was to find the relationship between the tool spindle speed and the tool influence function, with the purpose of guiding future practical experiments. A tool was designed infilled with non-Newtonian Material in order to reduce the misfit during the processing. The model for this simulation was generated by SolidWorks and the finite element analysis (FEA) was completed by ANSYS software.

5.3.2 Simulation procedures

The modelling experiment was to simulate the practical experiment for generating tool influence functions with different tool rotation speed of 33 rpm, 100 rpm and 300 rpm. Usually, these experiments are conducted by lowering a rotating tool on to a part surface with a defined slurry. By comparing the surface profile before and after the processing, the material removal of this area can be determined, which is also known as the 'Tool Influence Function'.

This simulation was divided into three steps. 1) The first step is conducted with SolidWorks to generate the 3D model of the tool and workpiece surface. 2) In the second step, the model was imported into the ANSYS software for FEA in order to calculate the pressure distribution of the rotation tool. This procedure included definition of material properties, connections setup, mesh, initial conditions setup and final calculation. 3) Simulated tool influence functions were calculated using MatLab according to Preston's Law.[13]

5.3.2.1 Generation of the tool model

The model generated by Solid Work was assembled by 4 parts, which is shown in **Figure 5.5**. The glass provided a flat working surface for the simulation experiment. The diaphragm is made from a flexible material fabricated by Marsh Bellofram Corporation[131]. Non-Newtonian material was infilled to the bellofram to reduce the misfit. A tool back plate was used to seal the non-Newtonian material in place, and provided a tool-interface.

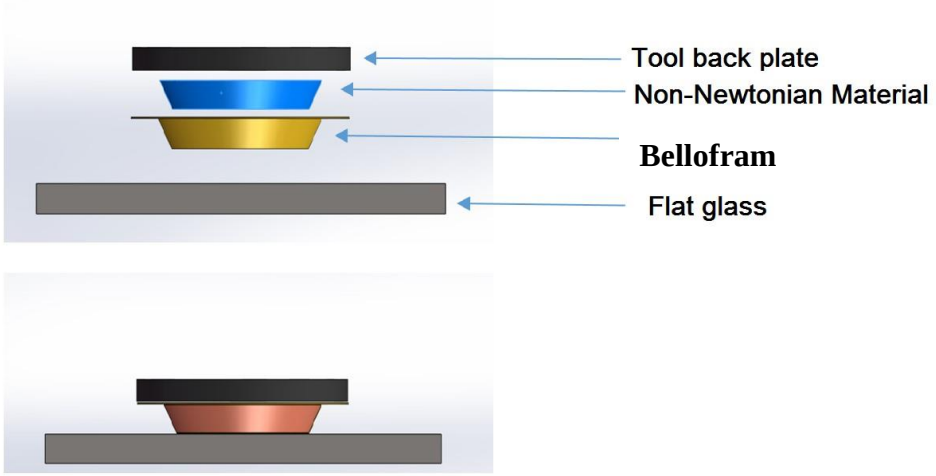

Figure 5.5: The separated parts (up) and assembly (bottom) for the non-Newtonian tool working on a flat surface.

5.3.2.2 ANSYS FEA simulation

1) Define material properties

It was necessary to import material properties, including Young's Modulus, density, hardness, etc., into the FEA software before setting other parameters. In this simulation, the Young's Modulus for non-Newtonian material was not a constant and could not be set by entering a certain value. Instead, the stress-strain curves measured with different strain rate were imported and the ANSYS software was able to define the non-Newtonian material properties under different conditions.

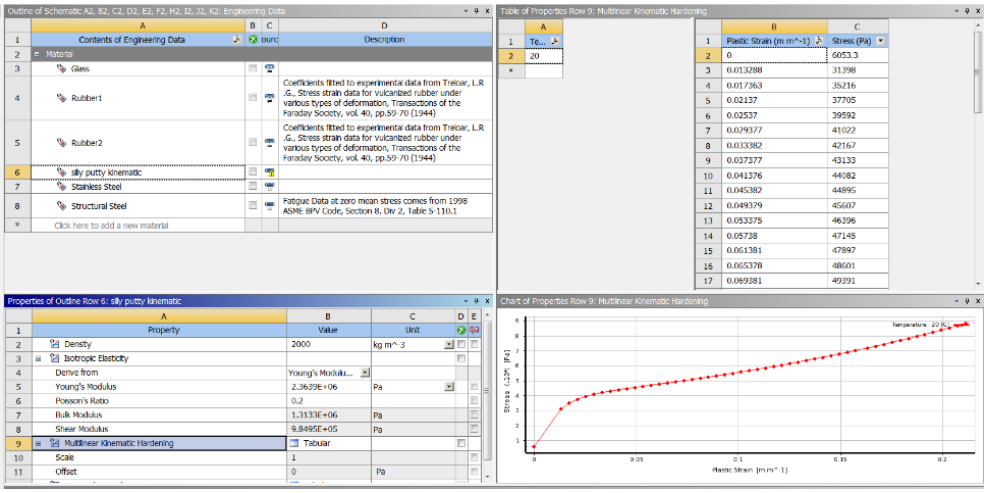

Figure 5.6: Importing stress-strain data to ANSYS FEA software.

2) Connections setup between each part

The non-Newtonian material was set in the model to deform freely between the tool back plate and diaphragm. The tool back plate and diaphragm were bounded together to seal the non-Newtonian material within the tool. The connection between the flat glass surface and the diaphragm was set to be frictional with coefficient of 0.2 according to the typical coefficient of friction between rubber and glass.

In practice, a part surface was not polished with rubber but with a flexible pad stuck to the rubber. In this simulation, the thin polishing pad was not generated to simplify the model in order to reduce the overall calculation time and reduce the probability of errors.

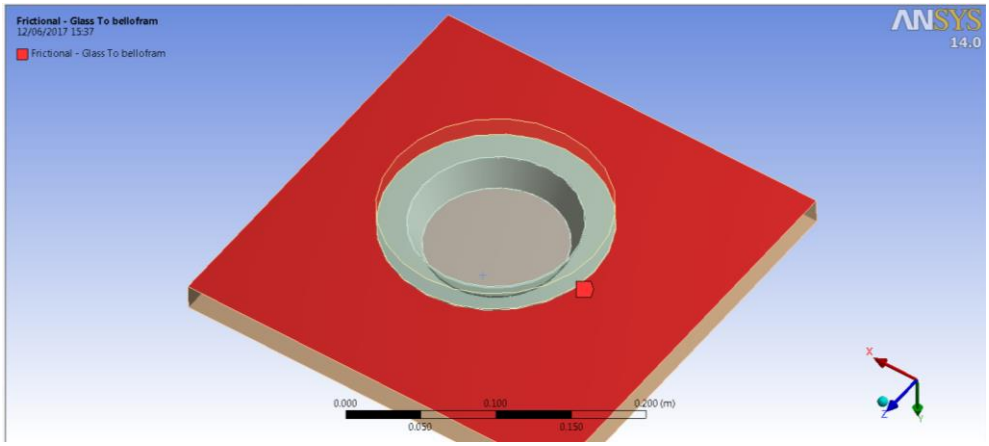

Figure 5.7: Set connection relationship between each part.

3) Mesh

There were three options for the mesh of the model: fine, medium and coarse. In order to reduce the system error of the modelling, the mesh was selected to be fine in this simulation experiment.

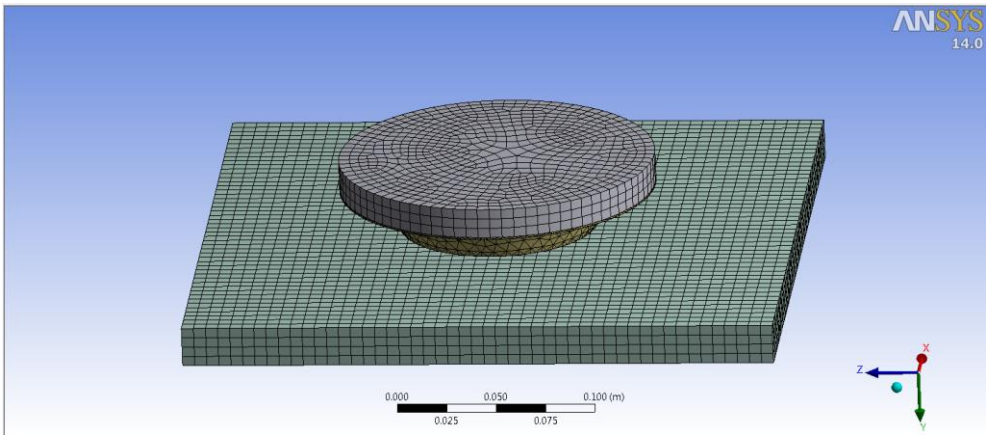

Figure 5.8: Mesh of the model using fine cells.

4) Conditions setup

Practically, the rotating tool is floating on the workpiece surface and remove material under its own weight. In this simulation a force equal to the gravity of the tool was applied on the top of the tool so that the tool was able to remove material.

The initial rotation speed was appiled to the tool back plate before the final calculation. As the diaphragm and tool back plate were bonded together in this simulation, the whole tool was be able to rotate with the specified speed (33 rpm, 100rpm and 300 rpm).

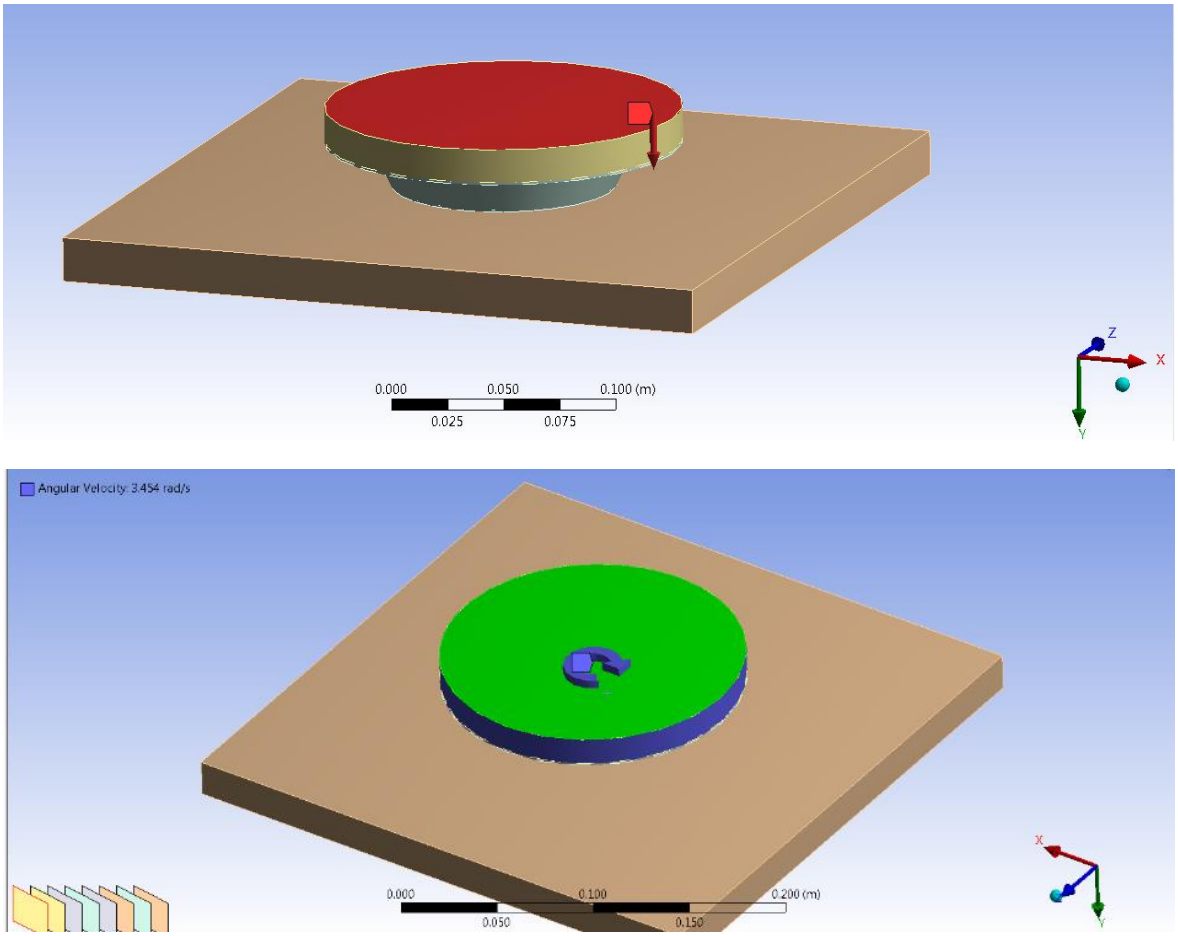

Figure 5.9: Set pressure (up) and rotation speed (down) as the initial conditions.

The processing time for each simulation experiment was shown in **Table 5.1**. In order to achieve similar overall material removal. The run time was set longer for slower

spindle speed. The results of the multiplication between Spindle Speed and Run Time are equal.

Table 5.1: The time set for each simulation experiment.

Spindle Speed	33 rpm	100 rpm	300 rpm
Run Time	180s	60 s	20 s

5) Calculations for pressure distribution

Then the pressure distribution of the tool with 3 different rotating speed was calculated by the FEA software. The data was exported for further analysis.

5.3.2.3 Calculation for the Simulated Tool Influence Function

Once the pressure distribution of the tool was achieved, the data was imported to a MatLab code written by the author to calculate the material removal by integrating the pressure times the velocity over time. The code details are shown in the **Appendix D**.

5.3.3 Simulated Results

5.3.3.1 Simulated Pressure Distribution

The predicted pressure distribution of the tool surface with 3 different rotation speed is shown in **Figure 5.11**. The results showed that the pressure is distributed evenly on the tool surface at rotation peed below 100 rpm. However, pressure concentred in the peripheral zone at the higher tool rotation speed of 300 rpm, which may be explained by the Weissenberg effect.

The Weissenberg effect is a phenomenon that occurs when a spinning rod is inserted into non-Newtonian fluid. Instead of being thrown outward, the solution is drawn towards the rod and rises up around it.[132]

Figure 5.10: Spinning Newtonian (left) and non-Newtonian (right) fluid.[133]

This phenomenon is related to the elasticity of the fluid. Soto, Enrique[134] and co-workers also reported that not only with a spinning rod, the Weissenberg effect was also observed without a rod. It has been tested that both Newtonian and non-Newtonian fluid were put at the centre of a spinning disk for comparison. The Newtonian material fluid trended to flow from centre to the side of the disk, while on the other hand, the non-Newtonian fluid flowed to the opposite direction and emerged from the disk centre.

In this report, the rotating non-Newtonian tool exhibited some properties of the ‘stirring tool’, and the non-Newtonian material in this rotating tool had the tendency to leave a vacancy at the bottom centre. Therefore, the pressure on the centre reduced and concentred on the edge over the increase of the rotation speed.

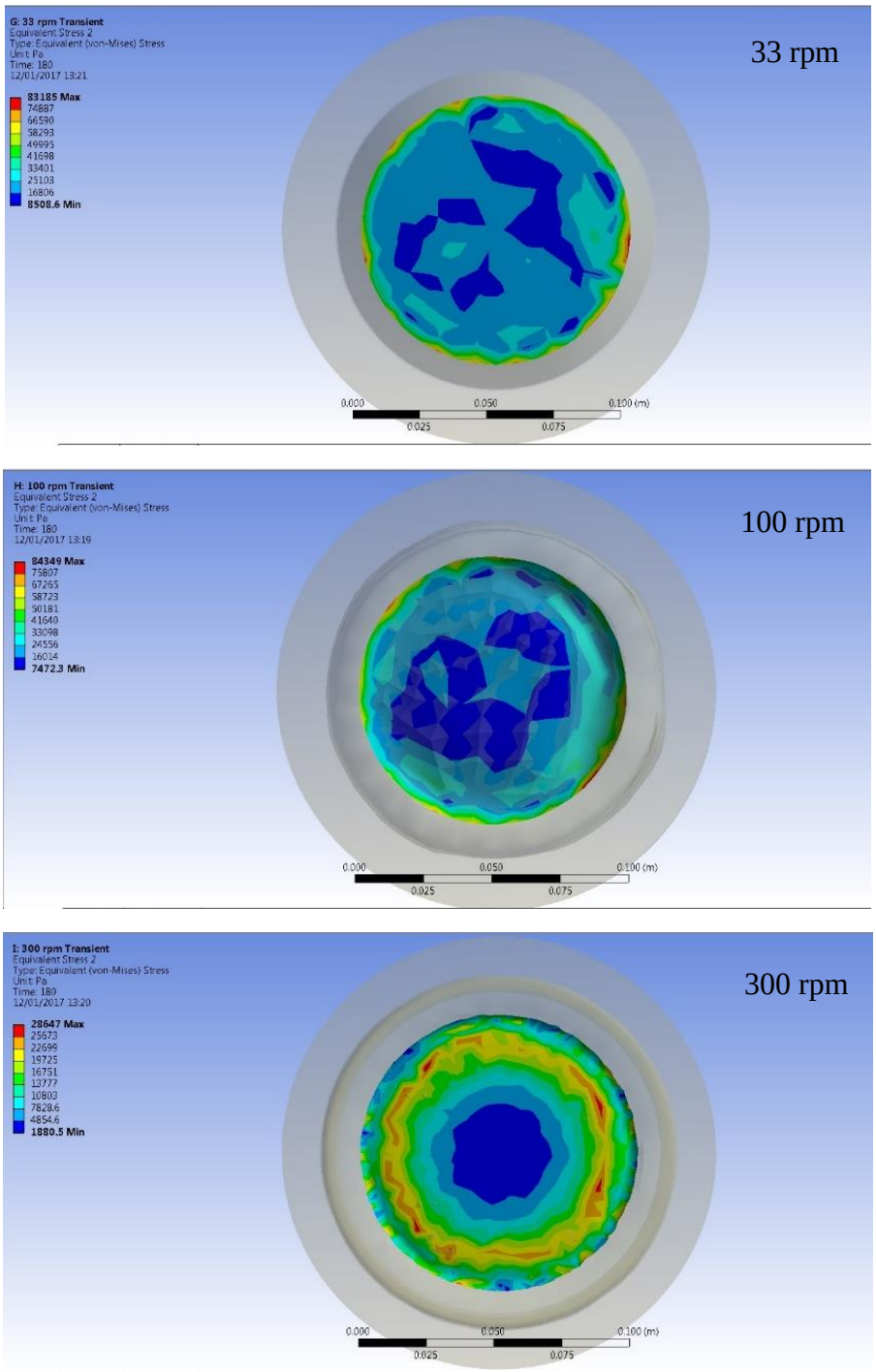

Figure 5.11: Simulated pressure distribution of the non-Newtonian tool working on a flat workpiece surface with different rotation speed of 33 rpm, 100 rpm and 300 rpm.

5.3.3.2 Simulated tool influence function

The results of simulated influence function generated by MatLab are shown in **Figure 5.12**. The contact area has a diameter of 100 mm. At 33 rpm rotation speed, the pressure was evenly distributed over the tool size, and the influence function appeared to be flat. At higher rotation speed of 100 rpm, the removal depth started to have fluctuation but did not have significant concentration. At 300 rpm, the removal was concentred at the edge of the tool, and other place on the centre did not have obvious material removal. The influence function at 300 rpm was like being generated by a ring tool. It will be discussed later in Chapter 6 that this will reduce the mismatch between the tool and workpiece surface.

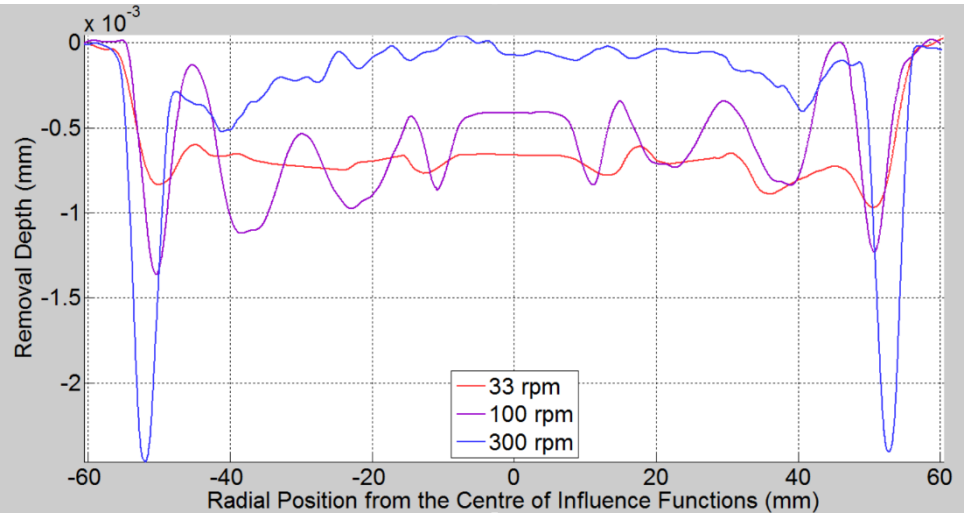

Figure 5.12: Simulated tool influence functions with different tool rotation speed.

5.4 Validation Experiments

5.4.1 Experiment Procedures

Three experiments were conducted to generate tool influence function with a non-Newtonian tool. The results were compared with the simulated influence functions. The procedures for conducting these experiment were the same as the one introduced previously in Chapter 3. The experiments were conducted with same parameter used for simulation experiments, shown in **Table 5.1**. A diamond pad (100 mm in diameter) with a centre hole of 20 mm in diameter was attached to the diagraph in these experiment.

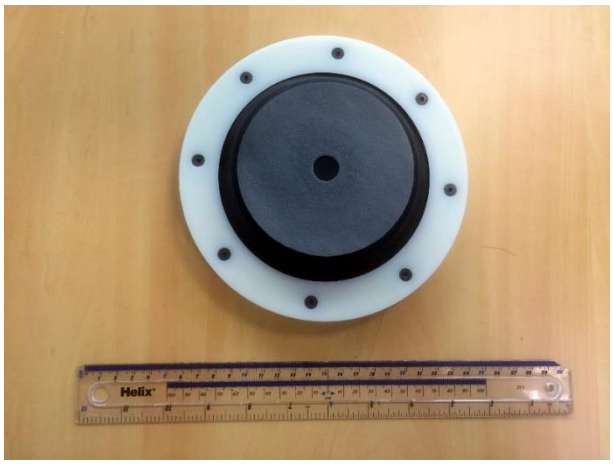

Figure 5.13: The tool with non-Newtonian materials used to conduct validation experiments.

5.4.2 Comparison of Experiment and Simulation Results

Results of validation experiments and simulated influence functions are compared in this section. Surface profiles shown in red represents the measurement results and the results shown in blue comes from the simulation experiments.

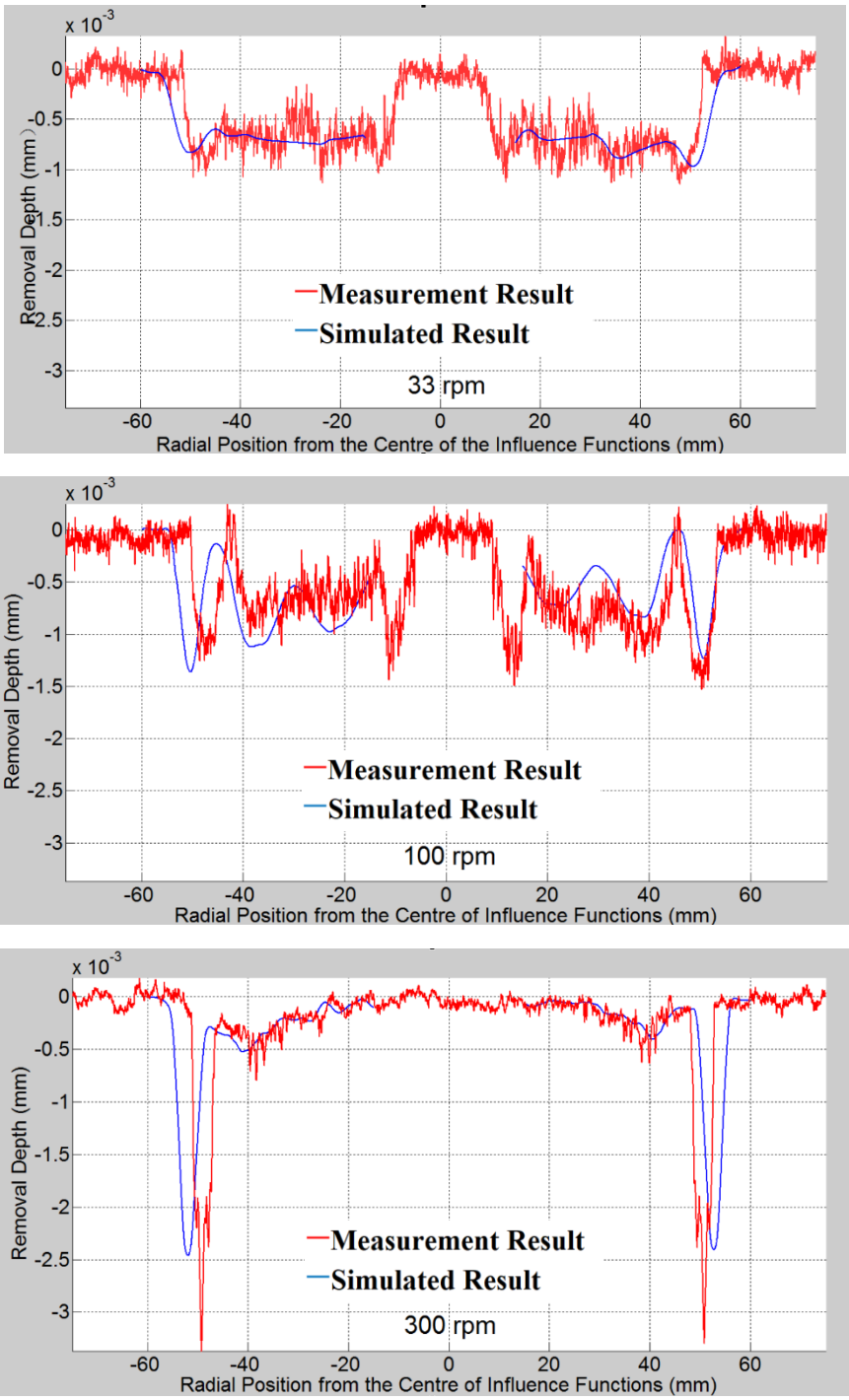

Figure 5.14: The Influence Functions conducted by a non-Newtonian material tool with different spindle speed of 33 rpm, 100 rpm and 300 rpm.

The diamond pad used in validation experiments had a hole in its centre, which means that the removal rate was close to zero (because the velocity was close to zero) and pressure was concentrated around the edge of this hole. However, in the simulated model, the tool surface was a complete disc so that the centre of the influence functions were not compared. This might affect the simulated material removal and lead to a mismatch of the results achieved from the simulation and practical experiments.

In order to qualify the difference of the curves measured in the practical experiments and calculated in the simulation, the standard deviation of each pair of curves are calculated and shown in **Table 5.2**.

Table 5.2: The standard deviation of the measured and simulated curves.

Spindle Speed	33 rpm	100 rpm	300 rpm
Standard Deviation	4.3%	7.7%	9.8%

As shown in **Figure 5.14** and **Table 5.2**, the simulated influence functions have the same trend from low rotation speed of 33 rpm to higher speed of 300 rpm. The standard deviation increases with the spindle speed. This may be caused by the stress concentration, which leads to the increased peak-to-valley value of the curves from 33 rpm to 300 rpm.

The standard deviations under different rotation speed are no more than 10%, which means the measured and simulated curves match well with each other. This comparison has created enough confidence for the simulated results to be accepted.

5.5 Conclusion

A non-Newtonian material (Silly putty ^{TM}) was characterized in this chapter to measure its Young's Modulus with different external forces, which proved essential data for the simulation of influence function using non-Newtonian tool. According to the simulated results, the pressure distribution of the tool surface changes over the increase of rotation speed. The pressure trended to concentrate on the edge of the tool at high rotation speed, and the non-Newtonian tool performed like a ring-tool. This is helpful for applying the non-Newtonian tool to the practical surface processing.

Validation experiment had proved the correctness of the simulated results. The standard deviations of the measured and simulated curved are no more than 10%, which means the theses curves matches well with each other. The increased standard deviation over the spindle speed may due to the stress concentration of the non-Newtonian tool surface during processing.

The next Chapter will introduce the implication of non-Newtonian tool to the surface processing, especially for aspherical and free-form surface. It showed obvious advantage as the misfit between tool and workpiece surfaces could be effectively controlled.

Chapter 6. Mid-Spatial Frequency Control on Aspherical and Free-from Surfaces

6.1 Introduction

The previous experiments introduced in chapter 3 and 4 have demonstrated that the grolishing technique using tools with metal button or diamond pad could effectively remove mid-spatial errors on flat optics faster than polishing. Mismatch between the surfaces of tool and workpiece will introduce new periodic errors onto the surface. This phenomenon can be controlled by either pre-smoothing the metal tool to match the surface form or applying an extra flexible layer for the tool using diamond pad. However, it has not been demonstrated that this grolishing technique has ability to work effectively on aspherical or free-form surfaces. A tool with a metal surface can never properly conform to the aspherical surface even when it is trimmed to the nearest spherical form. The tool with flexible layer used in chapter 4 has been demonstrated that it has difficulty to adapt to the curved surface properly, which generates new surface errors.

In order to reduce the misfit between tool and workpiece surfaces, silly putty ™ was used as the non-Newtonian material to insert between the tool surface material and back plate. The flexibility of this materials changes along with the frequency of external force. For this experiment, the tool spindle speed controls the misfit between tool and workpiece surfaces. In this chapter, this technique is applied to a thin glass with free-form surfaces generated by a glass bending rig to control the mid-spatial frequency errors.

When the tool works on an aspherical part, there are two kinds of misfit during the processing. One is due to the rotational of the tool, and the other is due to the transversal along the surface. In this experiment, the majority misfit is caused by the rotation of the tool. This is because that it leads to high force frequency and the non-Newtonian material cannot deform quickly enough to properly conform to the surface. This phenomenon has been simulated and explained by Kim and Burg of University of Arizona.[135] To reduce the rotational misfit, a non-rotating orbital tool was designed and tested on an aspherical part to demonstrate that it does not introduce new MSF errors. This technique was also successfully applied to remove the mid-spatial errors on an aluminum off-axis aspherical part. The mechanism of this independent design is introduced, and its performance are commented in this chapter.

6.2 Grolishing with a non-Newtonian Tool on Glass with Free-form Surfaces

6.2.1 Experiment setup and procedure

6.2.1.1 Bending Rig

In this experiment, the glass was bent by the equipment shown in **Figure 6.1**. To generate free-form surface. A piece of thin glass with thickness of 3mm was attached to an aluminium plate and mounted on a stainless steel supporter. A cuboid bar attached to the plate is connected with a screw and the glass was bent by turn the screw nut underneath the equipment. The degree of curvature is decided by the number of turns. ISOPON™[136], a flexible polyester material, was used to fill the gap between aluminium plate and the supporter. This material has a characterization to become hard after air-dry for 30 min, which makes a perfect supporting layer with the same curvature

of the aluminium plate to reduce uneven stress and further deformation of the glass during processing and metrology.

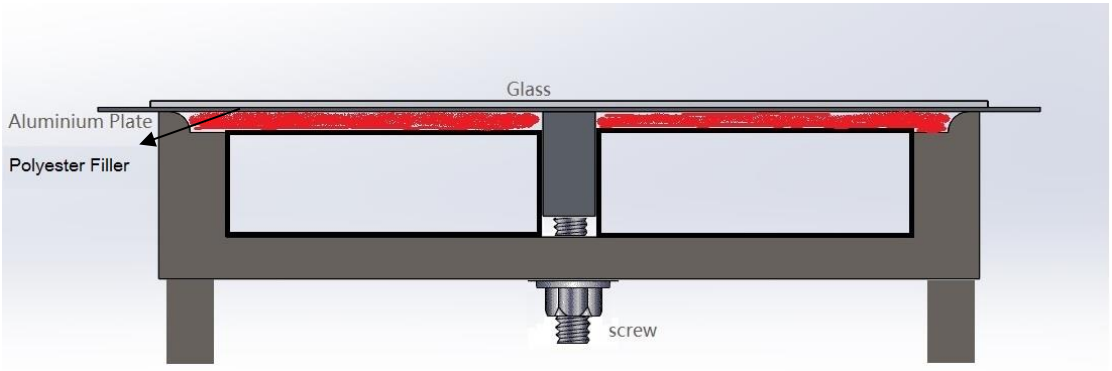

Figure 6.1： The schematic diagram of glass bending equipment.

6.2.2.2 Pre-metrology and Grolishing procedure

The stressed mirror equipment was used for generating the saddle−shape free-form surfaces. After being adhered to the bending equipment, the 3mm thick glass was first smoothed with 9μ alumina abrasive to remove potential residue texture on the surface. It was then pre-polished by Zeeko 1200 mm and measured by a 4D-600 interferometer to ensure the surface do not have any mid-spatial errors left from previous procedure. As can be seen from the interferogram shown in 错误!未找到引用源。, there are not any visible spatial errors left on the surface. Thus, if any surface error are discovered after the experiment, it can be confirmed that these errors are introduced during the grolishing procedure.

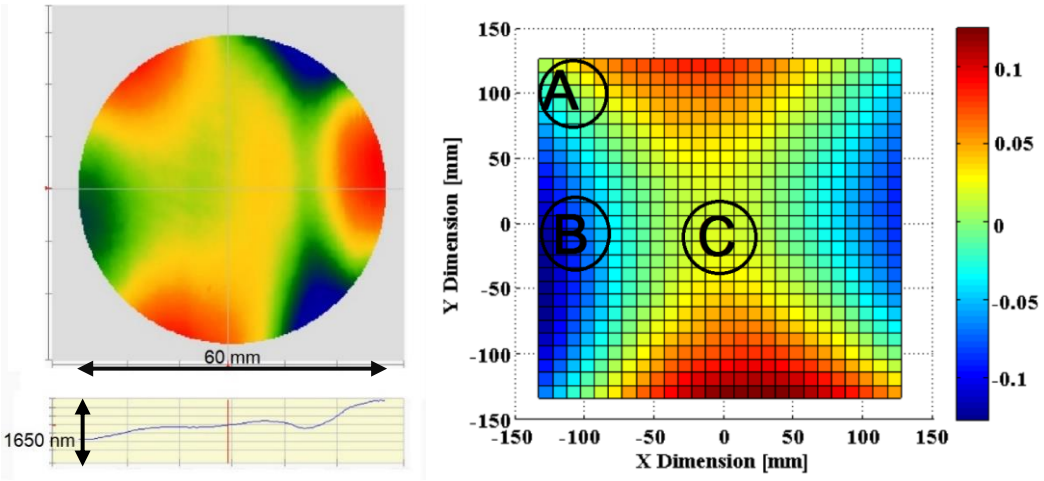

Figure 6.2： Interferogram of glass surface before grolishing (left) and measurement result of the glass surface form on the stressed mirror equipment (right)

Then, the glass surface form was measured by the Zeeko probing technique[119], which is also used to measure the tilt of the workpiece surface. The uncertainty of this method is within a few microns. Zeeko IRP 600 was used for the metrology of this freeform surface. A probe has been attached to the polishing arm and measured the relative height of a 4×4 matrix of points on the freeform surface. The result data was exported by Zeeko TPG softwar and then plotted using MatLab, which is shown in 错误!未找到引用源。. The surface form looks like a saddle. 3 positions (A, B and C) were selected from the corner, edge and centre of the surface. The surface slope changes quicker at A than B and B than C. So during the surface processing, the misfits at these 3 positions are expected to have the following relationship: A>B>C. Interferogram at these 3 positions after each run has been measured and analysed.

Grolishing experiments were conducted with different spindle speed (rpm 33, rpm 100 and rpm 300) and raster tool path track spacing of 10 mm using Fanuc robot. The tool path was generated supposing that this free-form sample has a flat surface, so that we can test ability of this non-Newtonian tool deforms to fill the gap between tool and workpiece surfaces.

(a) **(b)**

Figure 6.3: a) Grolishing experiment on glass stressed mirror equipment using Fanuc robot and non-Newtonian tool; **b)** Polishing with IRP 600 machine as the final finishing procedure (right)

The glass was finally polished by a Zeeko polishing machine to make the surface specular to enable measurement by a 632-8rm interferometer (with beam expander) looking for mid-spatial errors.

6.2.3 Results and analysis

The sample surface was measured by the interferometer at positions of A, B and C of the glass with spindle speed of 33 rpm, 100 rpm and 300 rpm. The results are shown in **Table 6.1**. The dimension of the measurement area is 60 mm and a cross section shown below each interferogram.

As expected, the mid-spatial error is the most serious at A, compared with B and C. According to 错误!未找到引用源。, the slope of the surface changes more quickly at A, compared with B and C, which leads to higher external force frequency at A during the processing. It is easier to have more misfit, if the tool cannot deform quickly enough to adapt the surface form.

With increase of the spindle speed, the non-Newtonian material becomes less flexible and it shows that the mid-spatial frequency becomes clearer at rpm 100 than rpm 33. Interestingly, the mid-spatial error produced by the tool becomes less serious at rpm

300. This could be explained by the Weissenberg effect, which has been descripted at Chapter 5. The simulation shows that with higher spindle speed, the non-Newtonian material tend to climb up around the central axis of the tool. With high spindle speed up to 300 rpm, this effect leads to the contact area between the tool and workpiece becomes a ring rather than a round disk. It has been demonstrated by experiments using ring tool to compare with the round disk tool. The result shows that the misfit of the ring tool is much less than the round tool. This is believed to be the reason that the mid-spatial error becomes more serious with increase of the spindle speed, but finally become less at higher spindle speed.

Table 6.1: The results measured by beam expander at different position of the glass with spindle speed of 33 rpm, 100 rpm and 300 rpm.

RPM	A	B	C
33	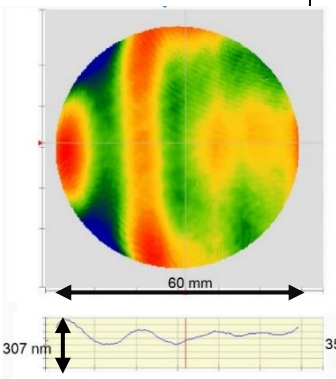	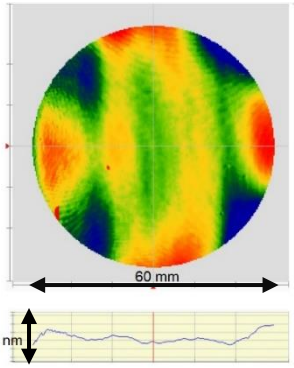	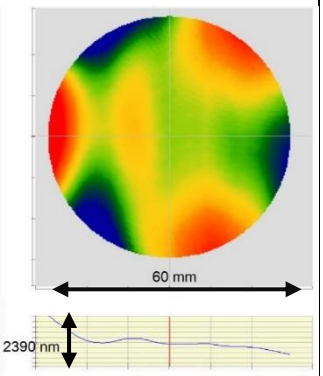
100	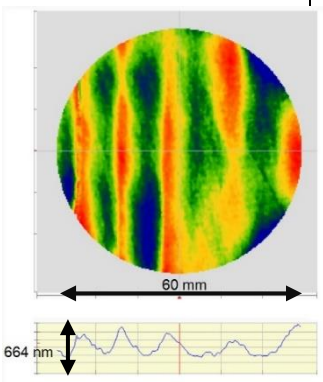	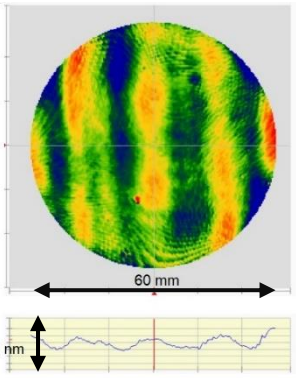	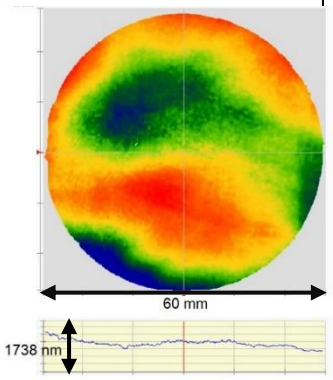
300	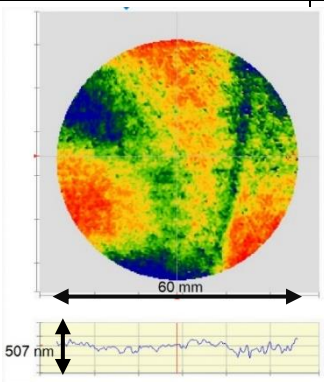	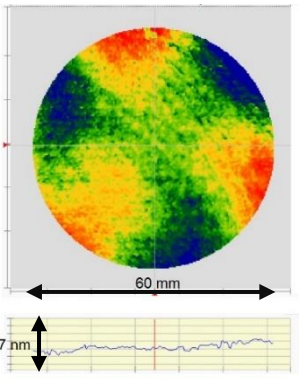	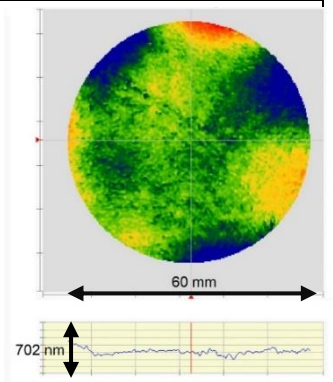

6.3 MSF control on aspherical surfaces with a non-rotating tool filled by non-Newtonian material

6.3.1 Aim

Misfit between tool and work piece surface is always a critical issue for processing asphere surfaces. Imperfect contact between interfaces can lead to periodic defects, i.e. mid-spatial frequencies, which are difficult to be removed by polishing procedures. By using a non-Newtonian tool, the tool surface can gradually adapt to the workpiece surface and reduce the misfit. However, under force variations at >10 Hz, the polymer chains inside the non-Newtonian material are limited in the ability to deform and reduce the misfit. During the processing procedure, the external force is induced by the local curvature and the curvature along the tool path. The force frequencies are correspondingly decided by tool rotating speed and surface feed rate. In practise, the line velocity of the rotation tool is 5-100 times larger than the surface feed rate, which makes a rotating tool more difficult to adapt to an asphere surface compared with a non-rotating tool. Thus, a non-rotating tool is applied in the grolishing procedure, trying reduce the misfit and remove mid-spatial frequencies.

6.3.2 First Design of Non-rotating Orbital Tool

As discussed **6.3.1**, rotation is the major factor that leads to the misfit between a non-Newtonian tool and workpiece with an aspherical surface. In order to promote the performance of the non-Newtonian tool to adapt to the aspherical surface, the tool should be kept non-rotating while moving orbitally around a centre point. It is like a satellite revolves around a planet without rotation.

Three gears are used to keep one tool from rotating. A cardboard model was made to demonstrate the mechanism. As shown in **Figure 6.4**, the first gear is concentric with the back plate, fixed to the centre shaft and cannot rotate, the second and the third gear are free to rotate and move along with the rotating back plate.

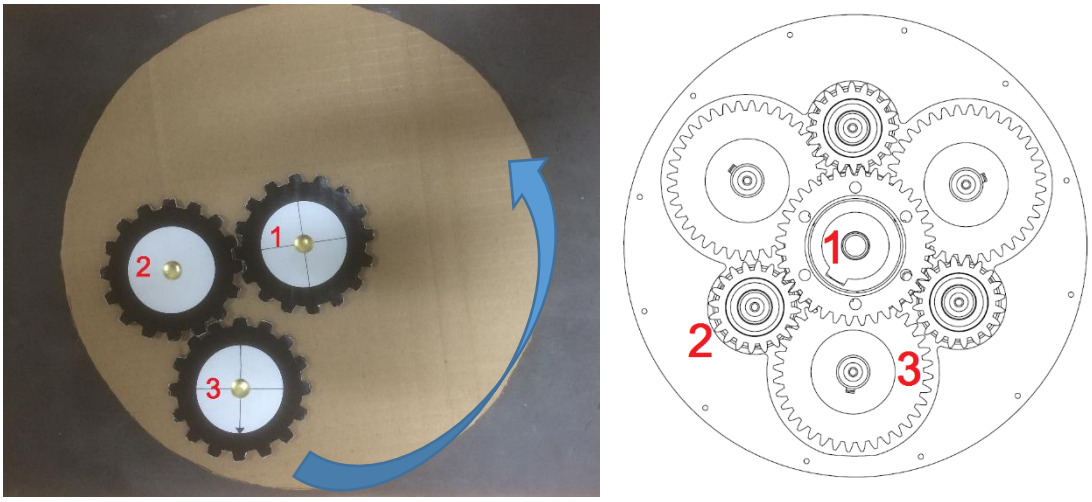

Figure 6.4: Cardboard model of the non-rotating orbital tool to explain its operating principle (left) and CAD design for the non-rotating tool (right).

Table 6.2: Specification of the non-rotating tool.

Contact Diameter	Max. diameter	Weight	Thickness of non-Newtonian layer
50 mm	**90 mm**	**1.5 kg**	**14 mm**

In the experiment using the non-rotating tool with the specification listed in **Table 6.2**, the tool tilted significantly when the robot moved along the tool path. The tool body on the side trailing the tool path could almost touch the glass surface (shown in **Figure 6.5**).

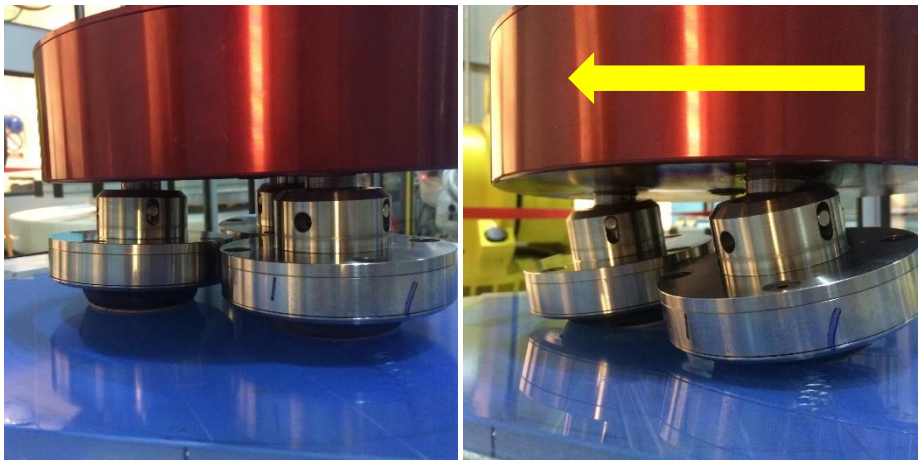

Figure 6.5： Problem of tilting during the experiment: the tool body almost touching the workpiece aspherical surface (left) and the tilt tool moving along the tool path (right).

6.3.3 Possible Solutions

In order to make the non-rotating tool to operate satisfactorily, it requires that

(i) Minimum friction providing sufficient articulation to enable the tool freely to float on a curved asphere surface;

(ii) Optimization of the non-Newtonian layer thickness to ensure that the layer is sufficient flexible to adapt to the asphere surface and not over thick to make the tool tilt.

(iii) Lower the virtual pivot (ideally but impractically just on the top of the workpiece surface) to minimise the moment of the tool;

(iv) A restoring force applied between gearbox and tool to compensate the tool's orientation with equal to the surface when the non-Newtonian material trends to form a wedged;

For the first requirement, the tool was re-machined to trim the joint and apply proper lubrication to the joint.

According to experimental testing, the thickness of non-Newtonian layer has been reduced from 14mm to 8 mm. This is the minimum thickness for the non-Newtonian layer to keep sufficient flexibility to deform. The thickness is reduced so that the non-Newtonian material trend not to form a wedged deposition easily.

To meet the other two requirements, more design was proposed and analysed.

a) Lower the virtual pivot using the current design

b) Spring metal flexure

This method can lower the virtual pivot position and applies more pressure onto the workpiece surface using the elasticity of the spring metal flexure, but requires more accurate alignment and may reduce the flexibility of the tool.

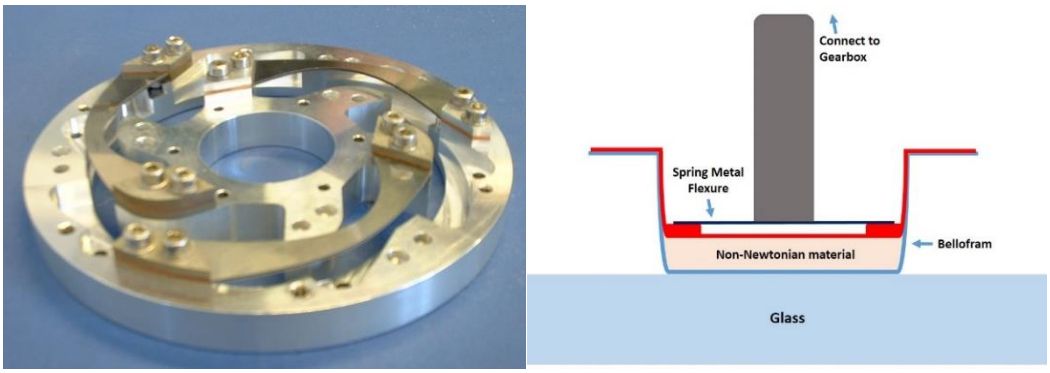

Figure 6.6: An example of spring metal flexure (up) and assembly drawing (down).

c) Correction force

Permanent magnets or springs are placed between gear box and tool. This method applies additional force between the gear box and the top surface of the tool to keep the tool vertical to the workpiece surface during the processing. Considering the relative movement between gearbox and tool, permanent magnets are used to avoid the contact friction. As can be seen from the **Figure 6.7**, when the tool tilts, one side of the tool gets closer to the gear box which lead to more repulsion force, while

the distance on the other side increases and leads to less repulsion force. Overall the system generate a moment pulls the tool aback to be vertical to the workpiece surface.

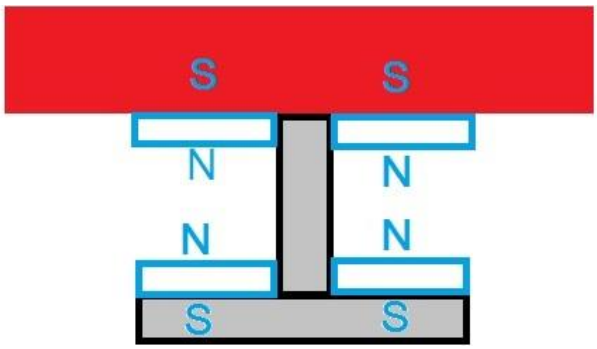

Figure 6.7: Schematic diagram of applying reinforcement between gearbox and tool.

d) Dog Clutch

A dog clutch is a type of clutch that couples two rotating shafts or other rotating components not by friction but by interference. The two parts of the clutch are designed such that one will push the other, causing both to rotate at the same speed and will never slip.[137]

This methods can easily lower the virtual pivot, but not be able to provide more pressure rather than the tool weight. Very significant friction can hardly keep the tool to freely float on the workpiece surface and affect the force distribution.

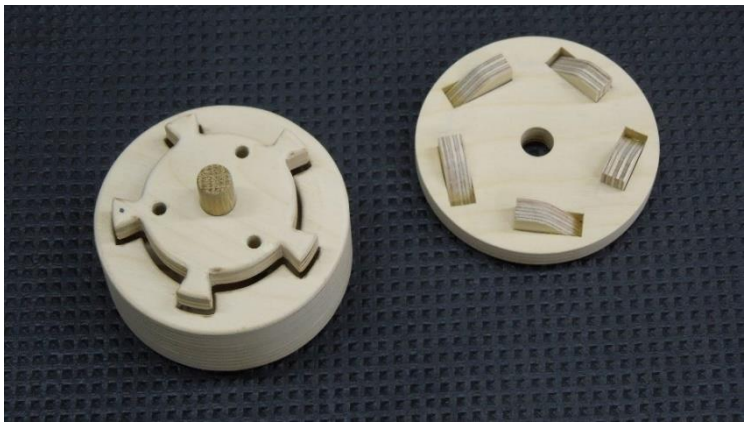

Figure 6.8: An example of dog clutch.

e) Hex socket with Ball driver

This design can be similar with dog clutch, but providing more articulation to float on a curved surface. The ball driver needs to insert into the socket deep enough to drive the tool move along tool path without slip.

Table 6.3: Comparison of different design to optimize the non-rotating tool.

Design	Virtual pivot	Pressure distribution	Articulation	Restoring force	Floating
Lower pin and slot	Good	Require spring	Good	Poor	Good
Spring metal flexure	Good	Good	Medium	Medium	Poor
Permanent magnet	Poor	Medium	Good	Good	Good
Dog Clutch	Good	Poor	Medium	Poor	Medium
Hex socket & Ball driver	Good	Poor	Good	Poor	Medium

6.3.4 Modified tool design

The modified non-rotating tool has retained the basic idea of the original design, which makes it be able to float on the workpiece surface and easy to adjust to the misfit with a flexible layer infilled with non-Newtonian material. In addition, the position of pivot has been lowered so that the tool is less likely to title when it goes along the tool path on an optical sample. In Figure 6.9, both of the pictures are taken while the tool is working along a raster tool path. It is clearly shown that the tilt problem has been solved for the non-rotating tool after this modification.

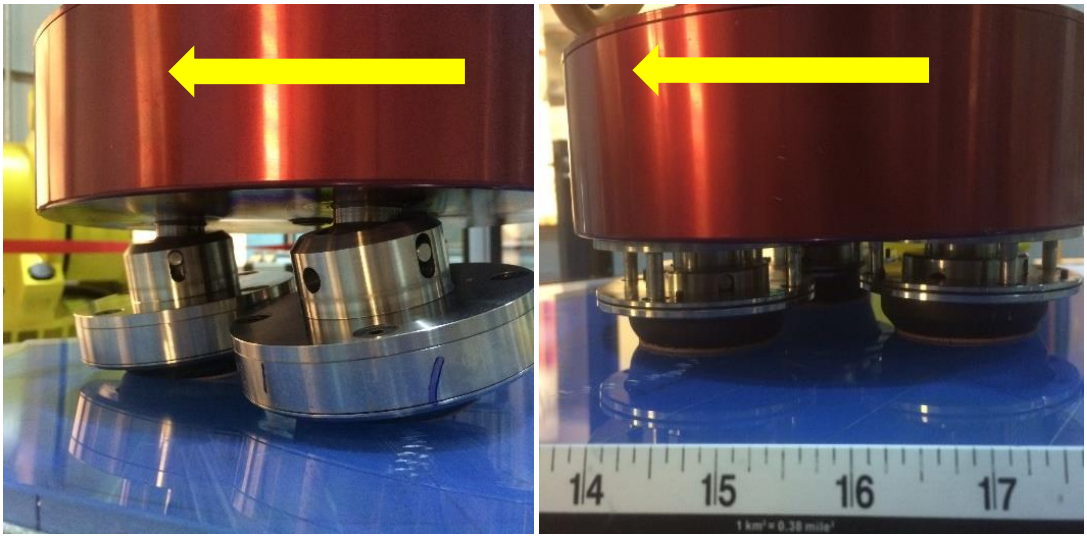

Figure 6.9: A comparison of the non-rotating tool before and after the first modification working along the raster tool path on borosilicate glass.

Before working on an asphere sample, this non-rotating tool has been tested on a pre-polished 3 m radius sphere borosilicate sample about removal rate, stability and texture.

6.3.5 Generating Influence Functions

An experiment for generating an influence function has been conducted using the parameters shown in **Table 6.4**. The sample surface has been measured before and after the influence function experiment by Talysurf and the material removal is calculated and shown in **Figure 6.10**. After analysing the measurement results, the overall material that has been removed in this experiment is 12 mm^3, which makes the volumetric removal rate to be 0.4 mm^3/min.

Table 6.4: The parameters for generating an influence function with modified non-rotating tool.

Duration Time	Spindle Speed	Slurry	Part	Grolishing Pad	Working Weight
30 min	60 rpm	Cero oxide (1.02 g/cm³)	Borosilicate	Polyurethane (⌀ 50 mm)	400 g for each

As can be seen from **Figure 6.10**, the surface texture in the working area (between 60mm-110mm and 60mm-240mm) is inferior to the rest of the place. This occurs with a fixed tool working on a workpiece surface, because a lack of smoothing due to lateral motion. If the rotating tool moves along a tool path over the whole surface, the surface texture can be improved, such as a grolishing tool working along a raster or epicyclic tool path. The overall volumetric material removal rate, 0.4 mm^3/min, is calculated by the software based on MatLab. Based on previous experience, if the tool surface can properly adapt to the workpiece surface, with this material removal rate, the tool can effectively remove mid-spatial frequencies on a glass part.

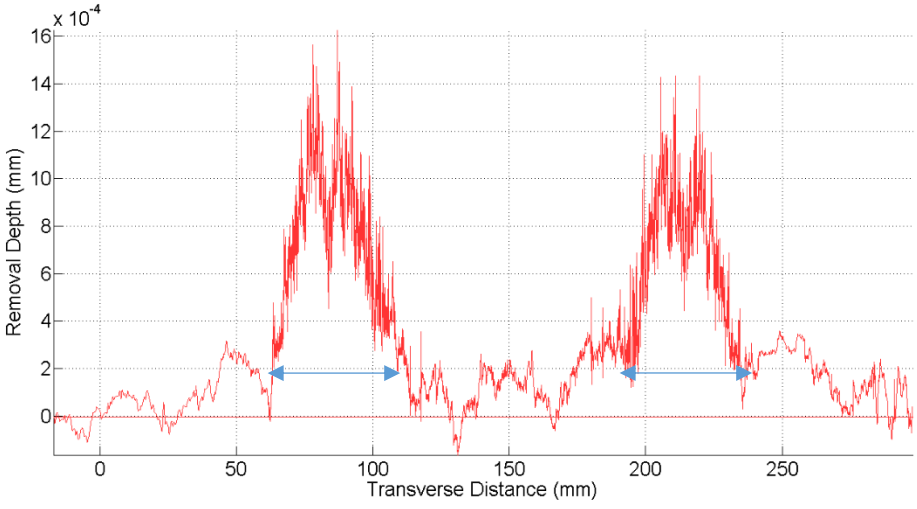

Figure 6.10: Materials removal for the influence function experiment using the non-rotating tool.

In order to demonstrate that the grolishing procedure using this non-rotating tool does not produce new mid-spatial frequency defects on the surface, we used the tool to grolish a pre-polished spherical surface using epicyclic tool path. At the same time, a selected position on the surface was tested by a test plate before and after the grolishing processing to find out if this tool introduce more MSF errors onto the part.

However, it appeared that the robot arm had difficulty to perform with the correct tool-angle orthogonal to the local working area of the part. As this Fanuc robot had only been used working on flat surfaces previously, this problem had not been realised until the preparation of this experiment. In order to solve this problem, the robot arm and tool setup were calibrated as introduced in the next section.

6.3.6 Calibrating Fanuc Robot Arm for Processing Non-flat Surfaces

The Fanuc i-2000B robot arm is used for grolishing an aspherical surface, but it appeared that the robot could only go to the specified positions correctly but with the wrong tilt angle orthogonal to the local working area of the part. The error could be up to 25%（for example, the robot was instructed to jog to a certain position with angle of 8° relative to the X-axis, but the angle was only 6° in practise). It was believed that this problem may be induced by the setup of robot arm and tool interface.

In this section, the mechanical setting, including motor, motor frame, gearbox, non-rotating orbital tool interface, attached to the end the robot arm was tested in order to ensure the whole tool setting was vertically aligned and concentric to the plate by which could effectively attached to the robot. The test was conducted with the help of Yuan Cheng Li, a Ph.D. student of the research team.

The calibration of the setup for the Fanuc Robot is conducted through measurement data collected by the *Romer Absolute Arm*, shown in **Figure 6.11**, a product from *Hexagon Manufacturing Intelligence*. The equipment has been introduced previously in Chapter 2. The 3-D coordinates of the tool setup attached to the Fanuc robot is measured and analysed including: A: Reference plate; B: Tool frame; C: Gear box; D: Top of the tool cylinder; E: Side of the tool cylinder. The measurement results is shown in **Table 6.5**.

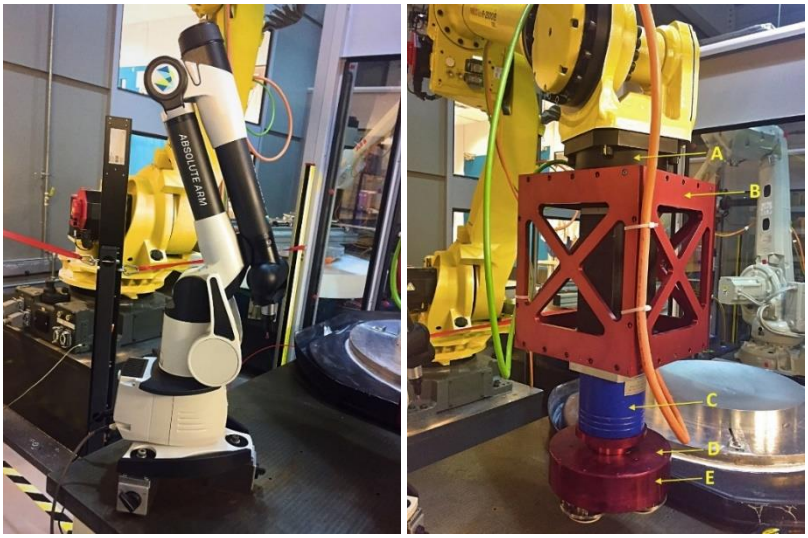

Figure 6.11: The Romer Absolute Arm (left) and the setup of Fanuc robot (right).

It was indicated by the measurement data that the tool has a tilt about 0.2 degree and a noticeable eccentricity error about 1 mm. Then, the error was corrected to complete the calibration.

The robot arm was tested after the calibration to jog to a few test positions. It appeared that the tool attached to the robot arm could job to the specified position with correct angles.

Table 6.5: Tabulation of the alignment measurement data.

MM	**Gearbox Location**		
AX	Nominal	Mean	Deviation
X	0	0.682	0.682
Y	0	-0.861	-0.861
MM	**Tool Location**		
AX	Nominal	Mean	Deviation
X	0	0.784	0.784
Y	0	-1.032	-1.032
DEG	**Tool Plane**		
AX	Nominal	Mean	Deviation
A	180	179.784	-0.216
MM	**Motor Box Location**		
AX	Nominal	Mean	Deviation
X	0	0.27	0.27
Y	0	-0.389	-0.389

6.3.7 Non-rotating epicyclic Tool Working on 3-m Radius Spherical Glass Part

Once the Fanuc robot was calibrated to work on non-flat surfaces, experiments were conducted to validate that the non-rotating epicyclic tool does not leave mid-spatial frequency defect on the surface.

A pre-polished sphere part surface was tested by a standard test plate before the experiment and the result is shown in **Figure 6.13**. To make the surface texture good enough for testing after the experiment, this sphere part was polished rather than grolished by the non-rotating orbital tool with cero oxide slurry for 1 h. As described previously, to reduce the tool misfit, an epicyclic tool path was used in this experiment.

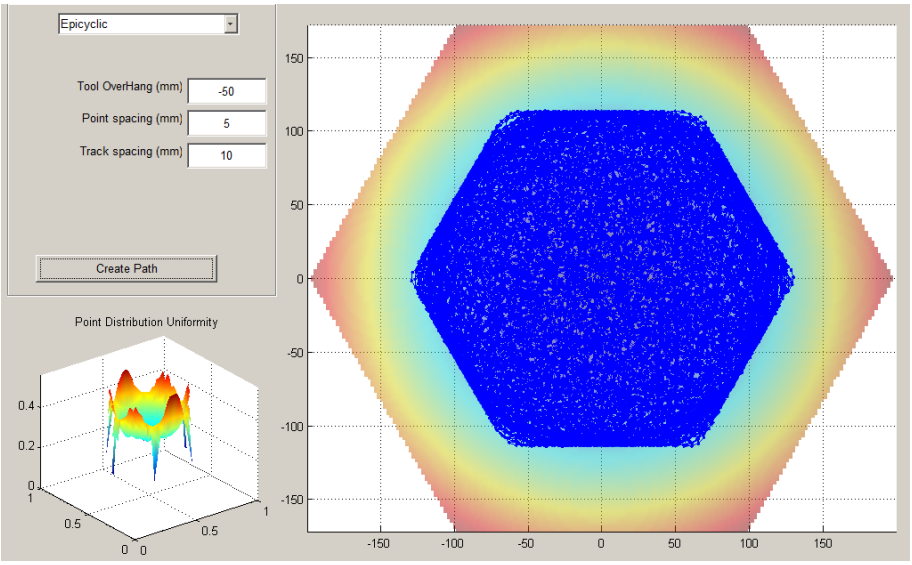

Figure 6.12: The parameters of the epicyclic tool path for grolishing the 400mm surface of the 3 m radius sphere part with non-rotating orbital tool.

Both of the test results before and after grolishing showed smooth concentric circles, which indicated that this grolishing procedure did not leave mid-spatial frequencies on the surface. Otherwise, small bumps will be noticeable along the concentric circles. The white line on the picture is the gap in tape on the back of the part to protect it from being scratched, and the dark line is a reference mark drawn on the workpiece surface.

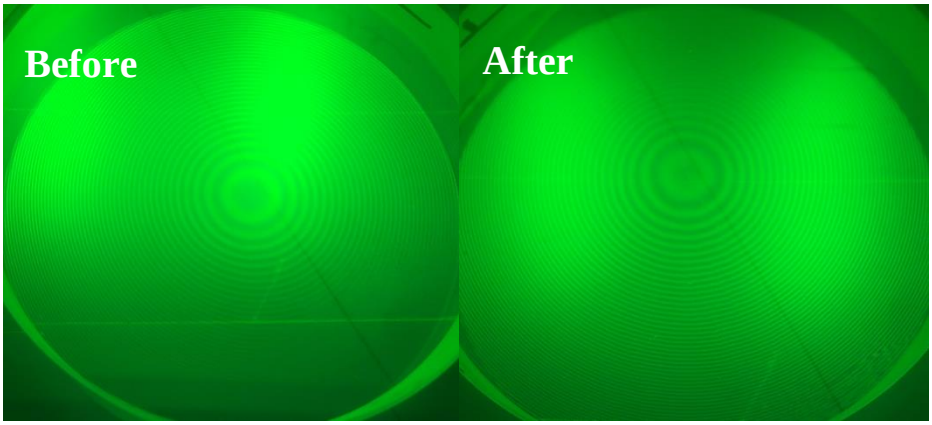

Figure 6.13: Test before and after polishing using non-rotating tool for 60 min with epicyclic tool path.

6.3.8 Non-rotating Orbital Tool Working on an off –axis Parabolic Spherical Aluminium Part

This technique was applied in a project to manufacturing an off-axis parabolic aspherical aluminium part with diameter of 500 mm. The part was machined using diamond turning to a surface form close to the design. This procedure was considered to introduce concentric MSF error to the surface.

In this experiment, polyurethane polishing pads were glued on the surface of the non-Newtonian tool with cerium oxide to removed MSF errors introduced by the diamond turning procedure. A spiral epicyclic tool path was specially generated for this experiment. The surface was tested before and after the experiment using a FISBA interferometer[138], an equipment with specification accuracy better than 10 nm. And experiment procedure and metrology results are shown in **Figure 6.14** and **Figure 6.15**.

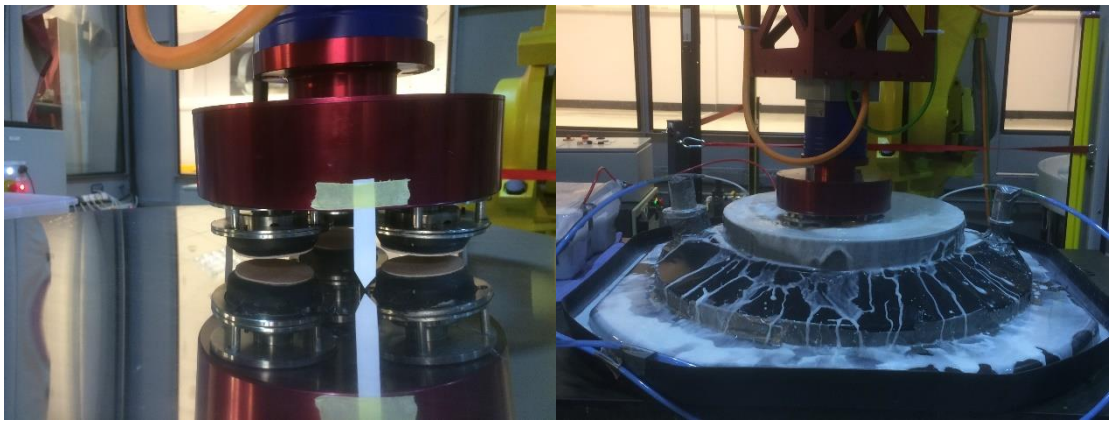

Figure 6.14: Polishing the off-axis aspherical aluminium part using non-rotating orbital tool.

Due to the inadequate surface texture, the interferogram was not achieved completely. But according to the concentric rings shown in **Figure 6.15** (left), it demonstrated that there was MSF error on the workpiece surface before processing. MSF could also be noticed by careful observation using naked eyes.

The interferogram measured after the polishing experiment is also shown in **Figure 6.15** (right)

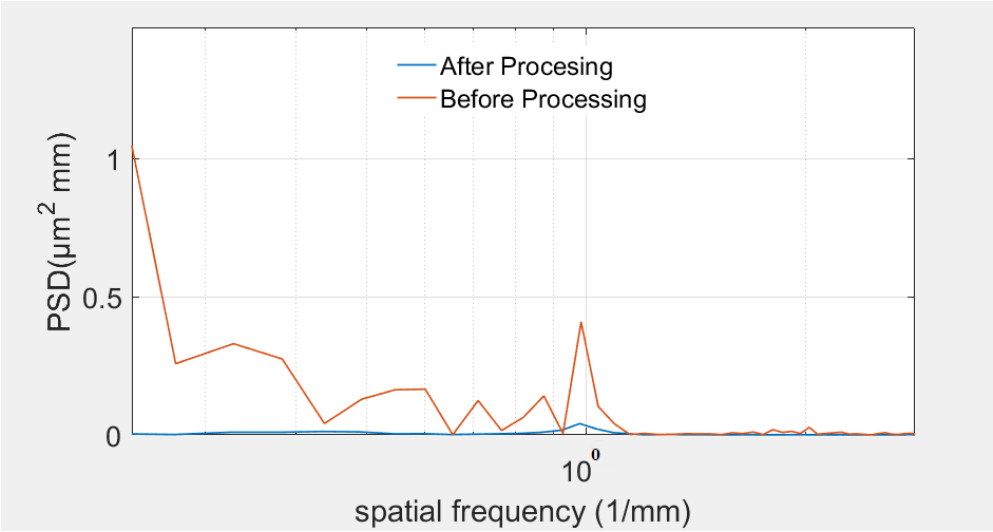

Figure 6.16: PSD analysis of the workpiece surface before and after the spiral polishing by a non-Newtonian tool.

To compare the MSF errors before and after processing, PSD analysis was conducted using the same programme code introduced in Chapter 3. The results can be seen from **Figure 6.16**. The peak at 10^0/mm is reduced from 0.4 μm^2mm to no more than 0.05μm^2mm. Since the accuracy of the interferometer is within 10nm, the PV of MSF error is controlled no more than 10 nm.

. Although there was significant coma caused by the imperfect metrology settings, it was still demonstrated that this spiral polishing procedure had successful removed the mid-spatial errors from the aluminium surface.

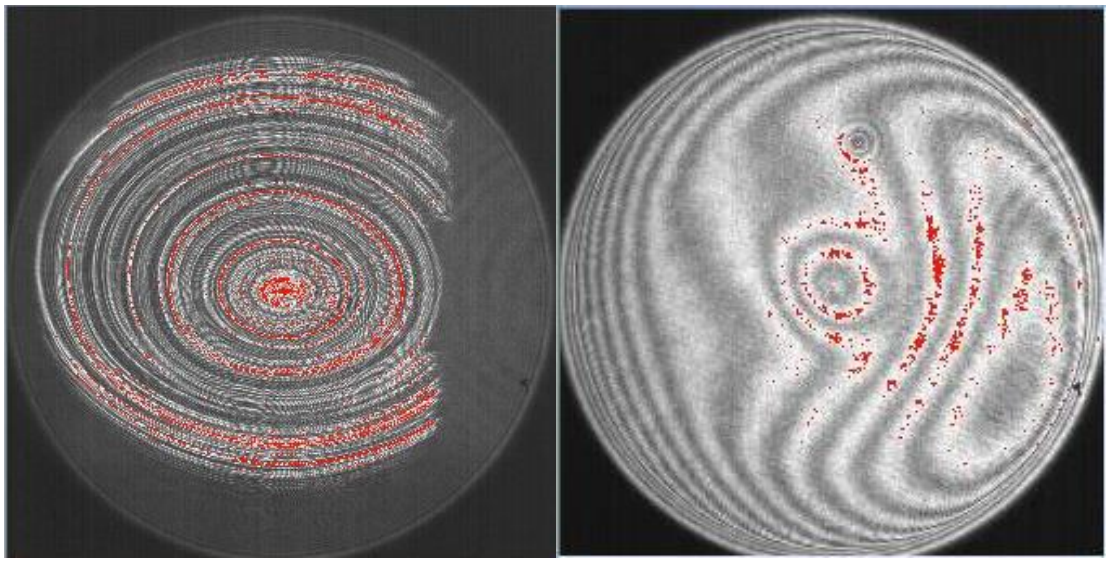

Figure 6.15: Metrology interferogram before (left) and after (right) the spiral polishing by the non-Newtonian tool.

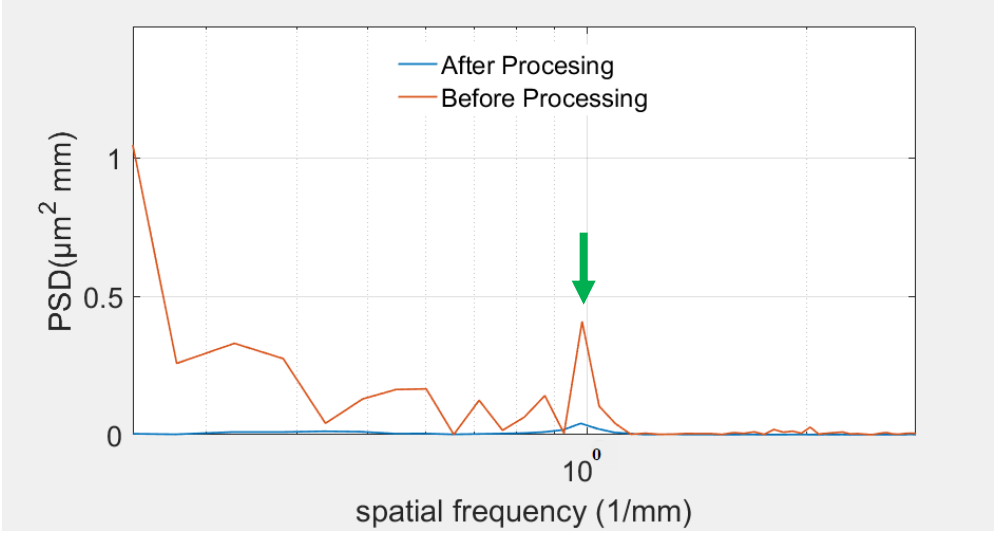

Figure 6.16: PSD analysis of the workpiece surface before and after the spiral polishing by a non-Newtonian tool.

To compare the MSF errors before and after processing, PSD analysis was conducted using the same programme code introduced in Chapter 3. The results can be seen from **Figure 6.16**. The peak at 10^0/mm is reduced from 0.4 μm^2mm to no more than 0.05μm^2mm. Since the accuracy of the interferometer is within 10nm, the PV of MSF error is controlled no more than 10 nm.

6.4 Conclusion

A non-Newtonian tool has been introduced in this chapter in order to remove MSF errors from aspherical and free-from surfaces. Due to its visco-elasticity, the hardness of the tool changes with the spindle speed. It has been demonstrated that at lower tool spindle speed, the non-Newtonian tool is easier to adapt to the saddle-shape free-form surface and reduce MSF errors. However, with higher spindle speed at 300 rpm, the Weissenberg effect was observed and made the contact area between the tool and workpiece surface to become a ring rather than a disk. It make the tool easier to conform to the workpiece surface but may affect the stability of the material removal rate.

In order to reduce the rotation misfit, (which dominates the overall misfit during the manufacturing), between the non-Newtonian tool and part surface, a non-rotating orbital tool was applied to control MSF errors on aspherical surfaces. In the first experiment trial, the tool tilted significantly and failed to complete the process. A few modification plans was proposed and compared in this chapter. After lower the gravity position, the new tool could properly work on a spherical surface. After comparing test result before and after the polishing procedure using this non-rotating orbital tool, it indicated that this procedure could effectively control MSF errors on spherical surfaces. This technique was then applied to remove MSF errors from an off-axis aspherical aluminium part. The PV of MSF has been controlled within 10 nm, which demonstrates the ability of this technique to control MSF errors on aspherical surfaces.

Chapter 7. Conclusions and Future Work

7.1 Summary of Conclusions

It has been articulated at the beginning of the thesis in Chapter 1 that mid-spatial frequency errors could significantly affect the performance of functional surfaces. Outline of this thesis is presented at the end of Chapter 1.

Chapter 2 introduces different manufacturing technologies for processing functional surfaces. It concludes that current technology has difficulty to control MSF errors with a fast and economical approach, which leads to the research for controlling MSF errors that described in this thesis. Metrology equipment used in this thesis are descripted and their accuracy specifications and relative applications are introduced.

Chapter 3 describe a *grolishing* technique using rigid tools and loose abrasive based on Fanuc robot arm. The results indicate that the PV of MSF errors are controlled within 10 nm on flat or sphere surfaces, but this technique could be remove MSF errors on aspherical surfaces due to the misfit problem.

Chapter 4 introduces the application of a flexible bound-diamond pad in grolishing technique. It improves the material removal rate up to 267 mm^3/min and keep the smoothing ability to control MSF errors on flat and sphere surfaces. Glazing effect is discovered and discussed in this chapter.

Chapter 5 introduces simulation experiments using a non-Newtonian tool and its validation experiments. The measured results matches well with the modelling results

with standard deviation no more than 10%. It provides theoretical guidance for the following practical experiments.

Chapter 6 demonstrates that using a non-Newtonian compliant tool could remove MSF errors on aspherical or free-form surfaces. The PV of the mid-spatial frequency is controlled no more than 10 nm.

7.2 Main Contributions of This Thesis

The contributions to knowledge of this research are listed below:

1. Results and analysis of ANSYS FEA simulations to understand the working mechanism of the non-Newtonian material under different stress conditions. The standard deviation of the results is no more than 10%. It provides guidance for selecting parameters in practical manufacturing applications.

2. A non-Newtonian tool is developed and used in a novel way to reduce the misfit between an aspherical workpiece and the tool surface. Peak-to-valley MSF error on an off-axis aspheric part has been better than 10 nm has been achieved. A stressed mirror technique has been developed providing a universal platform for aspheric experiments.

3. Using bonded diamond pads, with various diamond sizes in a ‘grolishing’ procedure to achieve extremely high material removal rates (up to 267 mm^3/min), which improves the overall processing efficiency. The MSF errors are controlled within 10 nm peak-to-valley, on flat and spherical surfaces.

4. Glazing effect is discovered and discussed in this thesis, which provides an aspherical surface after grolishing by a 3-microns diamond pad, with texture of sufficiently quality to be measured *directly* by an interferometer, which usually be achieved only after polishing.

5. Introducing robots in the process of controlling MSF errors, which contributes to the automation of the entire surface processing system.

7.3 Proposed Future Work

7.3.1 ANSYS Simulations for non-Newtonian tool working on a cylinder surface

As introduced in Chapter 5, a simulation has been generated using ANSYS FEA software to predict the performance of a non-Newtonian tool working on a flat surface with different rotation speed. It guides the following practical experiment to choose the suitable experiment parameters.

As discussed previously in **Section 6.1**, there are two kinds of misfit between the tool and workpiece surfaces in the manufacturing of aspherical and free-form surfaces. One is local misfit induced by the rotation of the tool, and another is transverse misfit due to the changing curvature along the workpiece surface. The rotation line speed is usually much faster than the transverse speed, which makes the local misfit dominates during the surface processing.

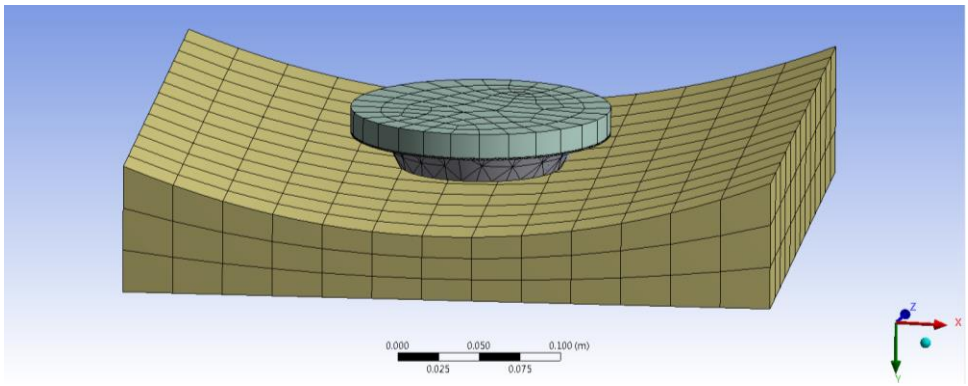

Figure 7.1： FEA model of a non-Newtonian tool on a cylinder surface.

A model was generated using the same non-Newtonian tool working on a cylinder surface to trying to find out if the non-Newtonian tool was able to conform to the working surface with different rotation speed. A cylinder surface was selected for it obvious rotation local misfit compared with conventional aspherical surfaces.

Unfortunately, the simulation experiment was not completed due to the unexpected unconverted function errors. It might be caused by the complex contact area between a flat tool and cylinder working surface. This work should be competed in the future because it would be very helpful for us to understand the performance of a rotating non-Newtonian tool conforming to a complex working surface.

7.3.2 Grolishing with non-Newtonian slurry

As introduced in Chapter 6, the application of non-Newtonian material as the conformal layer has successfully solve the contradiction between flexibility and smooth ability of the tool. It was considered that using non-Newtonian slurry may have similar effect for the MSF control. Preliminary experiments have been conducted, and corresponding experiment procedures and results are introduced in this section. In the relative literatures, this technology is also call shear thickening polishing (STP).

7.3.2.1 Experiment Procedures

The non-Newtonian slurry was first generated by mixing corn flour and conventional cerium oxide polishing slurry with volume ratio of 2:1. Then, mixture was stirred evenly. The non-Newtonian slurry is too thick to be used in the recycling system during the polishing experiment, so the part was immersed in a tank filled with this non-Newtonian slurry.

A borosilicate part (150 mm×150 mm) was located at the bottom of a plastic tank. A pipe with little hole is wrapped around the part at the bottom. Then, the slurry was poured into the tank over the part surface. High pressure nitrogen was imported into the pipe. The gas leaked out from the small holes on the pipe and kept the slurry even during the experiment.

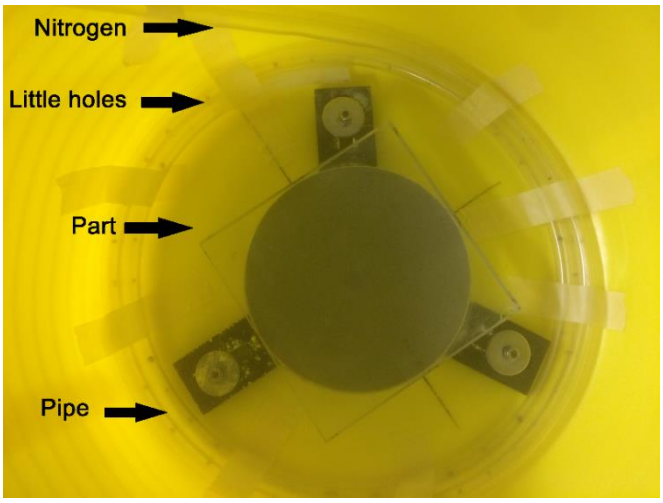

Figure 7.2: Experiment settings.

The part was then polished on the Zeeko IPR 600 machine for 1 hour. The edge area of the part was not polished as the reference for the metrology.

Figure 7.3: Polishing procedure with non-Newtonian slurry.

The slurry was then stored in a ventilated and dry room, but it turned bad after 48 hours. In the future experiment, preservative may need to be applied to the slurry to extend the expiry time.

7.3.2.2 Result and analysis

The surface profiles of the part before and after polishing are measured by a profilometer, and the material removal is calculated, which is shown in **Figure 7.4.**

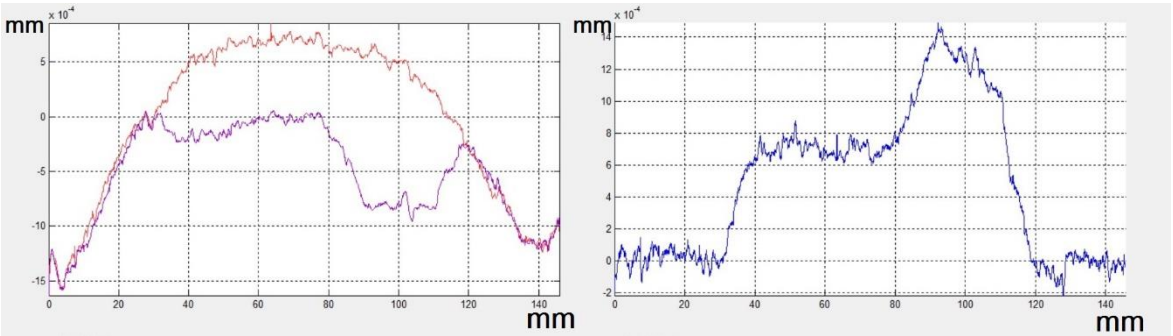

Figure 7.4: Surface profiles measured before and after polishing (left); Material removal during the polishing process (right).

It is shown in the results that the material removal was not uniform in this processing. This may be induced by the precipitation of the slurry, so that the polishing abrasive

was not evenly distributed. It seems that this procedure also introduce new MSF errors to the part surface, which may be caused by the non-deterministic processing.

It is suggested that dispersant agent should be added to the slurry to alleviate the precipitation phenomenon. More effective slurry mixing system should also be applied to the manufacturing processing.

Publications

[1] D. D. Walker. H. Li, G. Yu, X. Zheng and A. Beaucamp, "Research on edge-control methods in CNC polishing." *Journal of the European Optical Society*, 2017.

[2] D. D. Walker, G. Yu, C. Gray, P. Rees, M. Bibby, H. Y. Wu and X. Zheng, "Process Automation in Computer Controlled Polishing." *Advanced Materials Research*, vol. 1136, pp. 684-689, 2016.

[3] D. D. Walker, G. Yu, M. Bibby, C. Dunn, H. Li, H. Y. Wu, X. Zheng and P. Zhang, "Robotic automation in computer controlled polishing." *Journal of the European Optical Society*, vol. 11, 2016.

[4] R. Navarro, J. H. Burge, G. Yu, H.-Y. Wu, D. D. Walker, X. Zheng, et al., "Optimisation of grolishing freeform surfaces with rigid and semi-rigid tools. " in *SPIE Astronomical Telescopes + Instrumentation*, 2016.

[5] D. D. Walker, C. Dunn, G. Yu, M. Bibby, X. Zheng, H. Y. Wu, H. Li, and C. Lu, "The role of robotics in computer controlled polishing of large and small optics." *Optical Manufacturing and Testing XI*, 2015.

References

[1] Y. Qu and S. Field, *Tian Wen: a Chinese book of origins* vol. 624: New Directions Publishing, 1986.

[2] S. Dupré, "Galileo's telescope and celestial light," *Journal for the History of Astronomy*, vol. 34, pp. 369-399, 2003.

[3] G. Galilei, *Sidereus Nuncius, or The Sidereal Messenger*: University of Chicago Press, 2016.

[4] J. M. Rodriguez-Espinosa and P. Alvarez, "Gran Telescopio Canarias: a 10-m telescope for the ORM," in *Optical Telescopes of Today and Tomorrow*, pp. 69-73, 1997.

[5] G. Chanan, D. G. MacMartin, J. Nelson, and T. Mast, "Control and alignment of segmented-mirror telescopes: matrices, modes, and error propagation," *Applied Optics*, vol. 43, pp. 1223-1232, 2004.

[6] R. N. Youngworth and B. D. Stone, "Simple estimates for the effects of mid-spatial-frequency surface errors on image quality," *Applied Optics*, vol. 39, pp. 2198-2209, 2000.

[7] D. Aikens, J. E. DeGroote, and R. N. Youngworth, "Specification and Control of Mid-Spatial Frequency Wavefront Errors in Optical Systems," in *Frontiers in Optics 2008/Laser Science XXIV/Plasmonics and Metamaterials/Optical Fabrication and Testing*, Rochester, New York, 2008.

[8] G. Yu, D. Walker, and H. Li, "Implementing a grolishing process in Zeeko IRP machines," *Applied optics*, vol. 51, pp. 6637-6640, 2012.

[9] G. Yu, H. Li, and D. Walker, "Removal of mid spatial-frequency features in mirror segments," *Journal of the European Optical Society-Rapid publications*, vol. 6, 2011.

[10] D. D. W. C. R. Dunn, "Pseudo-random tool paths for CNC sub-aperture polishing and other applications," *Optics Express*, vol. 16, pp. 18942-18949, 2008.

[11] A. a. Burge, *The Handbook of Optical Engineering* vol. Chapter 28, 2001.

[12] C. Pruss, E. Garbusi, and W. Osten, "Testing aspheres," *Optics and Photonics News*, vol. 19, pp. 24-29, 2008.

[13] F. Preston, "The theory and design of plate glass polishing machines," *J. Glas Tech.*, vol. 11, pp. 214, 1927.

[14] J. H. Burge, B. Anderson, S. Benjamin, M. Cho, K. Smith, and M. Valente, "Development of optimal grinding and polishing tools for aspheric surfaces," in *Proc. SPIE*, pp. 153-164, 2001.

[15] A. McPherson, J. Spyromilio, M. Kissler-Patig, S. Ramsay, E. Brunetto, P. Dierickx, *et al.*, "E-ELT update of project and effect of change to 39m design," in *Proc. SPIE*, p. 84441F, 2012.

[16] D. D. Walker, D. Brooks, R. Freeman, A. King, G. McCavana, R. Morton, *et al.*, "The first aspheric form and texture results from a production machine embodying the precession process," in *Proc. SPIE*, pp. 267-276, 2001.

[17] B. L. M. Li, J. Yuan, W. Yao, F. Zhou, M. Zhong, "Evolution and equivalent control law of surface roughness in shear-thickening polishing," *International Journal of Machine Tools and Manufacture*, vol. 108, pp. 113-126, 2016.

[18] L. B. L. Min, Y. Julong, D. Chenchen, D. Weitao, "Material removal mathematics model of shear thickening polishing (in Chinese)," *JOURNAL OF MECHANICAL ENGINEERING*, vol. 52, pp. 143-151, 2016.

[19] a. A. B. H. E. J. Cohen, "The 1.8m Technology Demonstration Mirror for Terrestrial Planet Finder," in *SPIE*, Glasgow, 2004.

[20] A. K. T. J. E. Harvey, "Scattering effects from residual optical fabrication errors," presented at the International Conference on Optical Fabrication and Testing, Tokyo, Japan, 1995.

[21] J. FILHABER, "LARGE OPTICS: Mid-spatial-frequency errors: the hidden culprit of poor optical performance," 2013.

[22] M. J. R. T. Hull, J. M. Barentine, A. Magruder, "Mid-spatial frequency matters: examples of the control of the power spectral density and what that means to the performance of imaging systems," in *SPIE*, Baltimore, 2012.

[23] R. N. H. John E. Krista, Felix Stoehrb, "20 years of Hubble Space Telescope optical modeling using Tiny Tim," *Optical Modeling and Performance Predictions V*, vol. 8127, pp. 13, 2011.

[24] Q. W. Jin Luo, Feng Pan, Yaowei Wei, "Study on the influence factors of the mid-spatial-frequency wavefront PSD1 error for large-aperture mirrors," presented at the SPIE, Chengdu, 2016.

[25] J. L. T. Bai, W. Zhang, Z. Zou, "Effect of surface roughness on the aerodynamic performance of turbine blade cascade," *Propulsion and Power Research*, vol. 3, pp. 82-89, 2014.

[26] F. S. a. A. Barrientos, "Surface Roughness Measurement on a Wing Aircraft by Speckle Correlation," *Sensors*, vol. 13, pp. 9, 2013.

[27] R.Hauert, "A review of modified DLC coatings for biological applications," *Diamond and Related Materials*, vol. 12, pp. 583-589, 2003.

[28] A. S. L. Mertus, "Implications of Diamond-Turned vs. Diamond Ground Mold Fabrication Techniques on Precision-Molded Optics," in *Polymer Optics and Molded Glass Optics: Design, Fabrication, and Materials II*, 2012.

[29] H. F. Rase, *Handbook of commercial catalysts: heterogeneous catalysts*: CRC press, 2000.

[30] D. A. a. J. Burge, *The Handbook of Optical Engineering* vol. Chaper 28, 2001.

[31] M. A. Piscotty, J. S. Taylor, and K. L. Blaedel, "Performance evaluation of bound diamond ring tools," *Optical Manufacturing and Testing*, vol. 2536, pp. 231-246, 1995.

[32] Y. Namba, H. Kobayashi, H. Suzuki, K. Yamashita, and N. Taniguchi, "Ultraprecision surface grinding of chemical vapor deposited silicon carbide for X-ray mirrors using resinoid-bonded diamond wheels," *CIRP Annals-Manufacturing Technology*, vol. 48, pp. 277-280, 1999.

[33] X. Tonnellier, P. Morantz, P. Shore, and P. Comley, "Precision grinding for rapid fabrication of segments for extremely large telescopes using the Cranfield BoX," 2012.

[34] X. Tonnellier, "Precision grinding for rapid manufacturing of large optics," 2009.

[35] P. Comley, P. Morantz, P. Shore, and X. Tonnellier, "Grinding metre scale mirror segments for the E-ELT ground based telescope," *CIRP annals-manufacturing technology*, vol. 60, pp. 379-382, 2011.

[36] T. C. G. Lo-A-Foe, "Single-point diamond turning," *Doctor Thesis of TUE*, 1989.

[37] A. Mir, X. Luo, and J. Sun, "The investigation of influence of tool wear on ductile to brittle transition in single point diamond turning of silicon," *Wear*, vol. 364, pp. 233-243, 2016.

[38] J. T. Carroll and J. S. Strenkowski, "Finite element models of orthogonal cutting with application to single point diamond turning," *International Journal of Mechanical Sciences*, vol. 30, pp. 899-920, 1988.

[39] C. Cheung and W. Lee, "Modelling and simulation of surface topography in ultra-precision diamond turning," *Proceedings of the Institution of Mechanical Engineers, Part B: Journal of Engineering Manufacture*, vol. 214, pp. 463-480, 2000.

[40] A. W. Stahli, *The Technique of Lapping*: A. W. Stahli Ltd.

[41] R. E. English, "Optical Flats". In Ingalls, Albert G. Amateur Telescope Making, Book Three. Scientific American. pp. 156–162, 1953.

[42] A. A. Mills, P. J. Turvey, "Newton's telescope, an examination of the reflecting telescope attributed to Sir Isaac Newton in the possession of the Royal Society," *Notes and Records of the Royal Society of London*, vol. 33, pp. 133-155, 1979.

[43] J. Gleick and G. L. Alexanderson, "Isaac Newton," *The Mathematical Intelligencer*, vol. 27, pp. 74-76, 2005.

[44] R. N. Wilson, *Reflecting telescope optics II: manufacture, testing, alignment, Modern Techniques*: Springer Science & Business Media, 2013.

[45] L. Holland, *The properties of glass surfaces*: Chapman & Hall London, 1964.

[46] V. B. Kaufman and R. C. Kistler, "Chemical mechanical polishing slurry useful for copper substrates," USA Patents, 1999.

[47] V. B. Kaufman and S. Wang, "Multi-oxidizer slurry for chemical mechanical polishing," USA Patents, 1998.
[48] J. M. Bennett, *Characterization of Surface Roughness*. Boston: Springer, 2007.
[49] D. Walker, R. Freeman, G. Hobbs, A. King, G. McCavana, R. Morton, *et al.*, "Zeeko 1 metre polishing system," in *Proc. 7th Int. Conf Lamda-map, Cranfield, UK June*, pp. 240, 2005.
[50] R. FREEMAN, A. Beaucamp, and G. MCCAVANA, "Manufacturing processes for free-form optics," in *Proc. Conference Chubu, Japan*, 2007.
[51] D. D. Walker, D. Brooks, A. King, R. Freeman, R. Morton, G. McCavana, *et al.*, "The 'Precessions' tooling for polishing and figuring flat, spherical and aspheric surfaces," *Optics Express*, vol. 11, pp. 958-964, 2003.
[52] D. D. Walker, R. Freeman, R. Morton, G. McCavana, and A. Beaucamp, "Use of the 'Precessions'™ process for prepolishing and correcting 2D & 2½D form," *Optics Express*, vol. 14, pp. 11787-11795, 2006.
[53] W. DD and P. Shore, "Manufacture of segments for extremely large telescopes: a new perspective," in *Proc of SPIE*, 2003.
[54] D. Walker, A. Beaucamp, C. Dunn, R. Freeman, A. Marek, G. McCavana, *et al.*, "First results on free-form polishing using the Precessions process," in *Proc. ASPE Winter Conference: Freeform Optics, Design, Fabrication, Metrology, Assembly*, 2004.
[55] D. D. Walker, A. Beaucamp, R. G. Bingham, D. Brooks, R. Freeman, S. Kim, *et al.*, "The precessions process for efficient production of aspheric optics for large telescopes and their instrumentation," in *Proceedings of SPIE*, pp. 73-84, 2002.
[56] D. Walker, A. Beaucamp, V. Doubrovski, C. Dunn, R. Evans, R. Freeman, *et al.*, "Automated optical fabrications: first results from the new Precessions 1.2 m CNC polishing machine," in *Proc. SPIE*, pp. 627309, 2006.
[57] D. Walker, A. Beaucamp, V. Doubrovski, C. Dunn, R. Evans, R. Freeman, *et al.*, "Commissioning of the first Precessions 1.2 m CNC polishing machines for large optics," in *Proc. SPIE*, pp. 62880, 2006.
[58] D. Walker, A. Beaucamp, V. Doubrovski, C. Dunn, R. Freeman, G. Hobbs, *et al.*, "New developments in the Precessions process for manufacturing free-form, large-optical, and precision-mechanical surfaces," in *Proc SPIE*, pp. 614805-1, 2006.
[59] D. Walker, A. Beaucamp, R. Freeman, R. Morton, G. McCavana, and J. Kelchner, "Precessions 2½D Correction of an Aspheric Mirror," 2006.
[60] D. D. Walker, A. T. Beaucamp, D. Brooks, V. Doubrovski, M. D. Cassie, C. Dunn, *et al.*, "New results from the Precessions polishing process scaled to larger sizes," in *Proceedings of SPIE*, pp. 71-80, 2004.

[61] D. D. Walker, A. Beaucamp, D. Brooks, R. Freeman, A. King, G. McCavana, *et al.*, "Novel CNC polishing process for control of form and texture on aspheric surfaces," in *Proc. SPIE*, pp. 99-105, 2002.

[62] D. D. Walker, A. T. Beaucamp, D. Brooks, V. Doubrovski, M. D. Cassie, C. Dunn, *et al.*, "Recent developments of Precessions polishing for larger components and free-form surfaces," in *Proceedings of SPIE*, pp. 281-289, 2004.

[63] G. Yu, D. D. Walker, and H. Li, "Research on fabrication of mirror segments for E-ELT," in *Proceedings of SPIE*, 2012.

[64] D. Walker, A. Beaucamp, C. Dunn, R. Evans, R. Freeman, R. Morton, *et al.*, "Active control of edges and global microstructure on segmented mirrors," in *SPIE Astronomical Telescopes+ Instrumentation*, pp. 701812-701812-9, 2008.

[65] A. Beaucamp and Y. Namba, "Super-smooth finishing of diamond turned hard X-ray molding dies by combined fluid jet and bonnet polishing," *CIRP Annals-Manufacturing Technology*, vol. 62, pp. 315-318, 2013.

[66] H. Martin, D. Anderson, J. Angel, R. Nagel, S. West, and R. Young, "Progress in the stressed-lap polishing of a 1.8-rn f/i mirror," in *Proc. SPIE*, 1990, pp. 682.

[67] S. West, H. Martin, R. Nagel, R. Young, W. Davison, T. Trebisky, *et al.*, "Practical design and performance of the stressed-lap polishing tool," *Applied Optics*, vol. 33, pp. 8094-8100, 1994.

[68] M. W. Johns, "Giant Magellan Telescope(GMT)," in *Proceedings of SPIE*, pp. 85-94, 2003.

[69] M. Johns, P. McCarthy, K. Raybould, A. Bouchez, A. Farahani, J. Filgueira, *et al.*, "Giant Magellan Telescope: overview," in *Proc. SPIE*, p. 84441H, 2012.

[70] R. A. Bernstein, P. J. McCarthy, K. Raybould, B. C. Bigelow, A. H. Bouchez, J. M. Filgueira, *et al.*, "Overview and status of the Giant Magellan Telescope project," in *SPIE Astronomical Telescopes+ Instrumentation*, pp. 91451C-91451C-16, 2014.

[71] H. Martin, J. Burge, B. Cuerden, S. Miller, B. Smith, and C. Zhao, "Manufacture of 8.4 m off-axis segments: a 1/5 scale demonstration," in *Proc. of SPIE Vol*, pp. 63, 2004.

[72] J. Lubliner and J. E. Nelson, "Stressed mirror polishing. 1: A technique for producing nonaxisymmetric mirrors," *Applied Optics*, vol. 19, pp. 2332-2340, 1980.

[73] J. E. Nelson, G. Gabor, L. K. Hunt, J. Lubliner, and T. S. Mast, "Stressed mirror polishing. 2: Fabrication of an off-axis section of a paraboloid," *Applied Optics*, vol. 19, pp. 2341-2352, 1980.

[74] T. S. Mast and J. E. Nelson, "The fabrication of large optical surfaces using a combination of polishing and mirror bending," *Advanced Technology Optical Telescopes IV*, vol. 1236, pp. 670-681, 1990.

[75] J. Nelson, "The Keck Telescope: A new technology substitutes electronics for steel," *American Scientist*, vol. 77, pp. 170-176, 1989.

[76] L. N. Allen, R. E. Keim, T. S. Lewis, and J. Ullom, "Surface error correction of a Keck lOm telescope primary mirror segment by ion figuring," *Advanced Optical Manufacturing and Testing II, SPIE,* vol. 1531, 1991.

[77] W. Kordonski and D. Golini, "Progress update in magnetorheological finishing," *International Journal of Modern Physics B,* vol. 13, pp. 2205-2212, 1999.

[78] W. I. Kordonsky, I. V. Prokhorov, S. R. Gorodkin, G. R. Gorodkin, L. K. Gleb, and B. E. Kashevsky, "Magnetorheological polishing devices and methods," USA Patents, 1995.

[79] W. I. Kordonski and S. Jacobs, "Magnetorheological finishing," *International Journal of modern physics B,* vol. 10, pp. 2837-2848, 1996.

[80] H. Pollicove and D. Golini, "Deterministic manufacturing processes for precision optical surfaces," in *Key Engineering Materials*, pp. 53-58, 2003.

[81] S. D. Jacobs, W. Kordonski, I. V. Prokhorov, D. Golini, G. R. Gorodkin, and T. D. Strafford, "Magnetorheological fluid composition," USA Patents, 1998.

[82] D. C. Harris, "History of Magnetorheological Finishing," *in Proc. of SPIE,* 2011.

[83] J. A. Menapace, "Developing magnetorheological finishing (MRF) technology for the manufacture of large-aperture optics in megajoule class laser systems," Lawrence Livermore National Laboratory (LLNL), Livermore, CA, 2010.

[84] J. A. Menapace, P. J. Davis, W. A. Steele, L. L. Wong, T. I. Suratwala, and P. E. Miller, "MRF applications: measurement of process-dependent subsurface damage in optical materials using the MRF wedge technique," Lawrence Livermore National Laboratory (LLNL), Livermore, CA, 2005.

[85] J. A. Menapace, P. J. Davis, W. A. Steele, M. R. Hachkowski, A. Nelson, and K. Xin, "MRF applications: on the road to making large-aperture ultraviolet laser resistant continuous phase plates for high-power lasers," Lawrence Livermore National Laboratory (LLNL), Livermore, CA, 2006.

[86] W. Kordonski, A. B. Shorey, and A. Sekeres, "New magnetically assisted finishing method: material removal with magnetorheological fluid jet," in *Proceedings of SPIE*, pp. 107-114, 2003.

[87] M. DeMarco, "Optical manufacturing with magneto-rheological finishing (MRF); Techical Digest," in *Optifab 2005: Technical Digest*, pp. 28-30, 2005.

[88] J. E. DeGroote, A. E. Marino, K. E. Spencer, and S. D. Jacobs, "Power spectral density plots inside MRF spots made with a polishing abrasive-free MR fluid; Technical Digest," in *Optifab 2005: Technical Digest*, pp. 134-138, 2005.

[89] T. Wang, H. Cheng, H. Yang, W. Wu, and H. Tam, "Controlling mid-spatial frequency errors in magnetorheological jet polishing with a simple vertical model," *Applied optics,* vol. 54, pp. 6433-6440, 2015.

[90] H. Hu, Y. Dai, and X. Peng, "Restraint of tool path ripple based on surface error distribution and process parameters in deterministic finishing," *Optics express*, vol. 18, pp. 22973-22981, 2010.
[91] O. W. Fähnle, H. Van Brug, and H. J. Frankena, "Fluid jet polishing of optical surfaces," *Applied optics*, vol. 37, pp. 6771-6773, 1998.
[92] S. M. Booij, "Fluid Jet Polishing," PhD, Applied Sciences, Delft University of Technology 2003.
[93] A. K. Gharai. "Abrasive Jet Machining," 12, 2012.
[94] O. W. Fähnle and H. van Brug, "Fluid jet polishing: removal process analysis," *Optical Fabrication and Testing*, vol. 3739, pp. 68-77, 1999.
[95] S. M. Booij, H. Van Brug, J. J. Braat, and O. W. Fa, "Nanometer deep shaping with fluid jet polishing," *Optical engineering*, vol. 41, pp. 1926-1931, 2002.
[96] W. I. Kordonski, A. B. Shorey, and M. Tricard, "Magnetorheological (MR) jet finishing technology," in *ASME 2004 International Mechanical Engineering Congress and Exposition*, pp. 77-84, 2004.
[97] A. Beaucamp, R. Freeman, R. Morton, K. Ponudurai, and D. Walker, "Removal of diamond-turning signatures on x-ray mandrels and metal optics by fluid-jet polishing," in *Proc. SPIE*, pp. 701835, 2008.
[98] M. Weiser, "Ion beam figuring for lithography optics," *Nuclear Instruments and Methods in Physics Research Section B: Beam Interactions with Materials and Atoms*, vol. 267, pp. 1390-1393, 2009.
[99] S. C. F. T. W. Drueding, S. R. Wilson, T. G. Bifano, "Ion beam figuring of small optical components," *Optical Engineering*, vol. 34, 1995.
[100] S. Wilson and J. McNeil, "Neutral ion beam figuring of large optical surfaces," in *31st Annual Technical Symposium*, pp. 320-324, 1987.
[101] L. Anderson, "Optically pumped electron spin polarized targets for use in the production of polarized ion beams," *Nuclear Instruments and Methods*, vol. 167, pp. 363-370, 1979.
[102] A. Meinel, S. Bashkin, and D. Loomis, "Controlled figuring of optical surfaces by energetic ionic beams," *Applied optics*, vol. 4, pp. 1674-1674, 1965.
[103] L. N. Allen, "Progress in ion figuring large optics," in *Laser-Induced Damage in Optical Materials: 1994*, pp. 237-247, 1995.
[104] W. Liao, X. Xie, and Y. Dai, "Ion beam processing for ultra-smooth glass-ceramic optics," *SPIE Newsroom*, 2014.
[105] C. Fanara, P. Shore, J. R. Nicholls, N. Lyford, J. Kelley, J. Carr, *et al.*, "A new reactive atom plasma technology (RAPT) for precision machining: the etching of ULE® surfaces," *Advanced Engineering Materials*, vol. 8, pp. 933-939, 2006.
[106] T. Arnold, G. Böhm, R. Fechner, J. Meister, A. Nickel, F. Frost, *et al.*, "Ultra-precision surface finishing by ion beam and plasma jet techniques—status and outlook," *Nuclear Instruments and Methods in Physics Research Section A:*

Accelerators, Spectrometers, Detectors and Associated Equipment, vol. 616, pp. 147-156, 2010.

[107] C. Cardinaud, M.-C. Peignon, and P.-Y. Tessier, "Plasma etching: principles, mechanisms, application to micro- and nano-technologies," *Applied Surface Science,* vol. 164, pp. 72-83, 2000.

[108] J. Muñoz-García, L. Vázquez, R. Cuerno, J. A. Sánchez-García, M. Castro, and R. Gago, "Self-organized surface nanopatterning by ion beam sputtering," in *Toward Functional Nanomaterials*, ed: Springer, pp. 323-398, 2009.

[109] T. Hobson, Ed., *Form Talysurf PGI 400/800/1200 Ultra Precision Surface Form and Finish Measurement System*. 2012.

[110] T. Hobson, *FORM TALYSURF INTRA Operator's Handbok*, 2002.

[111] A. H. B. H. Bunch, *The History of Science and Technology*: Houghton Mifflin Harcourt, 2004.

[112] J. H. Neal Brock, Brad Kimbrough, James Millerd, Michael North-Morris, Matt Novak and James C. Wyant, "Dynamic Interferometry," *Novel Optical Systems Design and Optimization VIII,* vol. 5875, 2005.

[113] J. H. a. J. Millerd, *Dynamic Interferometry Handbook: Getting Rid of the Jitters*, 2008.

[114] S. T. a. W. X. Peter Lehmann, "Fundamental aspects of resolution and precision in vertical scanning white-light interferometry," *Surface Topography: Metrology and Properties,* p. 3, 2016.

[115] R. F. M. Carfagni, L. Governi, M. Servi, F. Uccheddu, Y. Volpe, K. McGreevy, "Fast and Low Cost Acquisition and Reconstruction System for Human Hand-wrist-arm Anatomy," *Procedia Manufacturing,* vol. 11, pp. 1600-1608, 2017.

[116] H. L. Eaton, "Articulation measuring arm having rotatable part-carrying platen," ed. US, 2003.

[117] G. K. U. Mutilba, A. Olarra, A. Gutiérrez, E. Gomez-Acedo, M. Zubieta, "Performance Calibration of Articulated Arm Coordinate Measuring Machine," *Procedia Engineering,* vol. 63, pp. 720-727, 2013.

[118] D. Walker, R. Evans, R. Freeman, D. Riley, G. McCanvana, J. Simms, *et al.*, "The precessions polishing and hybrid grolishing process-implementation in a novel 1.2 m capacity machine tool," *Proceedings to the Laser Metrology and Machine Performance,* vol. 7, pp. 99-108, 2007.

[119] H. Y. W. G. Yu, D. D. Walker, X. Zheng, H. Li, C. Dunn, C. Gray, "Optimisation of grolishing freeform surfaces with rigid and semi-rigid tools," presented at the Advances in Optical and Mechanical Technologies for Telescopes and Instrumentation II, Edinburgh, UK, 2016.

[120] D. D. Walker, G. Yu, M. Bibby, C. Dunn, H. Li, H. Y. Wu, *et al.*, *Robotic automation in computer controlled polishing* vol. 11, 2016.

[121] D. Walker, C. Dunn, G. Yu, M. Bibby, X. Zheng, H. Y. Wu, *et al.*, "The role of robotics in computer controlled polishing of large and small optics," *Optical Manufacturing and Testing XI*, vol. 9575, 2015.

[122] C. J. Evans, E. Paul, D. Dornfeld, D. A. Lucca, G. Byrne, M. Tricard, *et al.*, "Material Removal Mechanisms in Lapping and Polishing," *CIRP Annals - Manufacturing Technology*, vol. 52, pp. 611-633, 2003.

[123] R. C. Johnson and H. Jasik, "Antenna engineering handbook," *New York, McGraw-Hill Book Company, 1984, 1356 p. No individual items are abstracted in this volume.*, 1984.

[124] A. T. Beaucamp, Y. Namba, P. Charlton, S. Jain, and A. A. Graziano, "Finishing of additively manufactured titanium alloy by shape adaptive grinding (SAG)," *Surface Topography: Metrology and Properties*, vol. 3, pp. 024001, 2015.

[125] A. Beaucamp, Y. Namba, H. Combrinck, P. Charlton, and R. Freeman, "Shape adaptive grinding of CVD silicon carbide," *CIRP Annals-Manufacturing Technology*, vol. 63, pp. 317-320, 2014.

[126] A. Beaucamp, Y. Namba, and P. Charlton, "Process mechanism in shape adaptive grinding (SAG)," *CIRP Annals-Manufacturing Technology*, vol. 64, pp. 305-308, 2015.

[127] H. Li, "Research on Manufactruing Mirror Segments for an Extremely Large Telescope " Ph.D., Department of Physics & Astronomy UCL, 2012.

[128] J. B. J. II, "Characterization of Opical Surface Grinding Using Bound and Loose Abrasives," Ph.D., College of Optical Science The University of Arizona 2011.

[129] R. Cross, "Elastic and viscous properties of Silly Putty," *American Journal of Physics*, vol. 80, 2012.

[130] D. Roylance, "Stress-strain curves," *Massachusetts Institute of Technology study, Cambridge*, 2001.

[131] P. B. M. D. W. Comstock, "Rolling diaphragm and rolling diaphragm devices," USA Patent, 1975.

[132] M. Yamamoto, "The visco-elastic properties of network structure III. Normal stress effect (Weissenberg effect)," *Journal of the physical society of Japan*, vol. 13, pp. 1200-1211, 1958.

[133] Psidot, "The Weissenberg Effect," ed, 2007.

[134] E. Soto, O. R. Enriquez, R. Zenit, and O. Manero, "Rodless Weissenberg Effect," 2008.

[135] D. W. Kim and J. H. Burge, "Rigid conformal polishing tool using non-linear visco-elastic effect," *Optics Express*, vol. 18, pp. 2242-2257, 2010.

[136] J. P. P. E. C. Teo, J. H. Evans, H. W. Ng, "Experimental investigation of failure load and fracture patterns of C2 (axis)," *Journal of Biomechanics*, vol. 34, pp. 1005-1010, 2001.

[137] K. S. T. Hamada, S. Tokushima, M. Watanabe, N. Akama, M. Takano, S. Sakuma, Y. Ezure "Dog clutch mechanism," USA Patent, 1987.

[138] E. P. S.Esposito, A. Tozzi, P. Stefanini, N. Devaney, "Cophasing of segmented mirrors using the pyramid sensor," presented at the *SPIE*, San Diego, California, United States, 2003.

Appendix A

The programme code for PSD analysis of 2D surface profiles is presented as below.

```
function result = PSD %calculate PSD
    [filename, pathname] = uigetfile('*.csv','Please select the file');
    name = strcat(pathname,filename);
    M = csvread(name,1,0);
    datax = M(:,1);
    datay = M(:,2);

%     datay = datay / 1e3;

    minx = min(datax);
    maxx = max(datax);

%   confirm N
    N = size(datax,1);

    deltax = (maxx - minx) / N;

    y = datay;
    y = y - min(y);

    m = 0 : floor(N/2);
    n = 0 : (N - 1);
    n = n';
    PNm = n * m;
    PNm = exp(-2 * pi * 1i * PNm / N);

    for f = 1 : N
        PNm(f,:) = PNm(f,:)*y(f);
    end

    PN = deltax / (N + 1) * abs(sum(PNm,1)).^2;
%     PN = 1 / (N + 1) * abs(sum(PNm,1)).^2;
    fm = m / (maxx - minx);

    semilogx(fm(1,2:end),PN(1,2:end))
```

```
%       semilogx(1./fm(1,2:end),PN(1,2:end))
        xlabel('spatial frequency (1/mm)')
%       xlabel('wave length(mm)')
        ylabel('PSD(¦Ìm^2 mm)')
%       ylabel('PSD(mm^2 )')
        grid on
        fm = fm';
        PN = PN';
        result.k = fm;
        result.PN = PN;
        dataSurfaceShape(:,1) = result.k;
        dataSurfaceShape(:,2) = result.PN;
        tabledata = table(dataSurfaceShape(:,1),dataSurfaceShape(:,2));
        [FileName, PathName] = uiputfile({'*.csv'});
        newname = strcat(PathName, FileName);
        writetable(tabledata,newname);

end
```

Appendix B

Remove System Errors for Metrology Using 4D Interferometers

System errors of the 4D interferometer is caused by the optical aberration induced by the lens in the beam expander. In order to eliminate the system errors, a flat reference surface, with surface average (Sa) less than 1 nm, was measured by the interferometer and the result is shown in **Figure B.1**.

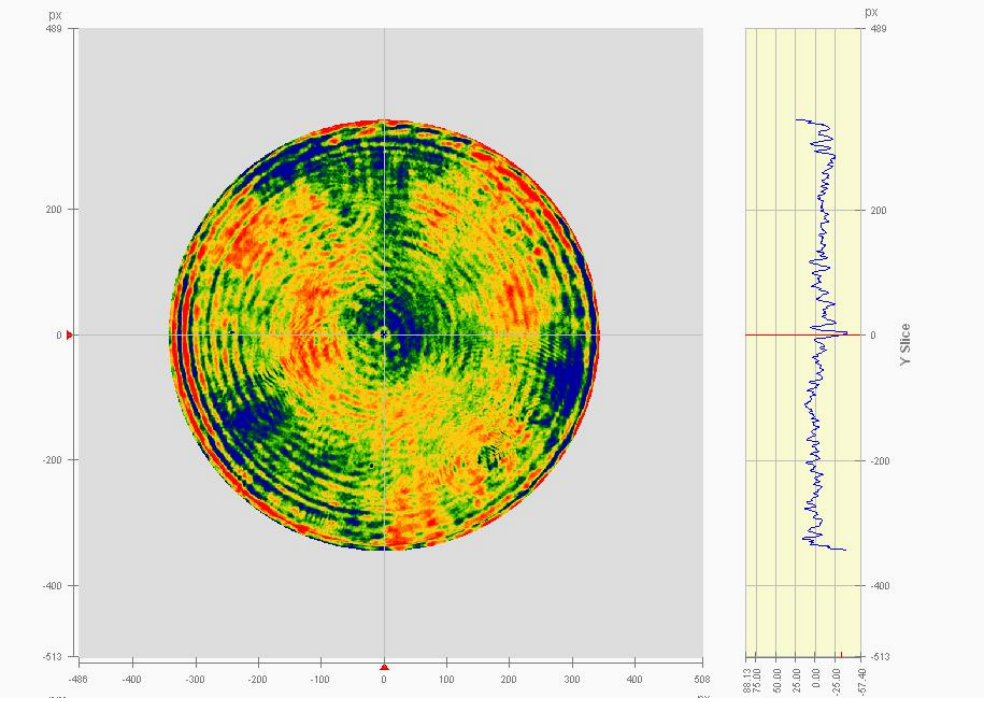

Figure B.1: The interferogram of the reference flat surface.

As the reference was nearly a perfect flat surface, the concentric rings and noises shown in **Figure B.1** were the reflection of the system error. This interferogram is called the error interferogram.

The errors can be considerably reduced by subtracting the measured interferogram by the error interferogram, which is shown in **Figure B.2**.

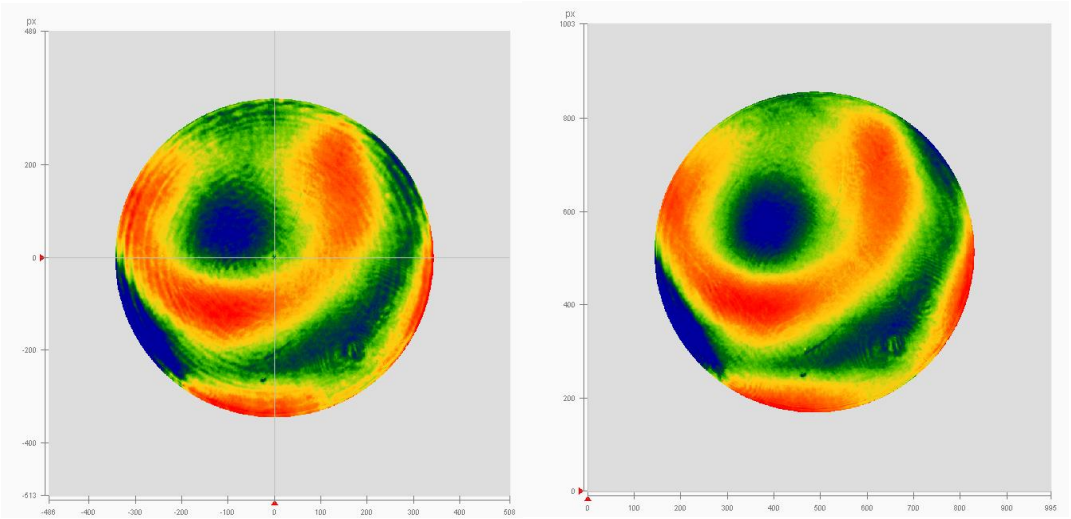

Figure B.2: The interferogram before and after the subtraction by the error interferogram.

Appendix C

The repeated experimental results before and after grolishing using a rigid KGS pad are shown in this section. **Figure C.1** shows the surfaces before and after grolishing by an un-conditioned KGS pad and **Figure C.2** shows the results after grolishing by a conditioned KGS pad.

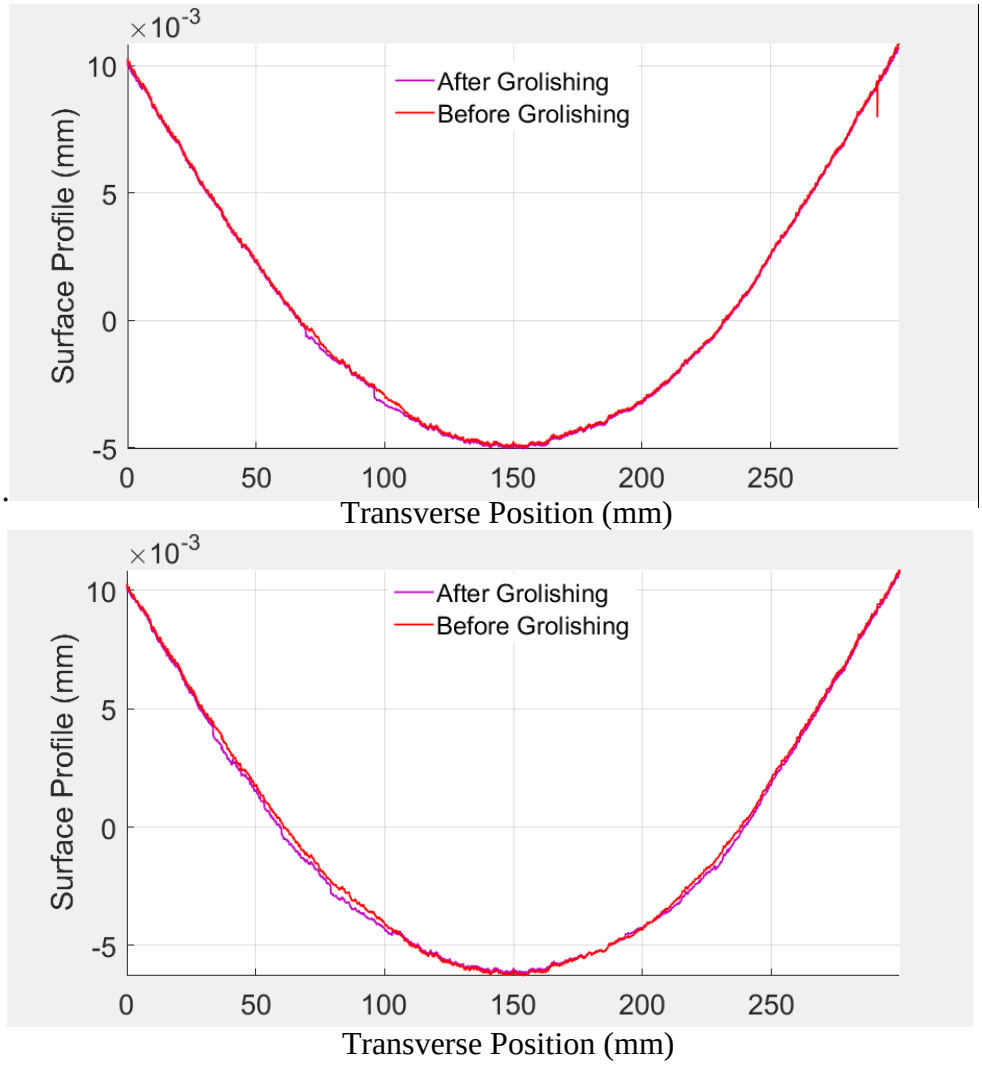

Figure C.1: Repeated experimental results before and after grolishing using a KGS pad without conditioning.

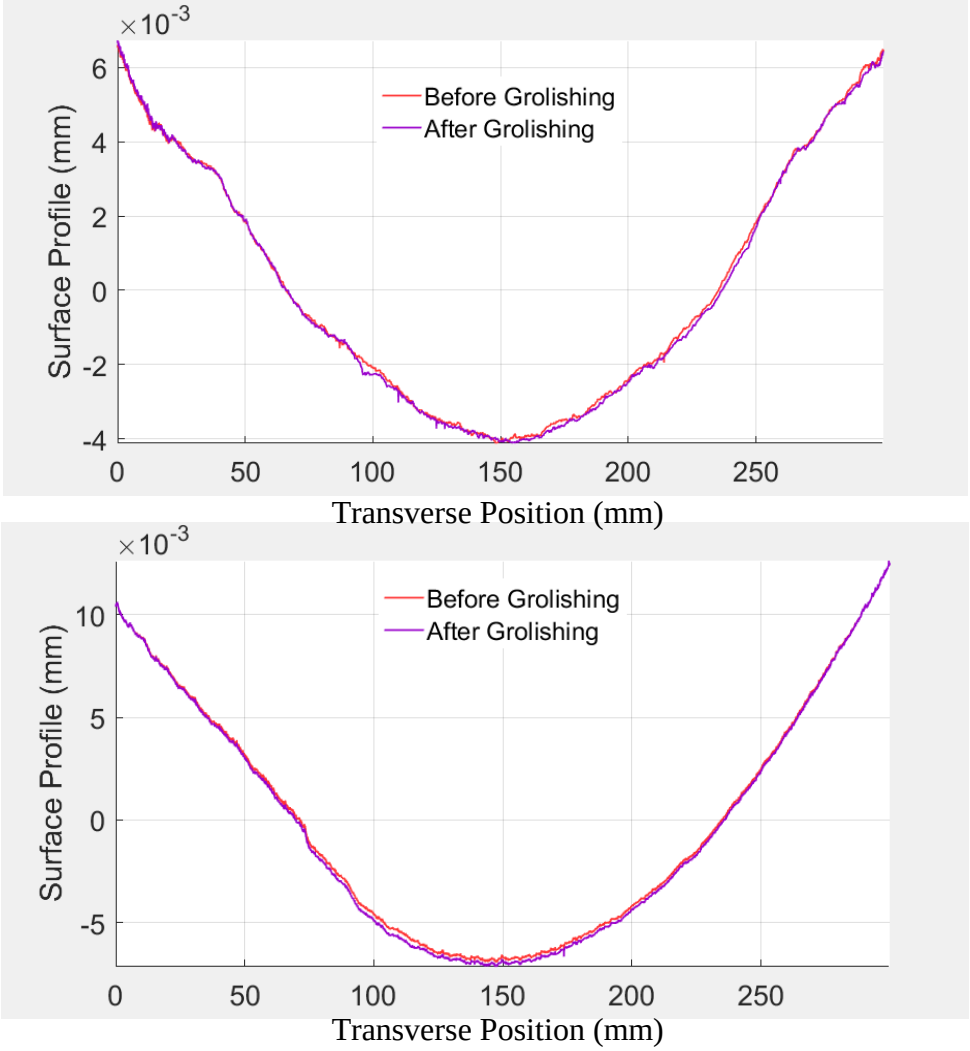

Figure C.2: Repeated experimental results before and after grolishing using a KGS pad after being conditioned.

Appendix D

Calculation for the Simulated Tool Influence Functions

The MatLab code for calculating the simulated tool influence functions are listed as below.

```
x=ww(;,1）;   % ww is the data exported from ANSYS
y=ww(;,2）;
z=ww(;,3）;

x=1000*x;     % change the unit from m to mm
y=1000*y;
z=z;

x=x-(max(x)+min(x))/2;
y=y-(max(y)+min(y))/2;
[X,Y,Z]=griddata(x,y,z,linspace(min(x),max(x),200)',linspace(min(y),max(y),200),
'v4');

[THETA,RHO] = cart2pol(X,Y);   % Convert to spherical coordinate system
Z=Z.*(3.14*33*180*RHO);
RHO(find(RHO>50))=NaN;
RHO(find(RHO<7.5))=NaN;

[XX,YY] = pol2cart(THETA,RHO);

Z=Z*0.25*10^(-12)
surf(XX,YY,-Z);

A=XX(100,:);
B=YY(100,:);
C=Z(100,:);

n=find(abs(A)>45);
C(n)=0;
plot(A,-C);
```